VILNIUS UNIVERSITY

AUDRIUS ZAUKEVIČIUS

THE USE OF ANGULAR DISPERSION FOR FORMATION OF HIGH PEAK POWER AND ULTRASHORT PULSED LIGHT BEAMS IN NONLINEAR INTERACTIONS

Doctoral dissertation
Physical sciences, physics (02P)

Vilnius, 2012

The researched was performed in 2008-2012 at Vilnius University

Scientific supervisor:

prof. dr. Gintaras Valiulis (*Vilnius University*, physical sciences, physics - 02P)

Consultant:

dr. Arūnas Varanavičius (*Vilnius University*, physical sciences, physics - 02P)

VILNIAUS UNIVERSITETAS

AUDRIUS ZAUKEVIČIUS

KAMPINĖS DISPERSIJOS PANAUDOJIMAS GALINGŲ IR ULTRATRUMPŲ IMPULSINIŲ ŠVIESOS PLUOŠTŲ FORMAVIMUI NETIESINIŲ SĄVEIKŲ METU

Daktaro disertacija
Fiziniai mokslai, fizika (02P)

Vilnius, 2012

Disertacija rengta 2008-2012 metais Vilniaus universitete

Mokslinis vadovas:

prof. dr. Gintaras Valiulis (*Vilniaus universitetas*, fiziniai mokslai, fizika - 02P)

Konsultantas:

dr. Arūnas Varanavičius (*Vilniaus universitetas*, fiziniai mokslai, fizika - 02P)

Contents

Acknowledgments

First of all I would like to thank my scientific supervisor *prof. Gintaras Valiulis* for giving me this opportunity to be his PhD student and providing me with the knowledge of mathematical description of nonlinear interactions. I am also thankful for the accurate dissertation title, originally written four years ago, which perfectly met my personal interests as well as scientific novelty, to which it was leading to.

Second I would like to thank my scientific consultant *dr. Arūnas Varanavičius* for generous help, support and patience while preparing my first manuscript. Without the manuscript-writing lessons I have learned from him, my thesis would be hardly readable. I am also grateful for the financial support, which has meant a lot for me, and had helped me to realize that not all bosses are greedy.

There are many more persons I would like to thank, including *prof. A. Piskarskas* for providing a great environment for the research, *prof. A. Stabinis* for the help in trying to crack the mind of god about parametric amplification, *prof. A. Dubietis* for granting the access to OSA papers, *prof. P. Di Trapani* for organizing the summer schools, *dr. A. Pugžlys* for the supervision during my internship, and my colleagues *dr. V. Jukna*, *dr. R. Antipenkov*, *dr. V. Pyragaitė*, *V. Martinėnaitė* and *J. Adamonis* for collaboration.

Most of all I would like to thank my parents and my wife for the support and believing in what I am doing.

Thank you,

Audrius Zaukevičius

To my mom and my wife, the two most fateful persons in my life.

List of abbreviations

GV group velocity

GVD group velocity dispersion

OPA optical parametric amplifier

NOPA noncollinear optical parametric amplifier

CPA chirped-pulse amplifier

OPCPA optical parametric chirped-pulse amplifier

OPXPA optical parametric X-pulse amplifier

PCWPA pulsed conical wave parametric amplifier

PCW pulsed conical wave

STC spatio-temporal coupling

BWE bi-direction wave equation

UPPE unidirectional pulse propagation equation

SEWA slowly evolving wave approximation

SVEA slowly varying envelope approximation

FWM four-wave-mixing

FS fused silica

Chapter 1

Introduction

Noncollinear optical parametric amplification is already proved to be the key element in the generation of ultrashort and powerful light pulses. Extremely broad gain bandwidth provided by noncollinear optical parametric amplifier (NOPA) [1] in the combination with chirped-pulse amplification (CPA) concept [2] has became a widely recognized amplification technique. Since the first demonstration of optical parametric chirped-pulse amplifier (OPCPA) [3] many systems based on this technique for generation of tunable femtosecond pulses with durations down to sub-5-fs have been reported [4, 5, 6]. With an increasing interest in this technique different setups have been developed for achieving TW-level signal pulse powers [7, 8, 9, 10] or high average powers as well [11, 12].

Typically, the broad amplification bandwidth is provided by NOPA operating at the so-called "magic" phase-matching angle [13, 14]. However, this noncollinear configuration has a drawback, arising as a consequence of pulse-front mismatch of signal and pump. It has been shown [15, 16, 17], that due to pulse-front mismatching, signal pulse experiences a reshaping, which leads to the reduced conversion efficiency and spatio-temporal distortions of the signal pulse, such as pulse-front tilt, angular dispersion and spatial chirp. The induced angular dispersion has been studied in several works [5, 18, 19]. However, the presence of the angular dispersion was considered as a consequence of the pulse-front tilting, but as it became apparent later, the pulse-front tilt can be also caused by the simultaneous

presence of the spatial and temporal chirps. Recently, an extensive 3D numerical study has revealed a new aspects of signal pulse reshaping during the amplification in noncollinear femtosecond OPCPA [20]. It has been shown, that when pump and signal fronts are not matched, the signal pulse becomes tilted and aside from angular dispersion has a spatial chirp. The main results of this study are presented in chapter 4.

In particular, the broad amplification bandwidth of the optical parametric amplifier (OPA) is provided by the noncollinear interaction geometry. When combined with an angularly dispersed signal beams, it could yield still broader parametric bandwidths [21, 22, 23]. Additionally, the use of angular dispersion could open the route for parametric amplification of chirped X-pulses, featuring temporal compression during propagation in free space [24, 25]. For amplification of high-peak-power pulses this feature would be of particular importance, since in contrast to ordinary OPCPA technique, the pulse compressor is no longer needed. Yet realization of such compressor-less idea has been left to be proven as obtaining a particular X-pulse for seeding is obscure.

It is well-known that in case of parametric amplification of tightly focused signal, the angular dispersion, corresponding to the phase matching curve, is imprinted in the signal pulse [26]. Usually, the imposed angular dispersion is considered as a drawback that must be corrected for, however, recently it was demonstrated, that it can be exploited in generation and amplification of pulsed Bessel beams [27] and pulsed conical waves (PCWs) in general [28]. Remarkably, due to tight focusing the initial Gaussian-shaped beam is self-adopted by the parametric amplifier and is transformed into conical one, defined by the phase-matching condition. In such a way Gaussian wave-packet can be reshaped into conical wave packet just by means of a lens and nonlinear crystal. However, in those works, parametric amplification was performed in the near field of the tightly focused signal, therefore it resulted in a sudden manifestation of the saturation regime without appreciable energy transfer from the pump.

In this contribution, we have proposed a method, which is aimed to deliver a new approach in generation and amplification of few-cycle high-peak-power light pulses by means of optical parametric amplification [29]. The presented method combines the major features of OPA and CPA, namely, the ultra-broad parametric bandwidth, which is achieved by achromatic phase matching, and amplification of stretched seed pulse, which is achieved by performing the far-field parametric amplification. Moreover, these features are brought in a simple setup, in which a pulse compressor is dismissed. The main results of this study are presented in chapter 5.

In addition to the generation of ultrashort light pulses, recently, a considerable attention has been drawn by spatio-temporal control of pulsed light beams in laser-matter interaction experiments [30, 31, 32, 33, 34, 35, 36, 37]. Pulsed light beams are said to exhibit spatio-temporal couplings (STCs) when their spatial properties depend on time, and vice versa, for example in case when the front of the pulse is tilted. The significance of these effects largely depends on the application as well as on parameters of the pulsed light beam, and while STCs may be negligible in some cases, they are detrimental in others. A great contribution in identifying and understanding the relations between the different STCs have been made by S. Akturk et. al. [38, 39, 40, 41]. It has been shown, that while there are eight such couplings in all, only two independent couplings exist. The presented theory also revealed, that in the general case, pulse-front tilt can be caused by simultaneous presence of spatial and temporal chirps, thus destroying the old, but wrong belief, that pulse-front tilt and angular dispersion are equivalent phenomena.

However, the spatio-temporal transformations, experienced while propagating through linear optical systems by the pulsed light beam containing STCs, has not been well explored yet. We have performed a theoretical study, which is intended to fill this gap and to provide an intuitive understanding of the behavior of pulsed light beams possessing STCs. The main results of this study are presented in chapter 3.

The main tasks of the thesis

1. To disclose the spatio-temporal dynamics of pulsed Gaussian beam, possessing first-order spatio-temporal couplings, during propagation in free space and after the reflection from a parabolic mirror.

2. To find optical scheme suitable for simultaneous space and time focusing of temporally chirped pulses by means of linear optics.

3. To study the spatio-temporal distortions of the signal pulse emerging in non-collinear optical parametric chirped-pulse amplifier and to obtain a quantitative description of this phenomenon.

4. To find a simple and practical optical scheme for broadband parametric chirped-pulse amplification with subsequent spatio-temporal compression of the signal pulse.

Scientific novelty

1. The essential role of the spatial chirp in linear propagation of pulsed Gaussian beams has been revealed.

2. The method for formation of pulses with a flat-top temporal profile by means of angularly dispersive element and a lens has been presented.

3. The conceptional scheme for the simultaneous space and time focusing of temporally chirped pulses by means of linear optics has been presented.

4. The diverse-domain analysis of the pulsed beams has been applied to study their spatio-temporal dynamics during the parametric amplification.

5. The obtained images of spatio-temporal, spatio-spectral and spatio-temporal spectrum distributions have manifested the actual spatio-temporal distortions of the signal pulse arising in NOPA. The obtained analytical expressions provide the quantitative description of this phenomenon.

6. The method for formation of pulsed conical waves by means of parametric amplification of the far field has been presented. In contrast to ordinary OPCPA technique, it does not require a pulse compressor, thus greatly facilitates the parametric amplification of few-cycle light pulses.

Statements to defend

1. The spatial chirp gives rise to the temporal chirp and pulse-front tilt, when the phase-front of the pulsed Gaussian beam is not flat. The angularly dispersed pulsed Gaussian beam may undergo temporal compression when propagating in free space even in the case when initial temporal chirp is negative. The pulse-front tilt of the angularly dispersed pulsed Gaussian beam may be counterweighted by the spatial chirp, acquired during propagation in free space.

2. In noncollinear optical parametric chirped-pulse amplifier, the magnitudes of the induced spatial and angular dispersions decrease at different rates with the increase of the signal pulse temporal chirp. The induced pulse-front tilt is nearly independent of the signal pulse temporal chirp, but is always smaller than the tilt of the pump pulse. In case of large temporal chirp, mainly the spatial chirp contributes to the pulse-front tilt of the signal.

3. Using nonlinear crystal as a spatial spectrum filter, the far field of the Gaussian wave-packet can be reshaped into the far field of the pulsed conical wave and simultaneously amplified with a large energy gain factor.

Practical value

The presented analytical expressions describing the spatio-temporal transformations of a pulsed Gaussian beam due to the presence of spatio-temporal couplings could provide an intuitive understanding of the behavior of ultrashort pulses and could be adopted in a broad range of practical applications. The presented method for formation of flat-top pulses could be applied in OPCPAs where flat-top pump pulses are preferred. The presented scheme for spatio-temporal compression of temporally chirped pulses could be employed in light-matter interaction experiments where enhanced localization of the pulse intensity is needed. A revealed role of initial pulse parameters in the spatio-temporal distortions, arising in NOPA,

could be used when designing a distortion-free NOPA or optical scheme for elimination of the induced distortions. The presented method for formation of pulsed conical waves could be used for formation of ultra-intense and propagation invariant wave-packets capable to propagate over many Rayleigh range in the desired material.

Approbation

Scientific papers related to the topic of this thesis

[**A1**] A. Zaukevičius, V. Jukna, R. Antipenkov, V. Martinėnaitė, A. Varanavičius, A. P. Piskarskas, G. Valiulis, Manifestation of spatial chirp in femtosecond noncollinear optical parametric chirped-pulse amplifier, J. Opt. Soc. Am. B **28**, 2902-2908 (2011).

[**A2**] R. Antipenkov, A. Varanavičius, A. Zaukevičius, A. P. Piskarskas, Femtosecond Yb:KGW MOPA driven broadband NOPA as a frontend for TW few-cycle pulse systems, Opt. Express **19**, 3519-3524 (2011).

[**A3**] A. Zaukevičius, G. Valiulis, Gaussian wave-packet reshaping into conical via parametric amplification of the far field, Opt. Commun. **288**, 101-106 (2013).

Conference presentations

Presented by Audrius Zaukevičius:

[**C1**] Open readings, Vilnius, Lithuania, A. Zaukevičius, V. Jukna, R. Antipenkov, V. Martinėnaitė, A. Varanavičius, A. P. Piskarskas, G. Valiulis, Spatial chirp and angular dispersion dynamics in femtosecond noncolinear OPCPA, 2009.

[**C2**] 39th LNFK, Vilnius, Lithuania, A. Zaukevičius, G. Valiulis, Space-time focusing of chirped pulses using axicons, 2011.

Co-author of the presentations:

[**C3**] 38th LNFK, Vilnius, Lithuania, R. Antipenkov, A. Varanavičius, A. Zaukevičius, G. Valiulis, A. P. Piskarskas, 512 nm pumped OPCPA setup for ultrabroadband femtosecond pulses amplification, 2009.

[**C4**] 39th LNFK, Vilnius, Lithuania, V. Jukna, A. Zaukevičius, R. Antipenkov, V. Martinėnaitė, A. Varanavičius, A. P. Piskarskas, G. Valiulis, Spatial chirp and angular dispersion dynamics in femtosecond noncollinear OPCPA, 2011.

[**C5**] ASSP 2012, San Diego, USA, V. Jukna, A. Zaukevičius, R. Antipenkov, V. Martinėnaitė, A. Varanavičius, A. P. Piskarskas, G. Valiulis, Spatial chirp and angular dispersion dynamics in femtosecond noncollinear OPCPA, 2012.

The contribution of co-authors

All the research was done at Vilnius University, Faculty of Physics, Department of Quantum Electronics under a supervision of prof. dr. G. Valiulis. The numerical and analytical part of the work was done by the author himself. However, it is important to note the significant contribution of these co-authors:

1. Prof. dr. G. Valiulis has suggested the main ideas for the research and has spurred the publishing of the obtained results.
2. Prof. habil. dr. A. P. Piskarskas took part in the interpretation of the obtained results [A1, A2].
3. Dr. A. Varanavičius was the key person in providing collaboration between the theorists and experimentalists. Additionally, he made a great contribution in preparing the manuscripts for [A1] and [A2].
4. Dr. V. Jukna contributed by deriving the analytical equations of section 4.2 and by presenting the results in [C4] and [C5].
5. Dr. R. Antipenkov has prepared the manuscript for [A2] and accompanied by V. Martinėnaitė have performed the experiment, presented in section 4.4.

In addition, it should be noted that author's knowledge in the field of optical parametric amplification has been greatly improved by discussions with prof. A. Stabinis here in Vilnius University, and also, by discussions with dr. G. Arisholm during the STELLA school held in Barcelona. Their contribution to this work is intangible, yet very significant.

The structure of the thesis

These thesis consists of six chapters. At the beginning of the first chapter, an introduction to the field of this work is given. In chapter 2, theoretical background is provided and equations used in numerical model are presented. These equations are referenced in the following chapters, depending on the physical situation

under consideration. Chapter 3 is aimed to give a comprehensive introduction to the spatio-temporal couplings of the pulsed Gaussian beams. Some general features of pulsed Gaussian beams possessing linear spatio-temporal couplings are disclosed. Chapter 4 is devoted to the investigation of signal pulse spatio-temporal distortions, occurring in noncollinear optical parametric amplifiers. The origin of these distortions is explained and dependencies on the initial pulse parameters are revealed. In chapter 5, a new concept of optical parametric chirped-pulse amplification technique is presented. The performance of this new technique is explored by numerical experiments. This chapter combines all the knowledge of the previous chapters. Finally, the major conclusions of this work are presented in the last chapter.

Chapter 2

A model of forward propagating plane waves

This chapter introduces the equations used throughout this work in the analytical studies as well as in the numerical experiments. One of the most important things in the theoretical work is knowing the scope of the validity of the equations that are employed. Therefore, in this chapter the particular attention is paid to the approximations made along the derivation of equations. In the following section, starting from the Maxwell's equations, the master wave equation of the thesis is derived, and the adopted assumptions are discussed. In the subsequent section, a well-known approximations for this master wave equation are considered in the way, that emphasizes and elucidates the lost accuracy in the proper description of the phenomenon. At the end of this chapter, focusing of the light beam by means of parabolic mirror is considered and the associated phase-factor is derived in the non-paraxial case.

2.1 Unidirectional wave equation with minimal approximations

A great contribution to the development of the optical pulse propagation models has been made by Kolesik et al. [42, 43, 44]. In those papers the derivation of the unidirectional pulse propagation equation (UPPE) from the Maxwell's equations is presented. In addition, it has been shown that various conventional carrier-

resolved [45, 46, 47, 48] as well as envelope propagation equations [49, 50, 51] can be derived, starting from the UPPE and employing the procedure that clearly elucidates the physical meaning of all the underlying approximations, and also reveals relations between different equations. At this point we should also mention that Kinsler [52, 53] has drawn some addition remarks in this field. This section is, most of the part, just a deliberated review of the previously referenced papers. Yet, since the results of these thesis are exceptionally theoretical, we have found it to be a good starting point to discuss what are the fundamental assumptions and approximations of the model used in this work.

At first, we postulate that Maxwell's equations provide a correct picture of the physical processes that are involved in following chapters of the thesis. Thus our starting point of derivations is the Maxwell's equations [54]

$$\nabla \times \mathbf{E}(\mathbf{r},t) = -\frac{\partial}{\partial t}\mathbf{B}(\mathbf{r},t), \tag{2.1.1}$$

$$\nabla \times \mathbf{H}(\mathbf{r},t) = \frac{\partial}{\partial t}\mathbf{D}(\mathbf{r},t) + \mathbf{J}(\mathbf{r},t), \tag{2.1.2}$$

$$\nabla \cdot \mathbf{D}(\mathbf{r},t) = \rho(\mathbf{r},t), \tag{2.1.3}$$

$$\nabla \cdot \mathbf{B}(\mathbf{r},t) = 0, \tag{2.1.4}$$

along with the continuity equation

$$\nabla \cdot \mathbf{J}(\mathbf{r},t) = -\frac{\partial}{\partial t}\rho(\mathbf{r},t), \tag{2.1.5}$$

where $\mathbf{E}$ and $\mathbf{H}$ are the electric and magnetic fields, respectively, $\mathbf{D}$ and $\mathbf{B}$ are the corresponding flux densities, $\mathbf{J}$ is the current density of free charges, $\rho(\mathbf{r},t)$ is the free charge density and $\mathbf{r}$ is the position vector. At this point let us introduce a general field vector $\mathbf{F}$, by which we will refer to each of the fields $\mathbf{E}$, $\mathbf{D}$, $\mathbf{H}$, $\mathbf{B}$, $\mathbf{J}$, and also $\mathbf{P}$ and $\mathbf{M}$, that will be introduced later. Each field can be represented in term of its projections

$$\mathbf{F} = F_x\mathbf{e}_x + F_y\mathbf{e}_y + F_z\mathbf{e}_z, \tag{2.1.6}$$

where $\mathbf{e}_x$, $\mathbf{e}_y$, $\mathbf{e}_z$ are the unit vectors in the Cartesian coordinate system, and F_x, F_y, F_z are the scalar components of the vector field. By substituting Eq. (2.1.6) into Maxwell equations, we would obtain the set of equations for each component of the vector field.

Before introducing the constitutive relations, we shall postulate, that scalar components F_x, F_y, F_z of each vector field can be viewed as an interference of a plane monochromatic waves

$$F_j(t,x,y,z) = \frac{1}{8\pi^3} \int_{-\infty}^{\infty}\int_{-\infty}^{\infty}\int_{-\infty}^{\infty} \hat{F}_j(\omega,k_x,k_y,z) e^{i(\omega t - k_x x - k_y y)} \mathrm{d}\omega \mathrm{d}k_x \mathrm{d}k_y, \qquad (2.1.7)$$

where ω is the temporal frequency and k_x, k_y are the spatial frequencies. Note that we have implicitly assumed the existence of a well defined propagation direction. In particular, we assume that each field $\mathbf{F}(t,x,y,z)$ evolves along the dominant propagation direction, and can be observed at arbitrary z as a function of time t and transverse coordinates x and y.

In this work it is assumed that the medium is anisotropic, yet homogeneous, meaning that neither electric nor magnetic susceptibility of the medium dependents on transverse (x,y) or longitudinal z coordinates, and neither does the electrical conductivity. In such case, the flux densities are related to the field vectors by the following constitutive relations [54]

$$\hat{\mathbf{D}} = \varepsilon_0 \hat{\mathbf{E}} + \varepsilon_0 \bar{\chi}_\mathrm{e}(\omega,k_x,k_y)\hat{\mathbf{E}}, \qquad (2.1.8)$$

$$\hat{\mathbf{B}} = \mu_0 \hat{\mathbf{H}} + \mu_0 \bar{\chi}_\mathrm{m}(\omega,k_x,k_y)\hat{\mathbf{H}}, \qquad (2.1.9)$$

$$\hat{\mathbf{J}} = \bar{\sigma}(\omega,k_x,k_y)\hat{\mathbf{E}}. \qquad (2.1.10)$$

where ε_0 is the permittivity and μ_0 is the permeability of free space, $\bar{\chi}_e$ and $\bar{\chi}_m$ are the tensors of electric and magnetic susceptibilities, respectively, and $\bar{\sigma}$ is the tensor of the electrical conductivity. Note that medium response to the applied fields depends on temporal as well as spatial frequencies, that is, on propagation

direction in the medium. The induced polarization and magnetization reads

$$\hat{\mathbf{P}} = \varepsilon_0 \bar{\chi}_{\mathrm{e}}(\omega, k_x, k_y)\hat{\mathbf{E}}, \tag{2.1.11}$$

$$\hat{\mathbf{M}} = \bar{\chi}_{\mathrm{m}}(\omega, k_x, k_y)\hat{\mathbf{H}}. \tag{2.1.12}$$

In this work we consider a medium, which is nonmagnetic, nonconducting and possess no free charges. Thus, for the rest of the derivation we assume that

$$\bar{\chi}_m = 0, \qquad \bar{\sigma} = 0, \qquad \rho = 0. \tag{2.1.13}$$

Actually, the electric susceptibility $\bar{\chi}_e$ depends on the strength of the applied electric field. This gives rise to the nonlinearity of the material. Provided that the external field applied to the material is small compared to the internal molecular fields, the relationship between $\hat{\mathbf{P}}$ and $\hat{\mathbf{E}}$ can be expanded in a Taylor series of the electric field

$$\hat{\mathbf{P}} = \varepsilon_0 \bar{\chi}^{(1)}(\omega, k_x, k_y)\hat{\mathbf{E}} + \varepsilon_0 \bar{\chi}^{(2)}(\omega, k_x, k_y)\hat{\mathbf{E}}^2 + \varepsilon_0 \bar{\chi}^{(3)}(\omega, k_x, k_y)\hat{\mathbf{E}}^3 + \dots \tag{2.1.14}$$

where $\bar{\chi}^{(1)}$, $\bar{\chi}^{(2)}$ and $\bar{\chi}^{(3)}$ are linear, second-order and third-order electric susceptibilities, respectively. In this work we will consider just a second and third-order nonlinearity of the medium, and for convenience we denote the nonlinear polarization as

$$\hat{\mathbf{P}}_{\mathrm{NL}} = \varepsilon_0 \bar{\chi}^{(2)}(\omega, k_x, k_y)\hat{\mathbf{E}}^2 + \varepsilon_0 \bar{\chi}^{(3)}(\omega, k_x, k_y)\hat{\mathbf{E}}^3. \tag{2.1.15}$$

Finally, by substituting Eq. (2.1.7) into Eq. (2.1.6), then Eq. (2.1.6) into Maxwell's equations, and then Eq. (2.1.8) into Eq. (2.1.2) and into Eq. (2.1.3), and Eq. (2.1.9) into Eq. (2.1.1), and taking a curl of Eq. (2.1.1) we obtain the following equation for the each plane wave of the electric field

$$\begin{aligned} \frac{\partial^2 \hat{\mathbf{E}}}{\partial z^2} + \left(\frac{\omega^2}{c^2} \bar{\varepsilon}(\omega, k_x, k_y) - k_x^2 - k_y^2 \right) \hat{\mathbf{E}} = \\ - \frac{\omega^2}{c^2} \frac{\hat{\mathbf{P}}_{\mathrm{NL}}}{\varepsilon_0} - \frac{\bar{\varepsilon}(\omega, k_x, k_y)^{-1}}{\varepsilon_0 e^{i(\omega t - k_x x - k_y y)}} \nabla \left(\nabla \cdot \hat{\mathbf{P}}_{\mathrm{NL}} e^{i(\omega t - k_x x - k_y y)} \right), \end{aligned} \tag{2.1.16}$$

where c is the speed of light in free space $c = (\varepsilon_0 \mu_0)^{-\frac{1}{2}}$. Note that we have

employed the vector Laplacian $\nabla^2\mathbf{F} = \nabla(\nabla\cdot\mathbf{F}) - \nabla\times\nabla\times\mathbf{F}$, and we have used the relationship between the linear susceptibility and relative permittivity of the medium $\bar{\varepsilon}(\omega, k_x, k_y) = 1 + \bar{\chi}^{(1)}(\omega, k_x, k_y)$.

In the following we neglect the second term on the right hand side of Eq. (2.1.16), which describes the spatial gradient of the nonlinear polarization. This is justified by its insignificance in comparison to other terms in the equation. Nevertheless, we should note that this term may give rise to phenomena such as nonlinear diffraction [55].

In this work we consider only a linearly polarized fields, including the fields, resulting from the response of the medium ($\mathbf{P}$, $\mathbf{M}$). Therefore, at this point we drop the vector notation of the field, since for plane polarized field, a scalar version allowing just for one of the linear polarization components is sufficient. However, for materials that couple the orthogonal polarizations together due to second-order nonlinearity, we could write one equation for each polarization and then find that they were coupled together by the nonlinearity.

Finally, from Eq. (2.1.16) we arrive to

$$\frac{\partial^2\hat{E}}{\partial z^2} + \left(\frac{\omega^2}{c^2}\varepsilon(\omega, k_x, k_y) - k_x^2 - k_y^2\right)\hat{E} = -\frac{\omega^2}{c^2}\frac{\hat{P}_{\mathrm{NL}}}{\varepsilon_0}. \tag{2.1.17}$$

Thus, we have obtained a so-called bi-direction wave equation (BWE) [52, 53], which accounts for forward and backward-propagating waves. Note that the backward-propagating wave originates *not due to* reflection from some boundary. The source of the backward-propagating wave is the nonlinear polarization $\hat{P}_{\mathrm{NL}}$. In this sense, the obtained equation is exact and all the prerequisites are readily fulfilled in the experimental situations that are in the scope of these thesis. However, handling of forward and backward-propagating waves in numerical simulations is cumbersome. Therefore, in the following we adopt a reasonable simplification for the bi-direction wave equation.

In order to obtain a unidirectional wave equation, we make a substitution

$$\hat{E}(\omega, k_x, k_y, z) = \hat{E}_1(\omega, k_x, k_y, z) \exp\left(-ik_z(\omega, k_x, k_y)z\right), \tag{2.1.18}$$

where k_z is the projection of the wave vector onto z axis, namely

$$k_z(\omega, k_x, k_y) = \sqrt{k(\omega, k_x, k_y)^2 - k_x^2 - k_y^2}. \tag{2.1.19}$$

In such case a fast variation of the spatial phase along the z axis is precisely removed from the $\hat{E}_1(\omega, k_x, k_y, z)$, since it is done individually for each components of the electric field.

Note that there is no assumptions associated with the substitution of Eq. (2.1.18) into Eq. (2.1.17) and it can be done without any loss of generality. The approximation is adopted afterwards, when we assume a so-called slowly evolving wave approximation (SEWA) [49, 45, 56]. In particular, by assuming that $\dfrac{\partial^2 \hat{E}_1}{\partial z^2} \ll 2k_z(\omega, k_x, k_y)\dfrac{\partial \hat{E}_1}{\partial z}$, we obtain

$$\frac{\partial \hat{E}_1}{\partial z} = -\frac{i}{2k_z(\omega, k_x, k_y)} \frac{\omega^2}{c^2} \frac{\hat{P}_{\mathrm{NL}}}{\varepsilon_0} e^{+ik_z(\omega, k_x, k_y)z}, \tag{2.1.20}$$

and, finally, from the definition of E_1, we obtain the following equation

$$\frac{\partial \hat{E}}{\partial z} + ik_z(\omega, k_x, k_y)\hat{E} = -\frac{i}{2k_z(\omega, k_x, k_y)} \frac{\omega^2}{c^2} \frac{\hat{P}_{\mathrm{NL}}}{\varepsilon_0}. \tag{2.1.21}$$

This equation is termed as non-paraxial forward Maxwell equation (non-paraxial FME) or unidirectional pulse propagation equation (UPPE) [42, 43, 44]. This is a master wave-equation used throughout the simulations of the thesis.

Note that SEWA is equivalent to elimination of the backward-propagating wave solutions from bi-direction wave equation [49, 45, 46, 56]. It is applicable as long as the optical field, generated in the backward direction, is so weak, that its contribution to the nonlinearity can be neglected. It is essential to realize that SEWA is inherent in any one-way propagating pulse evolution equation [44]. However, the obvious problem with SEWA is that it is not a priori clear whether

it holds or not in a particular situation. Only very recent investigation of mutual interaction between forward and backward-propagating waves has revealed, that backward-generated wave is most likely unimportant in case of typical single-filamentation scenarios [57]. Note that when the backward-propagating wave can be neglected, UPPE is equivalent to BWE, but the numerical solution is much more efficient.

Nonetheless, in the linear case, when $\hat{P}_{\mathrm{NL}} = 0$, there is no need for such approximation as SEWA, since there is no coupling between the forward and backward propagating waves, and furthermore the BWE has an exact solution in this case:

$$\hat{E}(\omega, k_x, k_y, z) = \hat{E}(\omega, k_x, k_y, z = 0) \exp\left(-i\sqrt{k(\omega, k_x, k_y)^2 - k_x^2 - k_y^2}z\right), \tag{2.1.22}$$

where $k(\omega, k_x, k_y)^2 = \dfrac{\omega^2}{c^2}\varepsilon(\omega, k_x, k_y)$ is the magnitude of the wave vector. Thus, the linear propagation of the pulsed light beams can be simulated with minimal approximations as discussed after Eq. (2.1.17).

Note that in the general case, the magnitude of the wave vector $k(\omega, k_x, k_y)$, in addition to the temporal frequency ω, also depends on the spatial frequencies k_x and k_y, that is, on propagation direction in the medium. In what follows, the explicit form of this dependence in case of uniaxial anisotropic media is provided.

Recall that spatial frequencies are related to the magnitude of the wave vector simply as

$$k_{x,y} = k(\omega, k_x, k_y) \sin \alpha_{x,y}, \tag{2.1.23}$$

where $\alpha_{x,y}$ is the angle between the wave vector projection in the xz or yz plane and the z axis. Assuming that the optic axis of the uniaxial crystal lies in the xz plane, the following relations for the extraordinary wave can be set

$$k(\omega, k_x)^2 = \frac{\omega^2}{c^2} n(\omega, k_x)^2 = \frac{\omega^2}{c^2} \frac{n_{\mathrm{o}}(\omega)^2 n_{\mathrm{e}}(\omega)^2}{n_{\mathrm{o}}(\omega)^2 \sin^2 \theta_{k_x} + n_{\mathrm{e}}(\omega)^2 \cos^2 \theta_{k_x}}, \tag{2.1.24}$$

$$\theta_{k_x} = \theta - \alpha_x = \theta - \arcsin\left(\frac{k_x}{k(\omega, k_x)}\right), \tag{2.1.25}$$

where θ is the angle between the optic axis and the z axis, and $n_{\mathrm{o}}(\omega)$, $n_{\mathrm{e}}(\omega)$ are the principal indices of the uniaxial crystal. Substituting Eq. (2.1.25) into Eq. (2.1.24) and then solving it for $k(\omega, k_x)$, we obtain

$$k(\omega,k_x)^2 = \frac{k_{\mathrm{o}}^2 k_{\mathrm{e}}^2}{k_{\mathrm{o}}^2\sin^2\theta + k_{\mathrm{e}}^2\cos^2\theta} + \frac{k_{\mathrm{o}}^4\sin^2\theta + k_{\mathrm{e}}^4\cos^2\theta - k_{\mathrm{o}}^2k_{\mathrm{e}}^2}{\left(k_{\mathrm{o}}^2\sin^2\theta + k_{\mathrm{e}}^2\cos^2\theta\right)^2}k_x^2 \\ - \frac{k_{\mathrm{o}}k_{\mathrm{e}}\sin(2\theta)\left(k_{\mathrm{e}}^2 - k_{\mathrm{o}}^2\right)\sqrt{k_{\mathrm{o}}^2\sin^2\theta + k_{\mathrm{e}}^2\cos^2\theta - k_x^2}}{\left(k_{\mathrm{o}}^2\sin^2\theta + k_{\mathrm{e}}^2\cos^2\theta\right)^2}k_x, \tag{2.1.26}$$

where $k_{\mathrm{o}} = \dfrac{\omega}{c}n_{\mathrm{o}}(\omega)$, $k_{\mathrm{e}} = \dfrac{\omega}{c}n_{\mathrm{e}}(\omega)$. As it can be seen, two propagation-direction dependent terms appear next to the usual term of this equation. The term next to k_x is responsible for the spatial walk-off of the extraordinary wave due to birefringence, and the term proportional to k_x^2 modifies the diffraction of the extraordinary beam [58, 59]. The actual direction along the x axis, in which the extraordinary wave gets shifted due to birefringence, will depend on the particular arrangement, that is, on the sign of θ and the type of uniaxial crystal. Recall that for the positive uniaxial crystal ($k_{\mathrm{e}} > k_{\mathrm{o}}$) the extraordinary wave is dragged towards the optic axis, and for the negative ($k_{\mathrm{e}} < k_{\mathrm{o}}$) - outwards. Thus, the extraordinary wave will be shifted in the positive x direction whenever the sign of the $\sin(2\theta)\left(k_{\mathrm{e}}^2 - k_{\mathrm{o}}^2\right)$ is positive, otherwise it will be shifted in the negative x direction.

In addition to the linear propagation of the waves, in this work we will consider a second and third order nonlinearity of the medium. However, nonlinear susceptibilities $\bar{\chi}^{(2)}$ and $\bar{\chi}^{(3)}$, that are present in the nonlinear polarization $\hat{P}_{\mathrm{NL}}$ (Eq. (2.1.15)), will be assumed to be a scalar quantities. Let us note that this scalar representation should be still understood as a description of two transverse single-polarization components of an optical field that are coupled by a system of equations [56, 60]. While each equation appears scalar, the two become coupled through the nonlinear polarization term $\hat{P}_{\mathrm{NL}}$. Additionally, the $\bar{\chi}^{(2)}$ and $\bar{\chi}^{(3)}$ susceptibilities will be assumed to be independent on temporal or spatial frequencies,

since there is no such data readily available. This approximation corresponding to the assumption that nonlinear response to the electric field is instantaneous and isotropic. In such case, the actual susceptibilities can be replaced by the corresponding effective quantities, designated for each nonlinear interaction individually, thus the nonlinear polarization is rewritten as

$$\hat{P}_{\mathrm{NL}} = \varepsilon_0 \chi^{(2)}_{\mathrm{eff}} \hat{E}^2 + \varepsilon_0 \chi^{(3)}_{\mathrm{eff}} \hat{E}^3. \tag{2.1.27}$$

It should be noted the actual objective in this work is not the electric field it self, but the complex amplitude, which represent the envelope of the electric field. Without any assumptions or loss of generality, the electric field can be written as

$$E(t,x,y,z) = \frac{1}{2} A(t,x,y,z) \mathrm{e}^{i\omega_{\mathrm{c}} t} + \frac{1}{2} A^*(t,x,y,z) \mathrm{e}^{-i\omega_{\mathrm{c}} t}, \tag{2.1.28}$$

where $A(t,x,y,z)$ is the complex amplitude and ω_{c} is the carrier frequency. Note that carrier frequency is just a coefficient, which sets the linear temporal phase relative to the complex amplitude, and so the temporal spectrum of the pulse is positioned along the ω axis. Therefore, it not necessarily corresponds to the central frequency ω_0 of the pulse, as it might be thought at first.

Typically, in the performed experiments the total electric field is composed of a distinct constituents. This could be illustrated as follows

$$\begin{aligned} E(t,x,y,z) &= E_1(t,x,y,z) + E_2(t,x,y,z) + E_3(t,x,y,z) + \ldots \\ &= \frac{1}{2} A_1(t,x,y,z) \mathrm{e}^{i\omega_1 t} + \frac{1}{2} A_2(t,x,y,z) \mathrm{e}^{i\omega_2 t} + \frac{1}{2} A_3(t,x,y,z) \mathrm{e}^{i\omega_3 t} + \ldots + \text{c.c.} \end{aligned} \tag{2.1.29}$$

where A_1, A_2, A_3 are the complex amplitudes of the constituents, and ω_1, ω_2, ω_3 are their carrier frequencies; "c.c." denotes the complex conjugate part. By transforming the Eq. (2.1.29) into Fourier domain and then substituting into Eq. (2.1.21), we could obtain a set of UPPEs, describing the evolution of the complex amplitude of each individual constituent in the spectral domain. Obviously, the obtained differential equations would be coupled via nonlinear term

presented in Eq. (2.1.21). The convenience brought by introducing the complex amplitude and separation of the total electric field into distinct constituents will become apparent in the next section. However, it should be noted a priori that the temporal or spatial spectra of the constituents must be well-separable or their states of polarization must be different. Otherwise, the distinction between the different constituents disappears, and such description becomes inaccurate. This requirement must be also considered in the situation when one of the constituents undergo the supercontinuum generation [61, 62], that is, in the situation when the temporal spectra of the initial pulses are narrow, but get broadened significantly during the nonlinear propagation.

2.2 Useful approximations for unidirectional wave equation

In order to gain more insight into Eq. (2.1.22) additional approximations have to be made. In particular, the magnitude of the propagation vector $k_z(\omega, k_x, k_y)$ is simplified by applying two approximations, which are very common in the literature on optics, namely, the paraxial approximation for the beams and the quasi-monochromatic approximation for the pulses. It is at this stage that artificial parameters are introduced into a propagation model.

In case of paraxial approximation it is assumed that the spatial spectrum of the beam is narrow enough, so that $k_x^2 + k_y^2 \ll k^2(\omega, k_x, k_y)$, and the propagation factor in the exponential of Eq. (2.1.22) is approximated to the first order in Taylor series as follows

$$k_z(\omega, k_x, k_y) = \sqrt{k(\omega, k_x, k_y)^2 - k_x^2 - k_y^2} \approx k(\omega, k_x, k_y) - \frac{k_x^2 + k_y^2}{2k(\omega, k_x, k_y)}. \quad (2.2.1)$$

As it can bee seen, the obtained equation has a suggestive appearance, as distinct phenomena are described by the different terms. In detail, the first term accounts for dispersive pulse propagation in the medium, whereas the second, for diffraction of the beam. If the second term was omitted, then we would have the plane wave

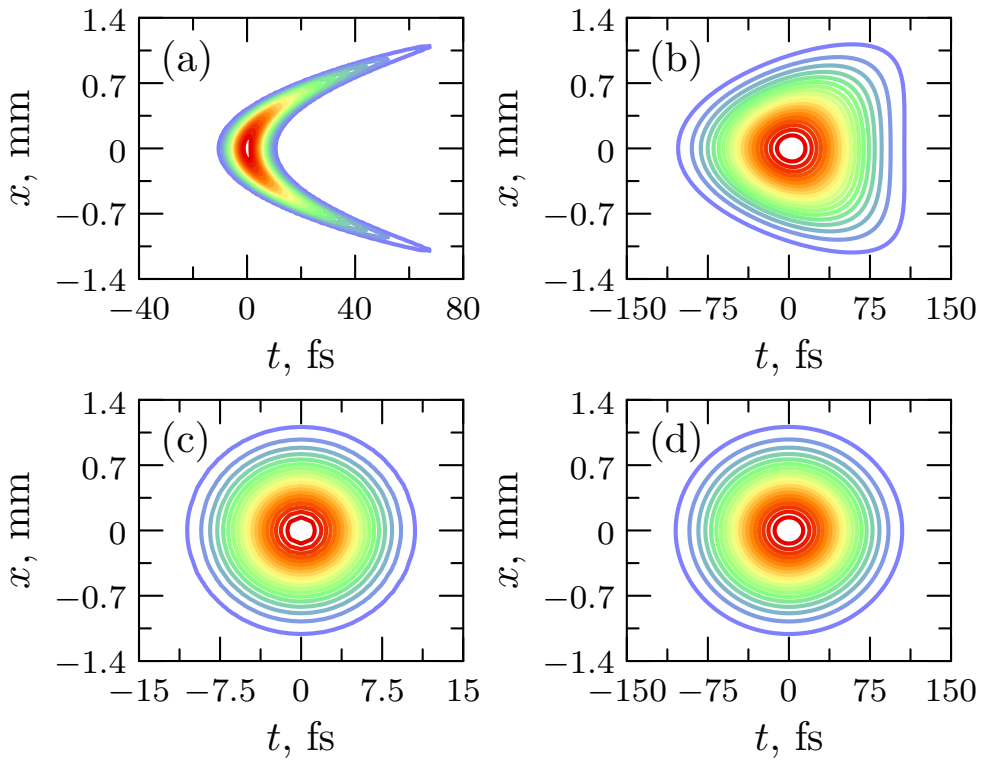

Figure 2.1: Spatio-temporal intensity profiles of pulsed Gaussian beam after the propagation in free space. In (a) and (b) graphs the magnitude of the wave vector was approximated as in Eq. (2.2.1), whereas in (c) and (d) graphs it was approximated as in Eq. (2.2.4). Initial parameters were as folllows: transform-limited duration $\tau_{\mathrm{TL}} = 10$ fs (FWHM), beam diameter $\rho = 10$ μm (FWHM), the central wavelength $\lambda_0 = 0.8$ μm, propagation distance $d = 30$ mm; in (b) and (d) graphs the pulse was linearly chirped and its initial duration was $\tau = 100$ fs (FWHM). All graphs are normalized.

model, yet accounting for a full material dispersion and imposing no restrictions to the bandwidth of the pulse.

It can be readily seen, that the term accounting for the diffraction of the beam is frequency dependent. It corresponds to the fact that the beam divergence is different for different frequencies. This dependence on frequency results in reshaping of the ultrashort pulsed Gaussian beam, even when it is propagating in free space: the transform-limited pulsed beam acquires the parabolic shape (Fig. 3.9a), whereas the temporally chirped pulsed beam acquires the triangular shape (Fig. 3.9b). In both cases the transform-limited duration is the same. Note that if the beam is diverging, the periphery of the beam lags behind the central part, as in Fig. 3.9a, but if the beam is converging the periphery advances.

Commonly, Eq. (2.2.1) is further simplified by adopting the quasi-monochromatic

approximation. In case of quasi-monochromatic approximation it is assumed that the bandwidth of the pulse is narrow enough, so that deviation from the reference frequency ω_{R} is not significant, that is, $|\Omega = \omega - \omega_{\mathrm{R}}| \ll \omega_{\mathrm{R}}$. In such case the magnitude of the wave vector $k(\omega, k_x, k_y)$ is expanded in Taylor series, and usually only the terms up to second order are taken into account

$$k(\omega, k_x, k_y) \approx k(\omega_{\mathrm{R}}, k_x, k_y) + k'\Omega + k''\Omega^2, \tag{2.2.2}$$

where $k(\omega_{\mathrm{R}}, k_x, k_y)$ is the magnitude of the wave vector corresponding to the reference frequency (in case of isotropic medium it could be simply denoted as k_{R}), $k' = \left.\dfrac{\mathrm{d}k}{\mathrm{d}\omega}\right|_{\omega_{\mathrm{R}}}$ is the inverse group velocity, namely, group velocity (GV) is equal to $u = \dfrac{1}{k'}$, and $k'' = \left.\dfrac{\mathrm{d}^2k}{\mathrm{d}\omega^2}\right|_{\omega_{\mathrm{R}}}$ describes the group velocity dispersion (GVD). Note that in Eq. (2.2.2) the dependence of dispersion orders on the spatial frequencies k_x and k_y is omitted. It is a reasonable assumption, since GV and GVD usually have a weak dependence on the propagation direction in the medium.

However, in case of quasi-monochromatic approximation, the $k(\omega, k_x, k_y)$ in the denominator of the diffraction term (Eq. (2.2.1)) is approximated to the zeroth order, namely

$$-\frac{k_x^2 + k_y^2}{2k(\omega, k_x, k_y)} \approx -\frac{k_x^2 + k_y^2}{2k(\omega_{\mathrm{R}}, k_x, k_y)}, \tag{2.2.3}$$

and thus, under the quasi-monochromatic approximation in addition to paraxial approximation, the magnitude of the propagation vector $k_z(\omega, k_x, k_y)$ is approximated as

$$k_z(\omega, k_x, k_y) \approx k(\omega_{\mathrm{R}}, k_x, k_y) + k'\Omega + k''\Omega^2 - \frac{k_x^2 + k_y^2}{2k(\omega_{\mathrm{R}}, k_x, k_y)}. \tag{2.2.4}$$

As we can see by comparison with Eq. (2.2.1), the term, accounting for the diffraction of the beam, now does not depend on the temporal frequency. Such approximation has a significant effect on the spatio-temporal profile of the ultrashort pulsed Gaussian beam considered previously. As it can be seen from Figs. 3.9c and 3.9d, in contrast to the previous case, the spatio-temporal shape of the pulsed

beam does not show any changes during the propagation in free space. This is due to the fact that the beam divergence was assumed to be the same for all the temporal frequencies.

However, it is important to note, that despite the drastic assumptions and lost accuracy in properly describing the diffraction of the ultrashort pulsed beam, the quasi-monochromatic approximation is of particular importance. It enables to obtain a relatively simple analytical expressions for the straightforward analysis of the pulsed Gaussian beam, propagating throughout the arbitrary optical scheme. Actually, the whole analytical study of chapter 3 is based on this approximation.

It is important to note, that the reference frequency ω_{R} is actually a free parameter. However, in most situations the frequency corresponding to the central component of the pulse spectrum is taken as a reference frequency. Such choice has an obvious reasons, since the central components contribute the most to the evolution of the temporal pulse profile, and the magnitude of the approximated wave vector has exact value just at the reference frequency (Eq. (2.2.2)). Consequently, the central frequency ω_0 is usually referred as a reference frequency ω_{R} without the explicit justification [63].

The nonlinear term in Eq. (2.1.21) can also be approximated accordingly. In particular, the most common approximation, yet the most crude, is a so-called slowly varying envelope approximation (SVEA) [44]. Under this approximation, the nonlinear term is approximated as

$$-\frac{i}{2k_z(\omega,k_x,k_y)}\frac{\omega^2}{c^2}\frac{\hat{P}_{\mathrm{NL}}}{\varepsilon_0}\approx-\frac{i}{2k_{\mathrm{R}}}\frac{\omega_{\mathrm{R}}^2}{c^2}\frac{\hat{P}_{\mathrm{NL}}}{\varepsilon_0}. \tag{2.2.5}$$

As it can be seen, it is assumed that $k_z(\omega,k_x,k_y)\approx k_{\mathrm{R}}$, and in addition, that the dependence on the temporal frequency is negligible $\omega\approx\omega_{\mathrm{R}}$. As a result, this approximation omits such phenomenon as a self-steepening of the pulse envelope, which in case of extremely short pulses may have a crucial consequences, such as optical shock and blow-up [63].

In order to see how this approximation is actually incorporated, let's consider

a particular case. In what follows, we consider the case when three waves, those temporal or spatial spectra are well-separated or their states of polarization are different, are propagating in the nonlinear media. Thus, by transforming the Eq. (2.1.29) into Fourier domain and then substituting together with Eq. (2.1.27) into Eq. (2.1.21), we obtain a sum of UPPEs, depicting the evolution of the complex amplitudes of each waves in the spectral domain

$$\frac{\partial}{\partial z}\left(\hat{A}_1+\hat{A}_2+\hat{A}_3+\text{c.c.}\right)+ik_z(\omega,k_x,k_y)\left(\hat{A}_1+\hat{A}_2+\hat{A}_3+\text{c.c.}\right)= \tag{2.2.6}$$
$$-\frac{i}{2k_z(\omega,k_x,k_y)}\frac{\omega^2}{c^2}\left[\chi^{(2)}_{\text{eff}}\left(\hat{A}_1+\hat{A}_2+\hat{A}_3+\text{c.c.}\right)^2+\chi^{(3)}_{\text{eff}}\left(\hat{A}_1+\hat{A}_2+\hat{A}_3+\text{c.c.}\right)^3\right],$$

where $\hat{A}_1$, $\hat{A}_2$, $\hat{A}_3$ are Fourier counterparts of the complex amplitudes, namely

$$\hat{A}_j(\omega,k_x,k_y,z)=\frac{1}{2}\int_{-\infty}^{\infty}\int_{-\infty}^{\infty}\int_{-\infty}^{\infty}A_j(t,x,y,z)e^{-i(\omega t-k_xx-k_yy)}\mathrm{d}t\mathrm{d}x\mathrm{d}y. \tag{2.2.7}$$

By expanding the nonlinear terms in Eq. (2.2.6), we would expose a vast diversity of possible parametric processes. After the expansion, each term would have its definite carrier frequency. Recall that carrier frequency defines the position of the temporal spectrum along the ω axis. Thus, different parametric processes can be identified by the carrier frequency of the particular term. In what follows, we retain just the terms with the carrier frequencies of the initial waves (ω_1, ω_2, ω_3). Obviously, other parametric three and four wave mixing processes, like second or third harmonic generation ($2\omega_1=\omega_1+\omega_1$, $3\omega_1=\omega_1+\omega_1+\omega_1$ etc.), may also take a place simultaneously. However, they are omitted, assuming that they are not phase-matched, and thus, are not sustained during the nonlinear propagation. Note that any number of the simultaneous parametric processes can be readily taken into account by complementing the Eq. (2.1.29) with additional constituents.

Note that, despite the introduced complex amplitudes in Eq. (2.2.6), there is no approximation implemented yet, and it is as accurate as Eq. (2.1.21). The SVEA is applied after the nonlinear terms in Eq. (2.2.6) are expanded, and for

each resulted term the approximate coefficient is established, just as in Eq. (2.2.5).

In the following, the term accounting for linear propagation of the waves is omitted for convenience, since on the basis of the split-step method [64], employed throughout this work, the linear propagation of the the waves is treated independently from the nonlinearity of the material and vice versa.

Finally, by Fourier transforming Eq. (2.2.6) back into space-time domain, and assuming that $\omega_3 = \omega_1 + \omega_2$, which just represents the energy conservation in case of three-wave parametric interaction, we obtain the following set of coupled differential equations

$$\begin{aligned}
\frac{\partial A_1}{\partial z} &= -i\frac{\omega_1^2}{2k_1c^2}\chi^{(2)}_{\mathrm{eff}_{32}}A_3A_2^* - i\frac{\omega_1}{c}\left(n_{2_1}I_1 + 2n_{2_{12}}I_2 + 2n_{2_{13}}I_3\right)A_1,\\
\frac{\partial A_2}{\partial z} &= -i\frac{\omega_2^2}{2k_2c^2}\chi^{(2)}_{\mathrm{eff}_{31}}A_3A_1^* - i\frac{\omega_2}{c}\left(n_{2_2}I_2 + 2n_{2_{21}}I_1 + 2n_{2_{23}}I_3\right)A_2,\\
\frac{\partial A_3}{\partial z} &= -i\frac{\omega_3^2}{2k_3c^2}\chi^{(2)}_{\mathrm{eff}_{12}}A_1A_2 - i\frac{\omega_3}{c}\left(n_{2_3}I_3 + 2n_{2_{31}}I_1 + 2n_{2_{32}}I_2\right)A_3,
\end{aligned} \tag{2.2.8}$$

where I_j is the intensity of the wave $I_j = \frac{1}{2}n_jc\varepsilon_0|A_j|^2$, n_j is the refractive index of the medium, n_{2_j} is the nonlinear refractive index $n_{2_j} = \dfrac{3\chi^{(3)}_{\mathrm{eff}_j}}{4n_j^2c\varepsilon_0}$, and $n_{2_{jk}}$ is the nonlinear refractive index $n_{2_{jk}} = \dfrac{3\chi^{(3)}_{\mathrm{eff}_{jk}}}{4n_jn_kc\varepsilon_0}$ due to cross-phase modulation. Thus, we have obtained a coupled three-wave equations, describing three-wave parametric interaction under SVEA, and, in addition, self-phase as well as cross-phase modulation encountered by each wave due to Kerr nonlinear optical effect.

Note that in Eq. (2.2.8) each effective susceptibility is designated for each nonlinear interaction individually, as it is indicated by the subscripts. However, typically it is assumed, that

$$\chi^{(2)}_{\mathrm{eff}_{32}} = \chi^{(2)}_{\mathrm{eff}_{31}} = \chi^{(2)}_{\mathrm{eff}_{12}} = \chi^{(2)}_{\mathrm{eff}}, \tag{2.2.9}$$

and

$$\chi^{(3)}_{\mathrm{eff}_1} = \chi^{(3)}_{\mathrm{eff}_2} = \chi^{(3)}_{\mathrm{eff}_3} = \chi^{(3)}_{\mathrm{eff}_{jk}} = \chi^{(3)}_{\mathrm{eff}}. \tag{2.2.10}$$

In numerical experiments of Sects. 4.3 and 5.3, the simulations of nonlinear

propagation and parametric amplification of the waves are based on Eq. (2.2.8). Yet a different approach is taken in Sect. 5.4, where numerical experiments of four-wave mixing were performed using a single equation (Eq. (2.1.21)) and without the need to adopt the SVEA discussed above.

2.3 Accounting for parabolic mirror in non-paraxial case

Almost every experiment in optics inevitably involves such optical elements as curved mirrors or refractive lenses. However, in the model of forward-propagating plane waves the medium is restricted to be with no sharp optical interfaces crossing the z axis. Therefore, the reflection from the surface of the mirror or refraction at the surface of the lens could not be actually simulated. Instead, the effect of such optical elements is taken into account by applying a particular spatial phase modulation $\phi(r)$ to the incident beam. In the following, we provide with the derivation of the phase modulation function $\phi(r)$ in case of parabolic mirror.

Let's consider a plane wave propagating parallel to the z axis and incident upon the parabolic mirror. It can be proved by means of geometrical optics, that all the parts of the plane wave, coming from the different positions off the mirror, will meet simultaneously at a single point, that is, at the focus of the parabolic mirror. This is a very special thing about the parabolic mirror, implying that a plane wave, propagating parallel to the z axis, becomes spherical after the reflection from the mirror (Fig. 2.2a, dashed line). Due to the acquired spherical wavefront, the plane wave will be focused to a single spot. In case of geometrical optics it would be depicted by the rays, directed towards a single point.

This feature is of paramount importance, empowering to achieve nearly diffraction limited beam diameters at the focus. In addition, this feature should be beard in mind when focusing a spatially dispersed pulsed beam (Sect. 3.3). In this case it is essential to realize, that despite the fact that the beams of different frequencies take a different paths towards the focus, they all meet simultaneously at the focus. Hence, no temporal chirp is generated in this case, and thus at the focus

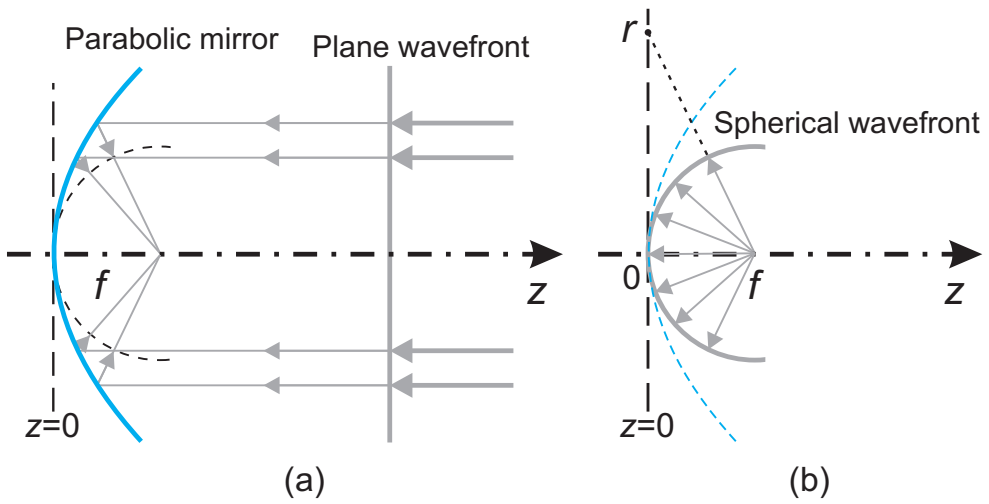

Figure 2.2: Schematic representation of the plane wave incident on the parabolic mirror (a), and of a spherical wave diverging from the focus (b). The plane, at which the spatial phase modulation $\phi(r)$ is applied in the forward-propagating plane wave model, is denoted by $z = 0$. In (a) dashed circular line depicts a spherical wavefront, acquired by the plane wave after the reflection from the parabolic mirror. f denotes the focal length of the parabolic mirror.

the pulse preserves its transform-limited duration.

In order to account for parabolic mirror in a forward-propagating wave model, the ultimate question is: what is the function of the spatial phase modulation $\phi(r)$, that should be applied to the plane wave, awaiting at $z = 0$, in order to properly simulate the propagation towards the focus of the plane wave, which was reflected by the mirror? And the answer is quite simple: the spatial phase modulation can be retrieved by speculating of what would be the phase at each point r in plane $z = 0$ of the reflected wavefront, if after the reflection it was propagated backwards.

In case of parabolic mirror and a plane wave parallel to z axis, the reflected wavefront is spherical, converging towards the focus (Fig. 2.2a). Therefore, the spatial phase modulation $\phi(r)$ is found by observing the phase at each point r in plane $z = 0$ of a spherical wave diverging from the focus (Fig. 2.2b). It can be done by geometrical considerations, since in geometrical optics a wavefront actually represents continuum of the rays, which are perpendicular to each point of the wavefront. As it can bee seen from Fig. 2.2b, the function of the phase modulation $\phi(r)$, that is, the phase difference between the point $r = 0$ and any

other point r in plane $z = 0$ is equal to

$$\phi(r) = \pm k \left(\sqrt{f^2 + r^2} - |f| \right), \tag{2.3.1}$$

where the sign "+" corresponds to the concave parabolic mirror, i.e. when $f > 0$, and the sign "−" to convex mirror ($f < 0$). This is our desired result.

We should note that in all the textbook it is typically assumed, that $r \ll f$, in which case Eq. (2.3.1) becomes simply

$$\phi(r) = k \frac{r^2}{2f}. \tag{2.3.2}$$

Thus, we have obtained a well-known formula for the thin lens. Note that the validity of this formula is restricted to a so-called paraxial approximation. Actually, the $r \ll f$ condition is fulfilled in most of the practical situations, if the beam is positioned on the z axis. However, if the off-axis beam, incident on the parabolic mirror, is considered, for example when focusing a ring-shaped beam, then discrepancies arises and Eq. (2.3.1) should be used instead. In any case, the paraxial lens formula (Eq. (2.3.2)) should be used in tandem with paraxial approximation for the propagation vector (Eq. (2.2.1)).

In addition, if a quasi-monochromatic approximation is applied, namely, if it is assumed that $\Omega \ll \omega_{\mathrm{R}}$, the magnitude of the wave vector in Eq. (2.3.2) is approximated as $k = \dfrac{\omega_{\mathrm{R}} + \Omega}{c} \approx \dfrac{\omega_{\mathrm{R}}}{c}$, and in such case the phase modulation becomes

$$\phi(r) = k_{\mathrm{R}} \frac{r^2}{2f}, \tag{2.3.3}$$

where k_{R} is the magnitude of the wave vector corresponding to the reference frequency $k_{\mathrm{R}} = \dfrac{\omega_{\mathrm{R}}}{c}$.

It should be noted that the validity of Eq. (2.3.1) is restricted to the case of plane wave parallel to the z axis and incident on the parabolic mirror. However, in practice we consider beams that consists of many plane waves, of which just one is actually parallel to the z axis. Therefore, Eq. (2.3.1) should be considered

as an approximation for the beams with a narrow angular spectrum.

Lastly, we should note that throughout the text of this thesis it is usually referred to the lens instead of parabolic mirror, however, when it comes to modeling it is always assumed to be a parabolic mirror.

Chapter 3

Pulsed Gaussian beams containing first-order spatio-temporal couplings

The propagation dynamics of space-time coupled wave packets has recently became a major issue of laser physics. Pulsed light beams are said to exhibit spatio-temporal couplings (STCs) when their spatial properties depend on time, and vice versa. The importance of STCs has been largely overlooked in most laser-matter interaction experiments. In strong-field science, STCs are even considered as highly detrimental, because they decrease the peak intensity at the focus. The significance of these effects largely depends on the application, and pulsed beam parameters as well, and while STCs may be negligible in some cases, they are detrimental in others. STCs commonly result due to mismatched fronts of pump and signal pulses in NOPA [15, 16, 19, 20] or from misalignments in CPA stretcher-compressor [65, 66, 67] and seem undesirable. In such case they are referred as spatio-temporal distortions. However on the other hand, they can be viewed as an additional, controllable pulsed beam parameter and become quite useful [30, 31, 32, 33, 34, 35, 36, 37]. For the comprehensive review and deeper introduction into this field the reader is referred to [68].

Although S. Akturk and R. Trebino et. al. [38, 39, 40, 41] have made a great contribution in identifying and understanding the relations between the different

STCs, yet, the spatio-temporal transformations, experienced by the pulsed light beams containing STCs, while propagating through linear optical systems has not been well explored. This chapter is intended to fill this gap and to provide an intuitive understanding of the behavior of pulsed light beams possessing STCs. It should be considered as a short course of linear optics necessary for proper interpretation of the results presented in the following chapters of the thesis. Here the basic characteristics of pulsed Gaussian beams containing STCs are investigated in case when they are propagating in free space and when focused by the lens.

Different methods for analytical treatment of this problem has been presented, either using Gaussian beam model [69, 70, 71] or the model of extended ABCD matrices [72, 40]. In this chapter we have employed a Gaussian beam model, as it seemed to be more intuitive to follow. However, note that restrictions to the pulse bandwidth and beam paraxiality are unavoidable in these analytical approaches.

Simply by Fourier transforming the spatio-temporal profile of the pulsed beam, we can obtain the corresponding profiles in four characteristic space and time domains, from which a comprehensive deductions about the STCs can be made. Besides the well-familiar spatio-temporal domain (t, x), the intensity distribution of the pulsed beam can be depicted in three additional domains, namely in the spatio-spectral domain (ω, x), in the spatio-temporal spectrum domain (ω, k_x), and in the spatial spectrum domain (t, k_x). This is illustrated in Fig. 3.5. All the four domains are related by the Fourier transformation, therefore spatio-temporal coupling introduced in one domain will necessarily has effect in another domain as well. Consequently, only two independent STCs exists overall [40].

As indicated in [38, 40], there are two distinct approaches to characterize each STC, and both give a proper description of the coupling under investigation. For example, in the ω-x domain (Fig. 3.5b) if we measure the center position at each frequency, then the measured parameter is the spatial dispersion, on the contrary, if we measure the center frequency at each position, then the measured parameter

is frequency gradient. The characterization of the STCs is explained at a greater detail in the subsequent section.

3.1 Characterization of the tilted pulsed Gaussian beams

The purpose of this section is to obtain a handy expressions for the characterization of the STCs in case of pulsed Gaussian beam. The obtained expressions will be used throughout the following sections of this chapter.

In the following, the profile of the tilted pulsed Gaussian beam is considered in the t-x domain, however, it is essential to realize that the same analysis applies for the profiles, depicted in the distinct spatio-temporal domains, i.e. for characterization of the spatial chirp (ω-x domain), angular chirp (ω-k_x domain) and angle vs. time (t-k_x domain). In what follows, the two characteristic parameters are derived.

The intensity profile of the pulsed Gaussian beam, possessing linear tilt in the t-x plane, reads

$$I(t,x,y) = I_{\text{peak}} \exp\left(-2\frac{(t-p_{\text{pt}}x)^2}{\tau^2} - 2\frac{x^2}{\rho_x^2} - 2\frac{y^2}{\rho_y^2}\right), \tag{3.1.1}$$

where I_{peak} is the peak intensity, τ and ρ_x, ρ_y are the parameters characterizing pulse duration and beam diameter, respectively, and p_{pt} is the parameter characterizing pulse tilt. It is readily seen from Eq. (3.1.1), that the function of the iso-intensity contour in t-x plane can be written in the general form as follows

$$-At^2 + Btx - Cx^2 = -\text{m}_\text{I}, \tag{3.1.2}$$

where A and C are positive real numbers, B is the real number, which defines the coupling between t and x domains, and m_I defines the intensity level of the iso-intensity contour as $I_{\text{peak}} \exp(-\text{m}_\text{I})$. Thus, for the iso-intensity contour, corresponding to the half-maximum intensity, $\text{m}_\text{I} = \ln 2$.

There are two distinct ways to determine the tilt of the pulsed beam, namely, by observing the delay of the pulse at each transverse position $t_0(x)$ (Fig. 3.1,

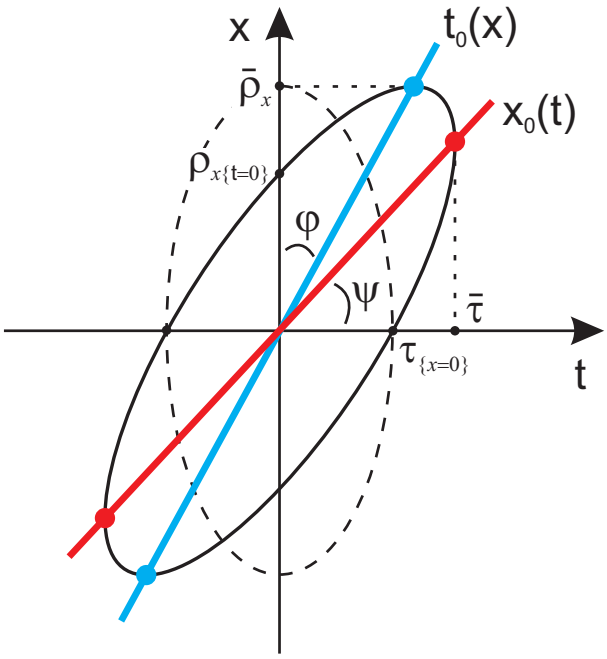

Figure 3.1: Iso-intensity contour of the pulsed Gaussian beam, tilted ($p_{\mathrm{pt}} > 0$) in the t-x domain (black line). The dashed contour represents initially untilted pulsed beam. Straight lines show the two distinct approaches to characterize the tilted pulsed beam. Filled circles correspond to the most-distant points of the iso-intensity contour.

blue line), or by observing the position of the beam at each moment of time $x_0(t)$ (Fig. 3.1, red line). Depending on the chosen approach, the tilt of the pulsed beam can be characterized by two distinct parameters $\tan\phi = \dfrac{\mathrm{d}t_0}{\mathrm{d}x}$ and $\tan\psi = \dfrac{\mathrm{d}x_0}{\mathrm{d}t}$. These two characteristic parameters can be obtained from geometrical considerations as follows.

Since we have assumed that the tilt of the pulsed beam is linear, the straight line $t_0(x)$, connecting two the most-distant points of the iso-intensity contour along the x axis, can be obtained by differentiating Eq. (3.1.2) with respect to t and then solving it for t. Similarly, the straight line $x_0(t)$, connecting two the most-distant points along the t axis, can be obtained by differentiating Eq. (3.1.2) with respect to x and then solving it for x. In the former case we would obtain

$$t_0(x) = \frac{B}{2A}x, \tag{3.1.3}$$

and in the later

$$x_0(t) = \frac{B}{2C}t. \tag{3.1.4}$$

Hence, the slopes of these straight lines, i.e. the two characteristic parameters for the tilted pulsed beam are

$$\tan\phi = \frac{B}{2A}, \tag{3.1.5}$$

$$\tan\psi = \frac{B}{2C}. \tag{3.1.6}$$

This is the desired result of this section.

For illustrative purpose, in the following we obtain the expression for the pulse-front tilt angle ϕ of the tilted pulse. After expanding the exponent in the Eq. (3.1.1), we may obtain the expressions for A, B, C coefficients

$$A = 2\tau^{-2}, \quad B = 4p_{\mathrm{pt}}\tau^{-2}, \quad C = 2\rho_x^{-2} + 2p_{\mathrm{pt}}^2\tau^{-2}. \tag{3.1.7}$$

Thus, from Eq. (3.1.5) we can see, that the slope of the pulse front with respect to the phase front is simply

$$\tan\phi = p_{\mathrm{pt}}. \tag{3.1.8}$$

However it is important to note, that ϕ angle was defined in the t-x domain, and as a result the actual value of this angle depends on the scales of t and x axes. Therefore, the comparison of two ϕ angles, obtained in the different scales of t or x axes, is inconvenient or might be even impossible, when the scales for one of the angles are unknown. In order to avoid such situation, commonly, the pulse-front tilt angle ϕ is defined in the z-x domain. For such purpose, t must be replaced by $-z/c$ in Eq. (3.1.1), where c is the speed of light in vacuum. In such case Eq. (3.1.8) becomes

$$\tan\phi = -cp_{\mathrm{pt}}. \tag{3.1.9}$$

Once again, note that the same generalized expressions of the $\tan\phi$ and $\tan\psi$ would be obtained if the iso-intensity contour was analyzed in another spatio-temporal domain, for example ω-x, ω-k_x or t-k_x. In this sense, these expressions are universal and can be applied for characterization of distinct first-order spatio-temporal couplings of the pulsed Gaussian beams. In particular, parameters char-

acterizing pulse tilt p_{pt}, spatial dispersion p_{sd}, angular dispersion p_{ad} and angle vs. time p_{at} are obtained as

$$p_{\mathrm{pt}} = \tan\phi_{t\text{-}x} = \frac{B_{t\text{-}x}}{2A_{t\text{-}x}}, \qquad p_{\mathrm{sd}} = \tan\psi_{\omega\text{-}x} = \frac{B_{\omega\text{-}x}}{2C_{\omega\text{-}x}}, \tag{3.1.10}$$
$$p_{\mathrm{ad}} = \tan\psi_{\omega\text{-}k_x} = \frac{B_{\omega\text{-}k_x}}{2C_{\omega\text{-}k_x}}, \qquad p_{\mathrm{at}} = \tan\psi_{t\text{-}k_x} = \frac{B_{t\text{-}k_x}}{2C_{t\text{-}k_x}},$$

where the corresponding domains are denoted in the subscripts.

Yet, in order to fully characterize the tilted pulsed Gaussian beam, we have to consider its overall and local dimensions [40]. The overall duration (half-width) $\bar{\tau}$ and overall radius $\bar{\rho}_x$ of the tilted pulsed Gaussian beam are depicted in Fig. 3.1. In order to obtain the general expressions of these parameters, recall, that the straight lines defined by Eqs. (3.1.3) and (3.1.4) determine the position of the most-distant points of the iso-intensity contour, along the corresponding axis. Hence, by substituting Eq. (3.1.3) into Eq. (3.1.2) and then solving it for x we obtain the radius $\bar{\rho}_x$, and by performing similar steps with Eq. (3.1.4) we obtain the duration $\bar{\tau}$ as given below

$$\bar{\tau} = 2\sqrt{\frac{C\mathrm{m_I}}{4AC - B^2}}, \tag{3.1.11}$$

$$\bar{\rho}_x = 2\sqrt{\frac{A\mathrm{m_I}}{4AC - B^2}}. \tag{3.1.12}$$

By substitution of Eq. (3.1.7) into the obtained equations, the overall duration and radius of the tilted pulsed Gaussian beam, defined by Eq. (3.1.1), evaluate to

$$\bar{\tau} = \sqrt{\tau^2 + \rho_x^2 p_{\mathrm{pt}}^2}, \tag{3.1.13}$$

$$\bar{\rho}_x = \rho_x. \tag{3.1.14}$$

Here the duration and diameter are given at $\mathrm{m_I} = 2$ intensity level, i.e. at $I_{\mathrm{peak}}\mathrm{e}^{-2}$. The corresponding local parameters, i.e. the duration $\tau_{\{x=0\}}$ at $x = 0$ and the

radius $\rho_{x\{t=0\}}$ at $t = 0$ are obtained directly from Eq. (3.1.1) and evaluate to

$$\tau_{\{x=0\}} = \tau, \tag{3.1.15}$$

$$\rho_{x\{t=0\}} = \rho_x \frac{\tau}{\bar{\tau}}. \tag{3.1.16}$$

In addition, assuming that the total energy of the pulsed Gaussian beam is preserved during the physical process after which it becomes tilted in t-x plane, the peak intensity can be obtained from

$$I_{\text{peak}} = I_0 \frac{\tau_0}{\tau} \frac{\rho_{x0}}{\bar{\rho}_x} \frac{\rho_{y0}}{\rho_y}, \tag{3.1.17}$$

where I_0, τ_0, ρ_{x0}, ρ_{y0} are the peak intensity, duration and radii of the initial untilted pulsed Gaussian beam.

Finally, by evaluating the pulsed Gaussian beam propagation through the arbitrary optical system, the explicit expressions of the A, B, C coefficients can be obtained. After substituting into the obtained equations, the peculiar dependencies can be obtained and the critical parameters can be identified. Such analysis is performed in the following two sections for the particular optical setups.

3.2 Focusing of pulsed Gaussian beams possessing angular dispersion

Angular dispersion, or more precisely, angularly dispersed pulses are frequently encountered in optical systems. The most common angularly dispersive optical elements are prisms and gratings, usually used in pulse stretchers and compressors. As it is demonstrated in Sect. 3.3, the lens also becomes a source of angular dispersion, in case when the pulsed beam is spatially dispersed in the front of it. In practice, due to slight misalignments in pulse stretchers or compressors the pulse usually contains some residual angular dispersion, which may lead to the tilted pulse front in the near field and to the reduced peak intensity at the focus [65, 66, 67].

In this section we are interested in the spatio-temporal dynamics of the pulsed Gaussian beam after being passed through angularly dispersive optical element and then focused by the lens. The optical scheme under consideration is depicted in Fig. 3.2.

Actually, focusing of angularly dispersed pulses was theoretically studied in Ref. [73]. It was shown, that at the focus the temporal profile is independent of the initial pulse profile, but rather is determined by the profile of the initial beam. In addition it was shown, that at the focus the pulse duration is defined by the initial diameter of the beam and the angular dispersion, but does not depend on the initial duration of the pulse. However, the results of this work are valid only for the case of transform-limited pulses and, in addition, when the pulse duration is much shorter than the pulse-front-tilt-time, i.e. than the overall duration of the tilted pulsed beam. Moreover, it was assumed that the angularly dispersive element is placed close to the lens, thus the spatial dispersion, acquired during the propagation from the angularly dispersive element to the lens, was ignored.

In the following study, we consider the optical scheme, where angularly dispersed pulsed Gaussian beam propagates an arbitrary distance z_1 before it is being focused by the lens (Fig. 3.2). It is shown, that this distance is of particular importance, as depending upon this distance, different spatio-temporal couplings are involved in the propagation towards the focus.

In the special case, when $z_1 = f$, i.e. when this distance is equal to the focal length of the lens, the scheme is exploited in spatially dispersive amplification of ultrashort laser pulses [74, 75, 76, 77]. The basic idea of such amplifiers is to overcome the gain narrowing by introducing artificial inhomogeneous broadening. This is achieved by placing the amplifier in the back focal plane of the lens, where individual wavelength components are decoupled from one another inside the gain medium, i.e. they are spatially dispersed.

This scheme, could also be regarded as a stretcher-compressor, especially, for picosecond pulses, since due to narrow bandwidth the stretching in time of these

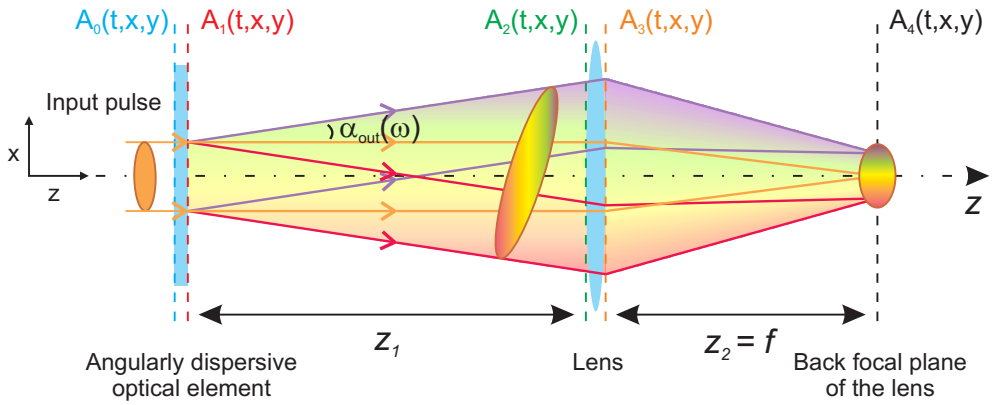

Figure 3.2: Schematic representation of the angularly dispersed pulsed beam being focused by a lens. It depicts a particular situation, when at the input the pulsed beam is transform- and diffraction-limited. Thus at the back focal plane of the lens the pulsed beam is not tilted, however, in addition to the angular dispersion, possesses the spatial chirp (see text for more details). z_1 denotes the distance from the angularly dispersive optical element to the lens, f - focal length of the lens, $\alpha_{\text{out}}(\omega)$ - the frequency dependent propagation angle of the beam. Vertical dashed lines denote the planes, at which the spatio-temporal profiles of the pulsed beam were obtained and depicted in Fig. 3.5.

pulses is hardly achieved by the usual means (pair of gratings, prisms etc). However, it is important to note that in this stretcher, the pulse remains stretched only at the focus. Nevertheless, such stretching method has been applied for amplification of bandwidth-limited 15 ps pulses, after stretching them to 200 ps [78]. Yet, there was no theoretical explanation given of what actually causes the pulse lengthening at the focus, and the given expression for pulse duration was based just on geometrical considerations.

In this section we present theoretical results, revealing the spatio-temporal couplings, that are involved, and the dynamics of the spatio-temporal profile of the angularly dispersed pulsed beam while it evolves through the optical scheme depicted in Fig. 3.2. In addition, the analytical expression for the pulse duration at the back focal plane of the lens is obtained from the theoretical considerations of pulsed Gaussian beam propagation. Therefore, it is considerably more accurate than the ones, obtained by means of geometrical considerations in the previous works.

At the input of the optical scheme we consider a pulsed Gaussian beam possessing a linear temporal chirp. In such case, the complex amplitude of the initial

pulsed Gaussian beam reads

$$A_0(t,x,y) = a_0 \exp\left(-\frac{t^2}{\tau_0^2}(1-i\gamma_{t0}) - \frac{x^2}{\rho_{x0}^2}(1-i\gamma_{x0}) - \frac{y^2}{\rho_{y0}^2}(1-i\gamma_{y0})\right), \quad (3.2.1)$$

where a_0 is the peak amplitude of the electric field, τ_0 is the half-width duration of the initial pulse, ρ_{x0}, ρ_{y0} are the initial radii of the beam in x and y directions, respectively, γ_{t0} is the parameter characterizing the initial linear temporal chirp, and γ_{x0}, γ_{y0} are the parameters characterizing the initial phase-front curvature of the beams in x and y directions, respectively.

For the Gaussian pulses the temporal chirp parameter γ_{t0} may be expressed as

$$\gamma_{t0} = \pm\sqrt{\frac{\tau_0^2}{\tau_{TL}^2} - 1}, \quad (3.2.2)$$

where τ_{TL} is the half-width duration of the transform-limited pulse, the sign "+" corresponds to positively chirped pulse, that is, when the high-frequency component lags behind the low-frequency component, and the sign "−" corresponds to negatively chirped pulse.

Similarly, the phase-front curvature parameters γ_{x0} and γ_{y0} in case of Gaussian beams may be expressed as

$$\gamma_{x0} = \pm\sqrt{\frac{\rho_{x0}^2}{\rho_{xDL}^2} - 1}, \qquad \gamma_{y0} = \pm\sqrt{\frac{\rho_{y0}^2}{\rho_{yDL}^2} - 1}, \quad (3.2.3)$$

where ρ_{xDL}, ρ_{yDL} are the diffraction-limited radii of the beam in the corresponding directions, the sign "+" corresponds to converging phase-front of the beam, and the sign "−" corresponds to diverging phase-front. Other handy expressions of γ_{x0} and γ_{y0} parameters are

$$\gamma_{x0} = \frac{z_{Rx}}{f_x}, \qquad \gamma_{y0} = \frac{z_{Ry}}{f_y}, \quad (3.2.4)$$

where f_x and f_y are the focal lengths of the cylindrical lenses being placed in front of the beam; positive focal length ($f_x, f_y > 0$) corresponds to positive (converging) lens and negative ($f_x, f_y < 0$) corresponds to negative (diverging) lens; z_{Rx} and

z_{Ry} are the Rayleigh lengths corresponding to the initial beam radii in x and y directions, respectively,

$$z_{Rx} = \frac{k_0 \rho_{x0}^2}{2}, \qquad z_{Ry} = \frac{k_0 \rho_{y0}^2}{2}. \tag{3.2.5}$$

At first, the pulse is incident on the angularly dispersive element. In the following analysis the angularly dispersive element is treated as a thin optical element, i.e. it is assumed that beam diffraction as well as pulse dispersion inside this element is insignificant. As it is depicted in Fig. 3.2, the angularly dispersive element gives rise to deflection of an incident beam with an output angle α_{out}, which depends on the temporal frequency ω of the beam. Note that, after the angularly dispersive element, the propagation direction of the beam with the central frequency ω_0 is taken as a reference for the propagation direction of the whole angularly dispersed pulsed beam, thus $\alpha_{\text{out}}(\omega_0) = 0$.

Actually, it is more convenient to work with the projections of the wave vectors onto the x axis instead of output angles. The projection of the wave vector onto the x axis is simply

$$k_{x_{\text{out}}}(\omega) = k(\omega) \sin\left(\alpha_{\text{out}}(\omega)\right), \tag{3.2.6}$$

where $k(\omega) = \dfrac{\omega}{c}$, and α_{out} is the angle between the z axis and the propagation direction of the wave vector in free space.

In general, the function of the angular dispersion $\alpha_{\text{out}}(\omega)$ can be of the arbitrary form. However, in the following analysis we shall assume that the angular dispersion, imposed by the angularly dispersive element, is such that the $k_{x_{\text{out}}}(\omega)$ function is linear. Thus, we restrict the imposed angular dispersion to the case when Eq. (3.2.6) can be rewritten as

$$k_{x_{\text{out}}}(\omega) = k_{x_{\text{out}}}(\omega_0) + k'_{x_{\text{o}}}\Omega, \tag{3.2.7}$$

where $k_{x_{\text{out}}}(\omega_0)$ is actually equal to zero, since in our reference frame $\alpha_{\text{out}}(\omega_0) = 0$; Ω denotes the deviation from the central frequency $\Omega = \omega - \omega_0$; $k'_{x_{\text{o}}}$ is the first-

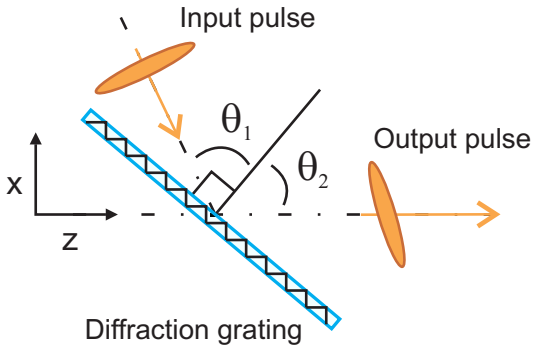

Figure 3.3: Schematic representation of the pulsed beam incident on the diffraction grating.

order derivative of $k_{x_{\text{out}}}(\omega)$

$$k'_{x_o} = \left.\frac{\mathrm{d}k_{x_{\text{out}}}}{\mathrm{d}\omega}\right|_{\omega_0} = \left.\frac{\omega_0}{c}\,\frac{\mathrm{d}\alpha_{\text{out}}}{\mathrm{d}\omega}\right|_{\omega_0} = -\left.\frac{\lambda_0}{c}\,\frac{\mathrm{d}\alpha_{\text{out}}}{\mathrm{d}\lambda}\right|_{\lambda_0}. \tag{3.2.8}$$

This assumption is justified by the fact that it is a usual assumption in optics in order to obtain the analytical expressions. Commonly, the angular dispersion, imposed by the angularly dispersive element, can be kept linear only in the narrow region of the spectrum. Therefore, such assumption implies a restriction on the pulse bandwidth, or equivalently on the duration of the transform-limited pulse, and must be justified for each experimental conditions individually.

In order to illustrate how the coefficient k'_{x_o} of the angular dispersion is actually calculated, for the moment we shall assume that the angularly dispersive element is grating (Fig. 3.3). The angular dispersion imposed by the grating can be obtained from the grating equation [79]

$$d\,(\sin\theta_2 - \sin\theta_1) = m\lambda, \tag{3.2.9}$$

where θ_1 is the angle of incidence, θ_2 is the diffracted angle, m is the diffraction order, λ is the wavelength of the incident beam, and d is the period of the grating. From the grating equation we may obtain

$$\theta_2(\lambda) = \arcsin\left(\frac{m\lambda}{d} + \sin\theta_1\right). \tag{3.2.10}$$

Thus, the output angle with respect to the beam with the central wavelength λ_0

is simply

$$\alpha_{\mathrm{out}}(\lambda) = \theta_2(\lambda) - \theta_2(\lambda_0). \tag{3.2.11}$$

By differentiating the obtained equation we have

$$\left.\frac{\mathrm{d}\alpha_{\mathrm{out}}}{\mathrm{d}\lambda}\right|_{\lambda_0} = \frac{\sin\theta_{02} - \sin\theta_{01}}{\lambda_0 \cos\theta_{02}}, \tag{3.2.12}$$

where θ_{01} and θ_{02} denote $\theta_1(\lambda_0)$ and $\theta_2(\lambda_0)$, respectively. Additionally, it was assumed that $\theta_1(\lambda) = \text{const.}$, i.e. that the incident pulsed beam has no angular dispersion. For the spacial case of Littrow configuration, when $\theta_{02} = -\theta_{01}$, it reduces to

$$\left.\frac{\mathrm{d}\alpha_{\mathrm{out}}}{\mathrm{d}\lambda}\right|_{\lambda_0} = -\frac{2}{\lambda_0}\tan\theta_{01}, \tag{3.2.13}$$

in which case Eq. (3.2.8) becomes simply

$$k'_{x_{\mathrm{o}}} = \frac{2}{c}\tan\theta_{01}. \tag{3.2.14}$$

For simplicity we assume, that the initial pulse is angularly dispersed *only* in the x direction. Thus, there is no coupling involved between y and t, nor y and x dimensions. In such case, the diffraction of the beam in y transverse direction is not affected by the pulse tilting and is actually described by a well-known formulas of Gaussian-beam propagation.

In the following study it is also assumed, that the angular spectrum of the beam in the x direction is narrow enough, meaning that the radius ρ_{xDL} of the diffraction-limited beam is large enough, so that the shape and the diameter of the monochromatic beam remains unchanged after passing the angularly dispersive element. In such case, just a linear spatial phase is added to the beam.

With the assumptions mentioned above, the effect of the angularly dispersive element is taken into account by performing the partial Fourier transformation of Eq. (3.2.1) into the spatio-spectral domain (Ω, x, y) and simply multiplying by frequency-dependent linear spatial phase, and finally transforming back to the

space-time domain

$$A_1(t,x,y) = \mathscr{F}_{\Omega}^{-1}\left\{\mathscr{F}_t\left\{A_0(t,x,y)\right\}\cdot\exp\left(-ik'_{x_\mathrm{o}}\Omega x\right)\right\}. \tag{3.2.15}$$

Thus, the complex amplitude after the angularly dispersive element becomes

$$A_1(t,x,y) = a_0\exp\left(-\frac{\left(t-k'_{x_\mathrm{o}}x\right)^2}{\tau_0^2}\left(1-i\gamma_{t0}\right)-\frac{x^2}{\rho_{x0}^2}\left(1-i\gamma_{x0}\right)-\frac{y^2}{\rho_{y0}^2}\left(1-i\gamma_{y0}\right)\right). \tag{3.2.16}$$

It is readily seen from the obtained expression, that in case when $k'_{x_\mathrm{o}} \neq 0$, the space-time coupling term "$t \cdot x$" is present in the exponent, meaning that the pulsed Gaussian beam becomes tilted.

The spatio-temporal intensity profile takes the form as given in Eq. (3.1.1). Therefore, it will not be explicitly rewritten here, just the essential parameters of the tilted pulsed Gaussian beam are provided below

$$\begin{aligned} \tau_1 &= \tau_0, & \bar{\tau}_1 &= \sqrt{\tau_0^2+\rho_{x0}^2k'^2_{x_\mathrm{o}}}, \\ \bar{\rho}_{x1} &= \rho_{x0}, & \rho_{y1} &= \rho_{y0}. \end{aligned} \tag{3.2.17}$$

Parameters, characterizing the spatio-temporal couplings, were also obtained, as defined in Eq. (3.1.10)

$$\begin{aligned} p_{\mathrm{pt1}} &= k'_{x_\mathrm{o}}, & p_{\mathrm{sd1}} &= 0, \\ p_{\mathrm{ad1}} &= k'_{x_\mathrm{o}}, & p_{\mathrm{at1}} &= -\frac{2k'_{x_\mathrm{o}}}{\bar{\tau}_1^2}\left(\gamma_{x0}-\gamma_{t0}\right). \end{aligned} \tag{3.2.18}$$

As it is readily seen, most of the pulsed beam parameters, including the peak intensity (Eq. (3.1.17)), remain unchanged after the angularly dispersive element. However, the pulsed Gaussian beam becomes tilted since $p_{\mathrm{pt1}} \neq 0$, and, in addition to the angular dispersion ($p_{\mathrm{ad1}} \neq 0$), possesses the angle vs. time, since $p_{\mathrm{at1}} \neq 0$. Note that angle vs. time essentially depends on the initial temporal chirp parameter γ_{t0} and the initial phase-front parameter γ_{x0}. Interestingly, but if these two parameters are equal, the angularly dispersed pulsed Gaussian beam being tilted in the near field becomes untilted in the far field.

The overall duration $\bar{\tau}_1$ of the tilted pulsed Gaussian beam becomes longer as it is apparent from the obtained expression, and increases with the initial radius of the beam ρ_{x0} as well as with the angular dispersion k'_{x_o}. On the other hand, the local radius ρ_{x1} at $t = 0$ becomes smaller (Eq. (3.1.16)) by the same factor

$$\rho_{x1} = \rho_{x0} \frac{\tau_0}{\sqrt{\tau_0^2 + \rho_{x0}^2 k'^2_{x_\mathrm{o}}}}. \tag{3.2.19}$$

For the tilted pulsed beams it is common to define the pulse-front tilt angle ϕ, namely, the angle between the pulse front and the phase front. It can be shown that this angle is related to the angular dispersion by [80, 81]

$$\tan\phi = -ck'_{x_\mathrm{o}} = \lambda_0 \left.\frac{\mathrm{d}\alpha_\mathrm{out}}{\mathrm{d}\lambda}\right|_{\lambda_0}. \tag{3.2.20}$$

It is important to note, however, that this relation is valid only for the case when the spatial chirp is negligible or when there is no temporal chirp and the beam is well-collimated [39, 40]. A more universal expression, which does not dependent on the origin of the tilt, is obtained by incorporating the pulse tilt parameter (see Sect. 3.1)

$$\tan\phi = -cp_\mathrm{pt}. \tag{3.2.21}$$

Obviously, these two relations are identical at the moment, as the pulse tilt is caused just by the presence of the angular dispersion, and p_pt1 is simply equal to k'_{x_o}. However, at the back focal plane of the lens, the pulse tilt will also be affected by the presence of spatial and temporal chirps and phase-front curvature as well, therefore the pulse tilt parameter will become more complex, and relation in Eq. (3.2.20) will be no longer valid.

In order to step further in the optical scheme, the propagation in free space of the angularly dispersed pulsed Gaussian beam must be calculated. The implicit expression of the complex amplitude accounting for the propagation distance z_1

in free space is

$$A_2(t,x,y) = \mathscr{F}^{-1}_{k_x,k_y}\left\{\mathscr{F}_{x,y}\left\{A_1(t,x,y)\right\}\exp\left[-i\left(k_0+\frac{\Omega}{c}-\frac{k_x^2+k_y^2}{2k_0}\right)z_1\right]\right\}. \tag{3.2.22}$$

Note that the calculations were performed under paraxial and quasi-monochromatic approximations (Eq. (2.2.4)), as otherwise an intuitive analytical expressions of the characteristic parameters of the pulsed Gaussian beam could not be obtained without supplementary assumptions.

Again the spatio-temporal intensity profile takes the form as given in Eq. (3.1.1), and the characteristic parameters of the pulsed Gaussian beam at the plane in front of the lens are

$$\begin{aligned}
\tau_2 &= \tau_0\frac{\rho_{x0}}{\bar{\rho}_{x2}}\sqrt{\left(1-\frac{z_1}{z_{Rx}}\gamma_{x0}\right)^2+\frac{z_1^2}{z_{Rx}^2}\frac{\bar{\tau}_1^4+\rho_{x0}^4k_{x_\mathrm{o}}'^4\gamma_{t0}^2}{\tau_0^4}}-\left(1-\frac{z_1}{z_{Rx}}\gamma_{x0}\right)\frac{4dk_{x_\mathrm{o}}'^2}{\tau_0^2k_0}\gamma_{t0},\\
\bar{\tau}_2 &= \bar{\tau}_1,\\
\bar{\rho}_{x2} &= \rho_{x0}\sqrt{\left(1-\frac{z_1}{z_{Rx}}\gamma_{x0}\right)^2+\frac{z_1^2}{z_{Rx}^2}\frac{\bar{\tau}_1^2+\rho_{x0}^2k_{x_\mathrm{o}}'^2\gamma_{t0}^2}{\tau_0^2}},\\
\rho_{y2} &= \rho_{y0}\sqrt{\left(1-\frac{z_1}{z_{Ry}}\gamma_{y0}\right)^2+\frac{z_1^2}{z_{Ry}^2}},
\end{aligned} \tag{3.2.23}$$

and the parameters characterizing the spatio-temporal couplings are

$$\begin{aligned}
p_{\mathrm{pt}2} &= k'_{x_\mathrm{o}}\frac{\rho_{x0}^2}{\bar{\rho}_{x2}^2}\left(1-\frac{z_1}{z_{Rx}}\left(\gamma_{x0}-\gamma_{t0}\right)\right), & p_{\mathrm{sd}2} &= z_1\frac{k'_{x_\mathrm{o}}}{k_0},\\
p_{\mathrm{ad}2} &= p_{\mathrm{ad}1}, & p_{\mathrm{at}2} &= p_{\mathrm{at}1}.
\end{aligned} \tag{3.2.24}$$

As it can bee seen, the on-axis pulse duration τ_2, i.e. pulse duration at $x, y = 0$, depends on the propagation distance z_1. This is a consequence of the angular dispersion, which gives rise to the two effects simultaneously, namely, the lateral and temporal walk-off of the spectral components. Thus, during the propagation the angularly dispersed pulsed beam acquires both spatial chirp and temporal chirp. Nevertheless, the overall pulse duration $\bar{\tau}_2$ does not change during the propagation, despite the fact that its spatio-temporal profile is consistently changing, as

it is apparent from the expression of p_{pt2}.

It is important to note, that during the propagation the angularly dispersed pulsed beam acquires a negative temporal chirp (a more detailed discussion is provided in Sect. 5.5). This is a consequence of the angular dispersion, which causes a negative GVD during the propagation in free space independently from the sign of k'_{x_o}, as it is shown in the equation below

$$g = \left.\frac{\mathrm{d}^2 k_z}{\mathrm{d}\omega^2}\right|_{\omega_0} = \frac{\mathrm{d}^2}{\mathrm{d}\omega^2}\left(k_0 + \frac{\Omega}{c} - \frac{k_{x_\mathrm{out}}^2}{2k_0}\right)\Bigg|_{\omega_0} = \frac{\mathrm{d}^2}{\mathrm{d}\omega^2}\left(-\frac{\left(k'_{x_\mathrm{o}}\Omega\right)^2}{2k_0}\right)\Bigg|_{\omega_0} = -\frac{k'^2_{x_\mathrm{o}}}{k_0}. \tag{3.2.25}$$

Therefore, if the pulsed beam has a positive temporal chirp at the input ($\gamma_{t0} > 0$), it undergoes a temporal compression. However, a transform-limited duration cannot be achieved due to simultaneous lateral walk-off of the spectral components. Therefore, at some distance the pulse duration reaches its minimal value, but it will be greater than the transform-limited duration. Naturally, for the wider beams the lateral walk-off is less significant and, at the particular distance, the τ_2 duration should be nearly transform-limited. It can be shown, that the distance, at which the on-axis duration becomes minimal, is equal to

$$z_{1_{\min(\tau_2)}} = \gamma_{t0} z_{Rx} \frac{\tau_0^2}{\bar{\tau}_1^2 + \tau_0^2 \gamma_{t0}\gamma_{x0} + \rho_{x0}^2 k'^2_{x_\mathrm{o}} \gamma_{t0}^2}. \tag{3.2.26}$$

The dependence of τ_2 duration on the propagation distance is depicted in Fig. 3.4a,b for the three different initial beam diameters. As it can bee seen from Fig. 3.4a, after the point of temporal focus, where the minimal duration is achieved, the pulse duration increases. However, this increase is confined by the acquired spatial chirp, which grows with the propagation distance z_1 (see Eq. (3.2.24)) and has an opposite effect on the pulse duration. In detail, due to the spatial chirp, the beam fronts of different frequencies are shifted with respect to each other in the transverse direction, thus inducing the positive temporal chirp (see the comments below Eq. (3.3.5)). Consequently, the magnitude of the negative temporal chirp is gradually reduced. Thus, depending upon the initial

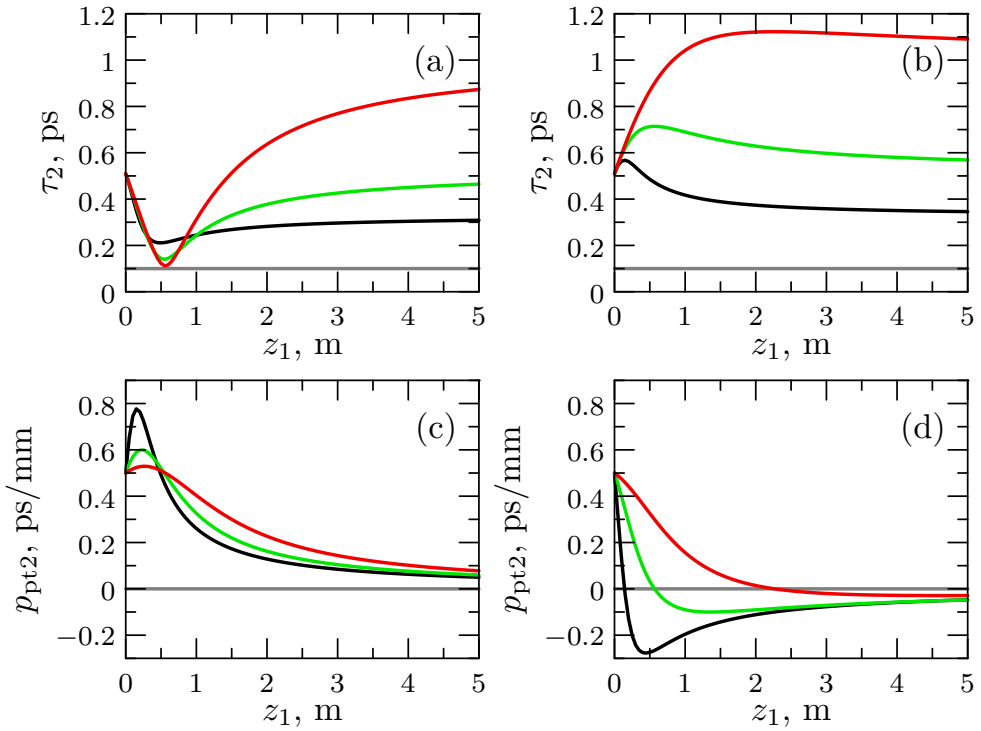

Figure 3.4: Variation of the on-axis duration (FWHM) (a) and (b), and of the pulse tilt parameter (c) and (d) of the angularly dispersed pulsed Gaussian beam during propagation in free space, for the case of three different diameters (FWHM) of the initial beam, namely 0.5 mm (black line), 1 mm (green line) and 2 mm (red line). In (a) and (c) graphs the initial temporal chirp parameter was $\gamma_{t0} = 5$, whereas in (b) and (d) graphs it was $\gamma_{t0} = -5$. The transform-limited duration (FWHM) was $\tau_{\mathrm{TL}} = 100$ fs (it is depicted by horizontal gray solid line in (a) and (b) graphs), the angular dispersion was $k'_{x_o} = 0.5$ ps/mm, the parameter of the phase-front curvature was $\gamma_{x0} = 0$, and the central wavelength was $\lambda_0 = 0.8$ μm.

diameter of the beam, the pulse duration may become shorter after some propagation distance even in the case when $\gamma_{t0} < 0$ (Fig. 3.4b, black line), i.e. in the case when the sign of the initial temporal chirp coincides with the sign of the temporal chirp, resulting from the angular dispersion.

As it is apparent from Eq. (3.2.24), in case when $\gamma_{t0} \neq \gamma_{x0}$ the angularly dispersed pulsed Gaussian beam has all the four spatio-temporal couplings. However, as it can be seen from the inspection of the p_{pt2} expression, after some intermediate variation, the tilt of the pulsed Gaussian beam gradually disappears with the increasing propagation distance z_1. Such behavior can be seen from Fig. 3.4c, where p_{pt2} is depicted as a function of the propagation distance for the case when $\gamma_{t0} > \gamma_{x0}$. Yet a more spectacular evolution of the spatio-temporal profile is in case when the pulsed Gaussian beam has a temporal chirp at the input such that

$\gamma_{t0} < \gamma_{x0}$. In this case the pulse tilt vanishes, or more precisely, changes the sign, at the particular distance (Fig. 3.4d), which is equal to

$$z_{1_{p_{\mathrm{pt2}}=0}} = \frac{z_{Rx}}{\gamma_{x0} - \gamma_{t0}}. \tag{3.2.27}$$

At this propagation distance the pulse gathers its maximal duration as in Fig. 3.4b, which is actually equal to the overall pulse duration $\bar{\tau}_1$. In addition, note that at this distance the pulse is not tilted, even though it has the angular dispersion. Such a case can be explained by recalling, that the simultaneous presence of the spatial chirp, and temporal chirp or phase-front curvature of the beam, also contributes to the pulse tilt [39, 40]. In order to illustrate that, expression of the p_{pt2} could be rewritten in a more suggestive form

$$p_{\mathrm{pt2}} = \frac{\rho_{x0}^2}{\bar{\rho}_{x2}^2}\left(p_{\mathrm{ad2}} - 2p_{\mathrm{sd2}}\frac{\gamma_{x0} - \gamma_{t0}}{\rho_{x0}^2}\right). \tag{3.2.28}$$

Now, having in mind that the signs of the p_{ad2} and p_{sd2} are always the same, and that p_{sd2} increases with the propagation distance, it can be seen, that in case when $\gamma_{t0} < \gamma_{x0}$ the pulse-front tilt caused by the angular dispersion p_{ad2} is counterweighted at the particular distance by the pulse tilt, resulting from the spatial chirp. Note that for the greater diameter of the initial beam a longer propagation distance is required, since the effect of the spatial chirp is less significant in this case (Fig. 3.4d, red line).

For the beam of the particular temporal frequency ω, the traverse position at the plane in front of the lens is determined simply by $x_0(\Omega) = p_{\mathrm{sd2}}\Omega = z_1\frac{k'_{x_o}\Omega}{k_0}$. This relation has an obvious geometrical explanation, since $\frac{k'_{x_o}\Omega}{k_0} = \sin\alpha_{\mathrm{out}}(\Omega)$, and in the paraxial case $\sin\alpha_{\mathrm{out}} \approx \tan\alpha_{\mathrm{out}}$. However note, that due to adopted quasi-monochromatic approximation the magnitude of the wave vector is assumed to be the same for all the spectral components of the pulse ($k(\omega) \approx k_0$). Therefore, even in the paraxial case the actual transverse position of the beam will be different from the one, obtained using p_{sd2}, and the difference will increase with

the increasing propagation distance z_1 or deviation from the central frequency Ω.

Now let's further proceed with the optical scheme. The complex amplitude after the lens is obtained simply by multiplying the complex amplitude in front of the lens by the phase factor of the lens (Eq. (2.3.3))

$$A_3(t,x,y) = A_2(t,x,y)\exp\left(ik_0\frac{x^2+y^2}{2f}\right). \tag{3.2.29}$$

Thus, most of the pulsed Gaussian beam parameters are preserved, just those determining the angular spread of the pulsed beam undergo some changes, namely

$$p_{\mathrm{ad3}} = k'_{x_\mathrm{o}}\left(1-\frac{z_1}{f}\right), \quad p_{\mathrm{at3}} = -\frac{2k'_{x_\mathrm{o}}}{\bar{\tau}_1^2}\frac{z_{Rx}}{f}\left(1+\frac{f-z_1}{z_{Rx}}\left(\gamma_{x0}-\gamma_{t0}\right)\right). \tag{3.2.30}$$

As it can be readily seen, in case when $z_1 = f$ the pulsed Gaussian beam possesses no angular dispersion after the lens. This is in agreement with the geometrical optics, since it corresponds to the case when all the rays emerging from the focal point become parallel after the lens.

Finally, the complex amplitude at the back focal plane of the lens is obtained by calculating the diffraction of the pulsed Gaussian beam in free space

$$A_4(t,x,y) = \mathscr{F}^{-1}_{k_x,k_y}\left\{\mathscr{F}_{x,y}\left\{A_3(t,x,y)\right\}\exp\left[-i\left(k_0+\frac{\Omega}{c}-\frac{k_x^2+k_y^2}{2k_0}\right)f\right]\right\}. \tag{3.2.31}$$

The obtained characteristic pulsed Gaussian beam parameters at the back focal plane are given below

$$\tau_4 = \sqrt{\frac{\bar{\tau}_1^4+\left(\tau_0^2\gamma_{x0}+\rho_{x0}^2k'^2_{x_\mathrm{o}}\gamma_{t0}\right)^2}{\bar{\tau}_1^2+\tau_0^2\gamma_{x0}^2+\rho_{x0}^2k'^2_{x_\mathrm{o}}\gamma_{t0}^2}}, \qquad \bar{\tau}_4 = \bar{\tau}_1, \tag{3.2.32}$$

$$\bar{\rho}_{x4} = \rho_{x0}\frac{|f|}{z_{Rx}}\frac{\sqrt{\bar{\tau}_1^2+\tau_0^2\gamma_{x0}^2+\rho_{x0}^2k'^2_{x_\mathrm{o}}\gamma_{t0}^2}}{\tau_0}, \qquad \rho_{y4} = \rho_{y0}\frac{|f|}{z_{Ry}}\sqrt{1+\gamma_{y0}^2},$$

and the ones, determining the spatio-temporal couplings, are

$$p_{\mathrm{pt4}} = -k'_{x_\mathrm{o}}\frac{\rho_{x0}^2}{\bar{\rho}_{x4}^2}\frac{f}{z_{Rx}}\left(\gamma_{x0}-\gamma_{t0}\right), \qquad p_{\mathrm{sd4}} = f\frac{k'_{x_\mathrm{o}}}{k_0}, \tag{3.2.33}$$

$$p_{\mathrm{ad4}} = p_{\mathrm{ad3}}, \qquad p_{\mathrm{at4}} = p_{\mathrm{at3}}.$$

The obtained expressions of τ_4, $\bar{\rho}_{x4}$, ρ_{y4}, p_{pt4} reveal that, although the propagation distance z_1 before the lens was taken into account, the spatio-temporal profile at the back focal plane of the lens does not dependent on that distance. However, it can be seen from the expression of τ_4 that, in contrast to Ref. [73], the duration of the pulse at the back focal plane of the lens, actually, depends on the initial duration, indicating that the temporal profile at the focus depends on the initial pulse profile. Moreover, the on axis duration τ_4 depends on the phase-front curvature of the input beam, as indicated by the presence of γ_{x0}. Furthermore, the spatio-temporal profile of the pulsed Gaussian beam is tilted, since $p_{\mathrm{pt4}} \neq 0$. Interestingly, but the pulse-front tilt at the back focal plane of the lens can be adjusted by varying the phase-front curvature of the input beam, and in the special case, when $\gamma_{x0} = \gamma_{t0}$, the pulse tilt vanishes.

Additionally, from the expression of p_{sd4} we can see, that at the back focal plane of the lens the spatial dispersion (spatial chirp) does not depend on the propagation distance z_1 in front of the lens. This independence of the spatial dispersion can be readily explained by means of geometrical optics, since all the parallel rays intersect at the same point in the back focal plane of the lens, independently from their transverse position in front of the lens.

It should be reminded here, that the radius ρ_{y4} is independent on the temporal parameters of the pulse, and depends just on the initial radius ρ_{y0}, propagation distance z_1 and the focal length of the lens. Therefore, in the general case, the radii ρ_{x4} and ρ_{y4} are not equal, hence, at the back focal plane of the lens the beam is elliptical. However, since the initial radius ρ_{y0} is a free parameter, the radii ρ_{x4} and ρ_{y4} can always be matched in the experiment, simply by adjusting the initial radius ρ_{y0} with the help of the cylindrical lenses. For such purpose it might be useful to employ the cylindrical lens instead of the spherical one in the considered scheme as well (Fig. 3.2), so that the beam is focused only in the x direction by that lens. In such case, the beam radius ρ_{y4} will be defined just by the diffraction in free space. If this is the case, then the radius ρ_{y4} in Eq. (3.2.32)

should be replaced by

$$\rho_{y4} = \rho_{y0}\sqrt{\left(1 - \frac{z_1 + f}{z_{Ry}}\gamma_{y0}\right)^2 + \frac{(z_1 + f)^2}{z_{Ry}^2}}. \tag{3.2.34}$$

In order to get further insight into the obtained expressions of Eq. (3.2.32), let's consider a particular case when the beam is well-collimated at the input ($\gamma_{x0} = 0$) and when the overall duration $\bar{\tau}_1$ of the tilted pulsed Gaussian beam is much longer than the initial duration τ_0, i.e. when $\rho_{x0}|k'_{x_o}| \gg \tau_0$. This is actually the case under consideration in Ref. [73]. In such case, the $\bar{\tau}_1$ duration in Eq. (3.2.17) reduces to

$$\bar{\tau}_1 \approx \rho_{x0}|k'_{x_o}|, \tag{3.2.35}$$

and the characteristic parameters of the pulsed Gaussian beam at the back focal plane of the lens simplifies to

$$\begin{aligned}
\tau_{4'} &= \bar{\tau}_{4'} = \rho_{x0}|k'_{x_o}|, & \rho_{x4'} &= \bar{\rho}_{x4'} = 2\frac{|fk'_{x_o}|}{\tau_0 k_0}\sqrt{1+\gamma_{t0}^2}, \\
p_{\mathrm{pt}4'} &= \frac{1}{2}\frac{\tau_0^2 k_0}{fk'_{x_o}}\frac{\gamma_{t0}}{1+\gamma_{t0}^2}, & p_{\mathrm{sd}4'} &= p_{\mathrm{sd}4}, \\
p_{\mathrm{ad}4'} &= p_{\mathrm{ad}3}, & p_{\mathrm{at}4'} &= -\frac{1}{p_{\mathrm{sd}4}}\left(1 + \frac{z_1 - f}{z_{Rx}}\gamma_{t0}\right).
\end{aligned} \tag{3.2.36}$$

As it can bee seen from the obtained expressions, in case when $\gamma_{x0} = 0$ and $\rho_{x0}|k'_{x_o}| \gg \tau_0$, the on-axis duration $\tau_{4'}$ does not depend on the initial duration τ_0, but, in agreement with Refs. [73] and [78], is defined just by the initial radius ρ_{x0} and the angular dispersion k'_{x_o}. In addition, we have found that the radius $\bar{\rho}_{x4'}$ at the back focal plane of the lens does not depend on the initial radius ρ_{x0}, but is determined by the initial duration τ_0 and other parameters. However note, that in this case the pulsed Gaussian beam still possesses all the four spatio-temporal couplings.

It is important to note, that in this case the on-axis duration of the pulse $\tau_{4'}$ must always be much longer than the initial duration τ_0, despite the fact that $\tau_{4'}$ is independent of τ_0. This requirement comes from the assumption that

$\rho_{x0}|k'_{x_o}| \gg \tau_0$, which has been made in deriving the expression of $\tau_{4'}$.

Yet another special case of interest is when at the input the pulsed Gaussian beam is well-collimated $\gamma_{x0} = 0$ and, in addition, has no temporal chirp $\gamma_{t0} = 0$. In such case, the spatio-temporal profile at the back focal plane of the lens is not tilted, since $p_{\mathrm{pt4}} = 0$, and the on-axis duration is just equal to the overall pulse duration $\tau_4 = \bar{\tau}_1$, which has been acquired after the incidence on the angularly dispersive element. Therefore, in this case the τ_4 duration can be readily calculated from Eq. (3.2.17) knowing the initial diameter of the beam ρ_{x0}, the angular dispersion k'_{x_o} and the initial duration τ_0 of the pulse. Note that in this case the pulsed Gaussian beam possesses the spatial dispersion, angular dispersion and angle vs. time.

In order to illustrate the dynamics of the spatio-temporal profiles of the pulsed Gaussian beam propagated through the optical scheme, the intensity profiles at each particular plane of the optical scheme are depicted in Fig. 3.5. The four graphs correspond to the distinct spatio-temporal domains: (a) spatio-temporal, (b) temporal spectrum, (c) spatio-temporal spectrum and (d) spatial spectrum. Intensity profiles were depicted by a dashed line in some of the graphs, in order to avoid the possible misleadings in case when intensity profiles are overlapping. Here we consider the case of transform-limited and well-collimated pulsed Gaussian beam at the input, hence $\gamma_{t0} = 0$ and $\gamma_{x0} = 0$. The tilt of each of the profiles follow exactly the characteristic parameters in accordance with the previously obtained equations. Namely, after the angularly dispersive optical element (red line) the pulsed Gaussian beam has the positive angular dispersion (c) and becomes tilted (a), but has no spatial dispersion (b) nor angle vs. time (d). After propagation of some distance in free space (green line) it acquires the positive spatial dispersion (b), its on-axis duration is increased and the tilt is reduced (a), however the angular dispersion (c) as well as angle vs. time remain unchanged. After the lens (orange line) the angular dispersion becomes zero (c), since $z_1 = f$, but the pulsed beam acquires the negative angle vs. time (d), whereas the pulse

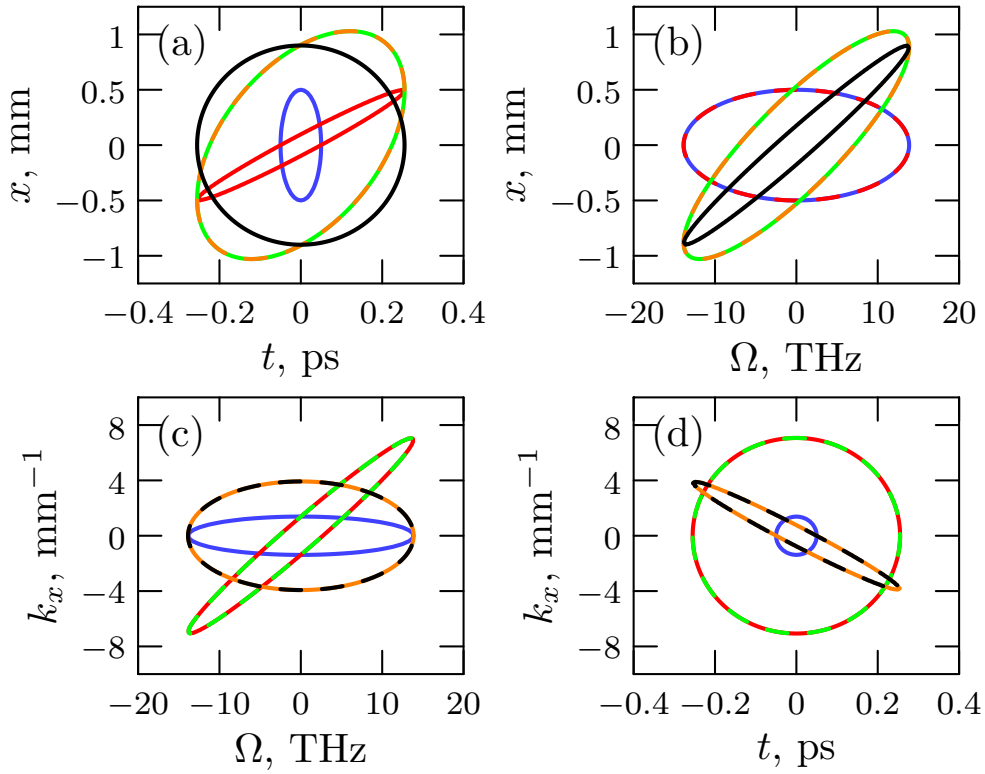

Figure 3.5: Variation of the iso-intensity profiles of the pulsed Gaussian beam in the different spatio-temporal domains. Note that the colors of the iso-intensity profiles correspond to the colors of the particular planes, at which they were observed (see Fig. 3.2). The initial parameters were as follows: $\tau_0 = 100$ fs (FWHM), $\rho_{x0} = 1$ mm (FWHM), $k'_{x_o} = 0.5$ ps/mm, $z_1 = f = 1$ m, $\lambda = 0.8$ μm, $\gamma_{t0} = \gamma_{x0} = 0$. All the iso-intensity contours are depicted at half-maximum intensity level ($\mathrm{m_I} = \ln 2$).

tilt (a) and spatial dispersion (b) remain unchanged. Finally, at the back focal plane of the lens (black line) the pulsed Gaussian beam becomes untilted (a), but inevitably possesses the spatial dispersion (b), which remains actually the same, since $p_{\mathrm{sd4}} = p_{\mathrm{sd2}}$ in case when $z_1 = f$.

In the introduction of this section, it was mentioned that the optical scheme considered in this section (Fig. 3.2) could be applied as a stretcher-compressor for picosecond pulses. In what follows, we present yet another possible application of this scheme. In the following, we present the numerical results disclosing the applicability of the considered optical scheme for optical parametric chirped-pulse amplifiers (OPCPAs) [3, 82]. As it is explained in the introduction of the next chapter, it is a desired feature in OPCPA to have the pump pulses with a flat-top temporal profile, since it enables to achieve a wider amplified bandwidth

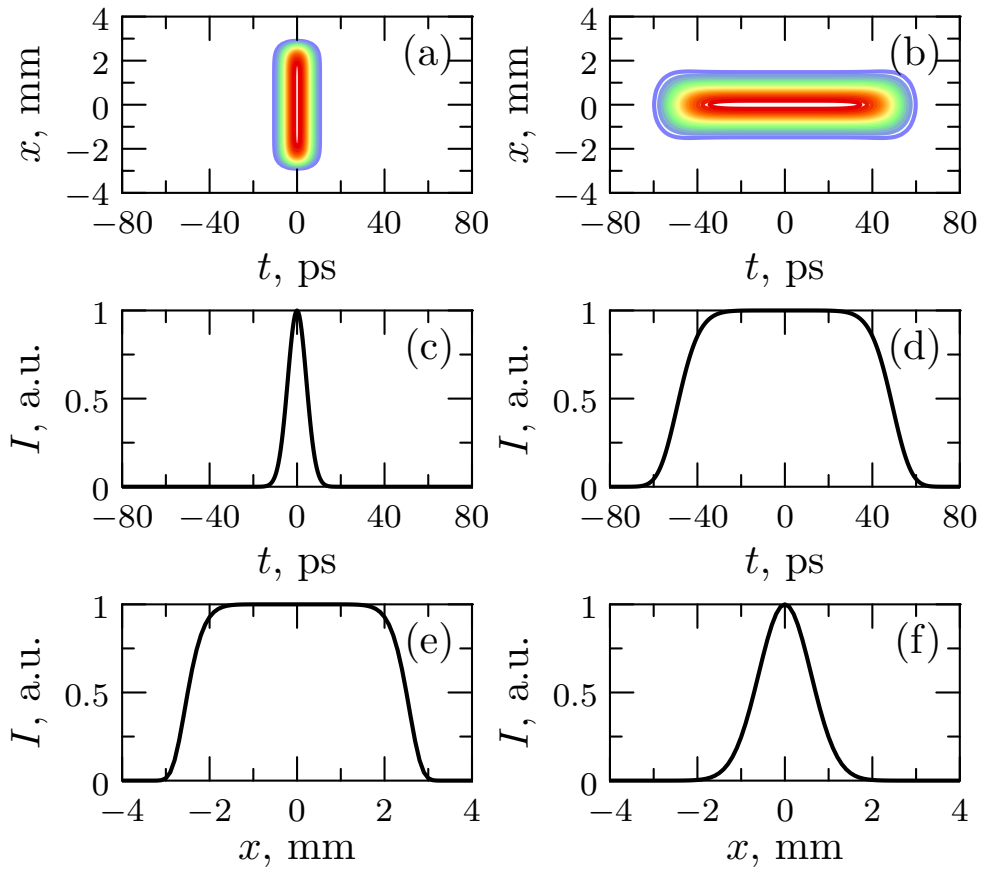

Figure 3.6: The spatio-temporal profiles of the pulsed beams at the input (a) and output (b) of the optical scheme (Fig. 3.2). The corresponding temporal profiles at $x = 0$ are depicted in (c) and (d), and the spatial profiles at $t = 0$ in (e) and (f), respectively. All graphs are normalized. The initial parameters were as follows: $I_{\text{peak0}} = 10$ GW/cm^2, $\tau_0 = 10$ ps (FWHM), $\rho_{x0} = 5$ mm (FWHM), $k'_{x_o} = 20$ ps/mm, $z_1 = f = 3$ m, $\lambda = 0.532$ μm, $\gamma_{t0} = \gamma_{x0} = 0$. Pulsed beam parameters at the back focal plane of the lens were as follows: $\bar{\tau}_4 = 99.5$ ps, $I_{\text{peak4}} = 3.5$ GW/cm^2, $\tau_4 = 97$ ps (FWHM), $\rho_{x4} = 1.4$ mm (FWHM).

of the signal pulse and a greater pump-to-signal conversion efficiency. As it is demonstrated below, this scheme could be used to transform flat-top spatial profile into flat-top temporal profile. Such reshaping of the pump pulse, in particular, its temporal profile, is readily available, since nearly flat-top pump beams are usually encountered in a high-energy setups. Nevertheless, to the best of our knowledge, such an idea has not yet been presented and here it is disclosed for the first time.

In contrast to the analytical study presented above, we have employed a pulsed super-Gaussian beam. Namely, at the input the temporal profile was still Gaussian, but the spatial profile was super-Gaussian of the 10th order. The spatio-temporal profile of the initial pulsed beam is depicted in Fig. 3.6a. At the input

the pulse was transform-limited and the beam was well-collimated. This guaranteed that the spatio-temporal profile will not be tilted at the back focal plane of the lens (Eq. (3.2.33)). It should be mentioned, that in the numerical simulations we do not make any assumptions about the paraxiality of the beams nor bandwidth of the pulses, as the propagation is modeled using Eq. (2.1.22) and the lens is taken into account using Eq. (2.3.1).

The spatio-temporal profile at the back focal plane of the lens is depicted in Fig. 3.6b. As it can be seen by comparison of Figs. 3.6c,d and Figs. 3.6e,f, the shape of the temporal profile has been inter-switched with the shape of the spatial profile. Thus, instead of the super-Gaussian spatial profile, at the back focal plane we have a pulsed Gaussian beam with a super-Gaussian temporal profile. The main requirement for such transformation of the profiles to occur, is that the overall duration $\bar{\tau}_1$ of the angularly dispersed pulsed beam to be considerably longer than the initial duration τ_0, that is, the condition $\rho_{x0}|k'_{x_o}| \gg \tau_0$ must be fulfilled.

Nevertheless, there are some drawbacks regarding the applicability of this scheme in OPCPA setups: (a) the length of the nonlinear crystal must be short enough, so that the pump pulse is nearly in its "horizontal position" throughout the crystal, (b) the angularly dispersive optical element may introduce some energy losses to the pump pulse, (c) the pump pulse has a spatial chirp, which may lead to undesired results during the parametric amplification. Yet, at least, the potential of this idea is worth the experimental verification.

3.3 Focusing of pulsed Gaussian beams possessing spatial dispersion

Spatial dispersion, namely, separation of frequency components in the transverse direction, is a permanent companion of the angular dispersion, since pulsed beams possessing the angular dispersion inevitably acquire the spatial dispersion simply when propagating [38]. Therefore, there are many possible ways to obtain spatially

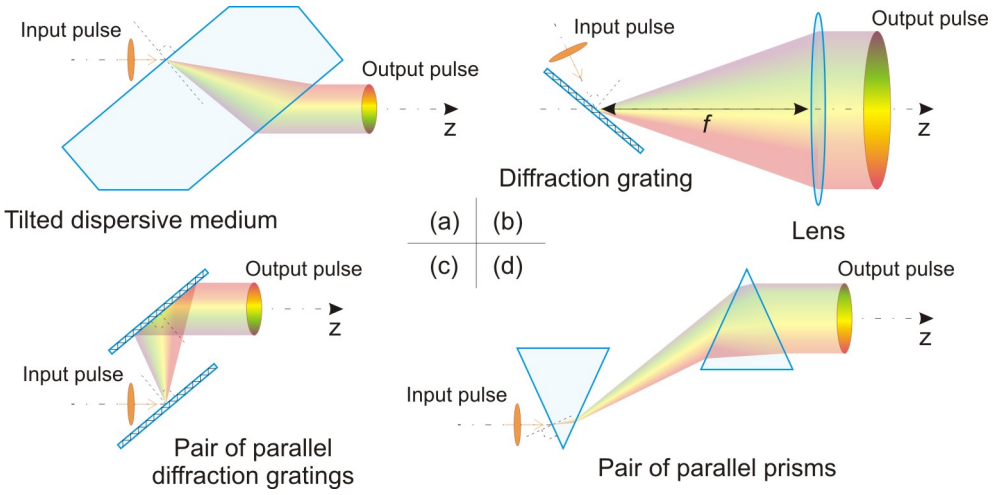

Figure 3.7: Some common ways, in which a spatially dispersed pulsed beam can be obtained.

dispersed pulsed beam, and just some of them are depicted in Fig. 3.7. Do not be confused with the spatial dispersion, which refers to the property of the medium, but has no relations to the spatial dispersion of the pulsed beams considered here.

In this section we are interested in the spatio-temporal dynamics of the pulsed Gaussian beam after being passed through spatially dispersive optical element and then focused by the lens. The optical scheme under consideration is depicted in Fig. 3.8. We should emphasize that in this case the pulsed Gaussian beam has no angular dispersion in front of the lens, just a spatial dispersion. Note that in the previous section, the angular dispersion gave rise to the spatial dispersion not only in the front of the lens, but also at the back focal plane of the lens as well. As it is apparent from Fig. 3.8 and examination by the geometrical optics, there will be no spatial dispersion at the back focal plane of the lens in this case. This scheme could be thought as the extension of the previous (Fig. 3.2), which in case when $z_1 = f$, becomes just as the one depicted in Fig. 3.7b, i.e. provides with the spatially dispersed pulsed beam, possessing no angular dispersion.

Usually, spatial dispersion is regarded as a spatio-temporal distortion of the pulsed beam, that should be avoided. However, in the recent years there was much attention dedicated for exploiting the spatial dispersion. In particular, focusing of spatially dispersed pulsed beams turned out to be advantageous in many fields

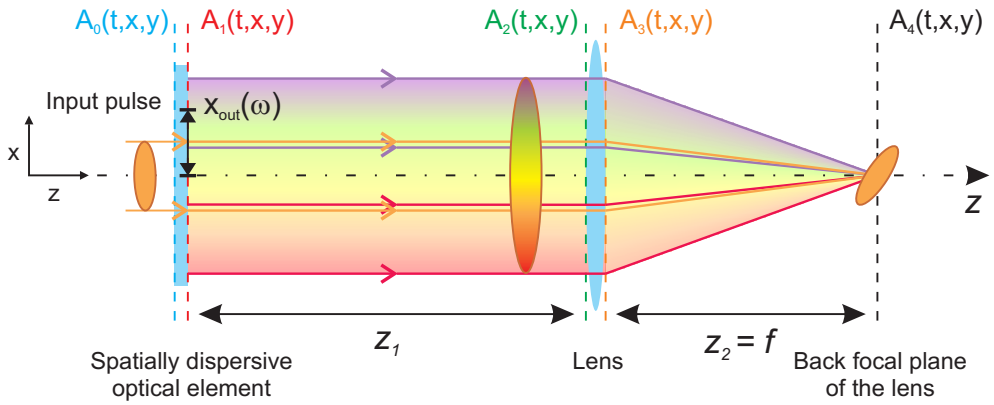

Figure 3.8: Schematic representation of the spatially dispersed pulsed beam being focused by a lens. It depicts a particular situation, when at the input the pulsed beam is transform-limited, thus at the back focal plane of the lens it is transform-limited as well. At the back focal plane of the lens the pulsed beam possesses the pulse-front tilt and angular dispersion, but has no spatial dispersion (see text for more details). z_1 denotes the distance from the spatially dispersive optical element to the lens, f - focal length of the lens, $x_{\mathrm{out}}(\omega)$ - the frequency dependent output position of the beam.

of laser-matter interaction. The main feature, which has drawn the attention, is the enhanced localization of the pulse intensity at the focus. When a pulsed beam possessing spatial dispersion is focused by a lens or curved mirror, its duration becomes transform-limited just at the focus, i.e. at the moment when all the frequency components are fully overlapped. Thus the axial intensity is strongly localized.

Recent works in nonlinear microscopy [36, 37], micromachining [83], waveguide writing [34], multiphoton microfabrication [84] and filamentation [32] has taken an advantage of this special feature. In particular, the strong localization that results from simultaneous space and time focusing is useful for multi-photon microscopy, since it improves the axial resolution for wide-field imaging. In micromachining, it strongly suppresses the nonlinear effects in a medium along the way to the focus, thus allowing to operate on the back side of a transparent medium. However, it should be noted, that at the focus the pulse front is tilted, and this may have additional effect in laser-matter interaction [33, 85].

Furthermore, the spatial shaping of the spatially dispersed pulsed beams empowers to actively control their temporal properties during propagation, and is a promising tool for many applications. In this technique, a lens or curved mirror

is placed one focal length away from a grating or prism, mapping frequency to position, that is, introducing spatial dispersion at the back focal plane of the lens (Fig. 3.7b). By deliberated separation of the different frequency components spatially, the pulse shaping in the frequency domain becomes possible [86, 87, 88, 89]. Naturally, the accuracy of pulse shaping depends on the degree of spatial dispersion at the focal plane.

Other applications of spatial dispersion include the suppression of longitudinal mode competition in the active medium of the laser, as was referenced in the introduction of the previous section.

The analytical study presented in the following is very similar to the one of the previous section, since most of the initial conditions and assumptions are analogous and can be simply adopted to this scheme. Just as in the previous section, at the input of the optical scheme we consider pulsed Gaussian beam possessing a linear temporal chirp (Eq. (3.2.1)). At first, the pulse is incident on the spatially dispersive element, which again is treated as a thin optical element. As it is depicted in Fig. 3.8, the spatially dispersive element gives rise to the lateral shift of an incident beam with an output position x_{out}, which depends on the temporal frequency ω of the beam. Note that, after the spatially dispersive element, the output position of the beam with the central frequency ω_0 is taken as a reference, thus $x_{\text{out}}(\omega_0) = 0$. For simplicity we assume, that pulsed Gaussian beam is spatially dispersed just in the x direction.

In general, the function of the spatial dispersion $x_{\text{out}}(\omega)$ can be of the arbitrary form. However, in the following analysis we shall assume that the spatial dispersion is linear

$$x_{\text{out}}(\omega) = \left.\frac{\mathrm{d}x_{\text{out}}}{\mathrm{d}\omega}\right|_{\omega_0} (\omega - \omega_0) = x'_{\text{o}}\Omega. \tag{3.3.1}$$

Typically the spatial dispersion, imposed by the spatially dispersive element, can be kept linear only in the narrow region of the spectrum. Therefore, be aware of the restriction to the pulse bandwidth, that is introduced by this assumption.

With the assumptions mentioned above, the complex amplitude after the spatially dispersive element is obtained by performing the partial Fourier transformation of Eq. (3.2.1) into the spatio-spectral domain (Ω, k_x, y) and multiplying by the frequency-dependent linear spatial phase, and finally transforming back to the space-time domain

$$A_1(t,x,y) = \mathscr{F}^{-1}_{\Omega,k_x}\left\{\mathscr{F}_{t,x}\left\{A_0(t,x,y)\right\}\cdot\exp\left(ix'_{\mathrm{o}}\Omega k_x\right)\right\}. \tag{3.3.2}$$

The spatio-temporal intensity profile takes the form as given in Eq. (3.1.1). Therefore, it will not be explicitly rewritten here, just the essential parameters of the pulsed beam are provided below

$$\begin{aligned}
\tau_1 &= \tau_0\frac{\rho_{x0}}{\bar{\rho}_{x1}}\sqrt{1+\frac{8x'^2_{\mathrm{o}}}{\tau_0^2\rho_{x0}^2}\left(1-\gamma_{t0}\gamma_{x0}\right)+\frac{16x'^4_{\mathrm{o}}}{\tau_0^4\rho_{x0}^4}\left(1+\gamma_{t0}^2\right)\left(1+\gamma_{x0}^2\right)},\\
\bar{\tau}_1 &= \tau_0\sqrt{1+\frac{4x'^2_{\mathrm{o}}}{\tau_0^2\rho_{x0}^2}\left(1+\gamma_{x0}^2\right)},\\
\bar{\rho}_{x1} &= \rho_{x0}\sqrt{1+\frac{4x'^2_{\mathrm{o}}}{\tau_0^2\rho_{x0}^2}\left(1+\gamma_{t0}^2\right)},\\
\rho_{y1} &= \rho_{y0}.
\end{aligned} \tag{3.3.3}$$

As it can be seen from the obtained expression of the on-axis pulse duration τ_1, its dependence on the spatial dispersion parameter x'_{o} is quite complicated. In general the τ_1 duration may become longer as well as shorter after the spatially dispersive optical element. It essentially depends on the sign and value of the γ_{t0} and γ_{x0}. Whereas the overall pulse duration $\bar{\tau}_1$ and overall beam radius $\bar{\rho}_{x1}$ *always* increase with the increased spatial dispersion x'_{o}. Obviously, the overall beam radius $\bar{\rho}_1$ also depends on the temporal chirp parameter γ_{t0}, since the greater value of γ_{t0} corresponds to the wider spectrum of the pulse. However, the similar dependence of the overall pulse duration $\bar{\tau}_1$ on the phase-front curvature γ_{x0} is not so obvious, and actually indicates, that the pulse tilt of the spatially dispersed pulsed Gaussian beam depends on the phase-front curvature of the beam. This will become apparent in the following.

Parameters, characterizing the spatio-temporal couplings acquired by the pulsed Gaussian beam after the spatially dispersive optical element, were obtained in accordance with Eq. (3.1.10)

$$p_{\mathrm{pt1}} = \frac{2x'_{\mathrm{o}}}{\bar{\rho}_{x1}^2}\left(\gamma_{t0}+\gamma_{x0}\right), \qquad p_{\mathrm{sd1}} = x'_{\mathrm{o}}, \tag{3.3.4}$$
$$p_{\mathrm{ad1}} = 0, \qquad p_{\mathrm{at1}} = -\frac{4x'_{\mathrm{o}}}{\rho_{x0}^2\bar{\tau}_1^2}\left(1+\gamma_{x0}^2\right).$$

The obtained expression of the pulse tilt p_{pt1} evidences the fact, that in the absence of the angular dispersion the pulse tilt may result from the spatial dispersion and simultaneous presence of either temporal chirp γ_{t0} or phase-front curvature γ_{x0} of the beam. Moreover, the spatial dispersion contributes to the temporal chirp of the pulse, as it can be seen from the obtained expression of the on-axis temporal chirp

$$\gamma_{t1} = \frac{\rho_{x0}^2}{\bar{\rho}_{x1}^2}\left(\gamma_{t0} - \frac{4x'^2_{\mathrm{o}}}{\tau_0^2\rho_{x0}^2}\gamma_{x0}\left(1+\gamma_{t0}^2\right)\right). \tag{3.3.5}$$

As we can see, in case when the initial pulsed Gaussian beam has a diverging phase front ($\gamma_{x0} < 0$), the spatial dispersion gives rise to the positive temporal chirp of the pulse, and vice versa. Note that the sign of the spatial dispersion x'_{o} does not affect the induced temporal chirp.

Let's step further in the optical scheme. The implicit expression of the complex amplitude at the plane in front of the lens is given by Eq. (3.2.22), and the obtained characteristic parameters of the pulsed Gaussian beam are

$$\tau_2 = \tau_0\frac{\rho_{x0}}{\bar{\rho}_{x2}}\left[\left(1-\frac{z_1}{z_{Rx}}\gamma_{x0}\right)^2 + \frac{z_1^2}{z_{Rx}^2} + \gamma_{t0}\frac{z_1}{z_{Rx}}\frac{8x'^2_{\mathrm{o}}}{\tau_0^2\rho_{x0}^2}\left(1+\gamma_{x0}^2\right)\right.$$
$$\left. + \frac{8x'^2_{\mathrm{o}}}{\tau_0^2\rho_{x0}^2}\left(1-\gamma_{t0}\gamma_{x0}\right) + \frac{16x'^4_{\mathrm{o}}}{\tau_0^4\rho_{x0}^4}\left(1+\gamma_{t0}^2\right)\left(1+\gamma_{x0}^2\right)\right]^{\frac{1}{2}},$$
$$\bar{\tau}_2 = \bar{\tau}_1, \tag{3.3.6}$$
$$\bar{\rho}_{x2} = \rho_{x0}\sqrt{\left(1-\frac{z_1}{z_{Rx}}\gamma_{x0}\right)^2 + \frac{z_1^2}{z_{Rx}^2} + \frac{4x'^2_{\mathrm{o}}}{\tau_0^2\rho_{x0}^2}\left(1+\gamma_{t0}^2\right)},$$
$$\rho_{y2} = \rho_{y0}\sqrt{\left(1-\frac{z_1}{z_{Ry}}\gamma_{y0}\right)^2 + \frac{z_1^2}{z_{Ry}^2}},$$

and the parameters characterizing the spatio-temporal couplings are

$$p_{\mathrm{pt2}} = \frac{2x'_{\mathrm{o}}}{\bar{\rho}_{x2}^2}\left(\gamma_{t0} + \gamma_{x0} - \frac{z_1}{z_{Rx}}\left(1+\gamma_{x0}^2\right)\right), \qquad p_{\mathrm{sd2}} = p_{\mathrm{sd1}}, \tag{3.3.7}$$

$$p_{\mathrm{ad2}} = p_{\mathrm{ad1}}, \qquad p_{\mathrm{at2}} = p_{\mathrm{at1}}.$$

As it can bee seen, the on-axis pulse duration τ_2 has even more complicated expression now, but we can obviously see that it depends on the propagation distance z_1. This can be explained by the fact that the phase-front curvature of the beam varies during the propagation, and in the presence of the spatial dispersion it affects the duration of the pulse. Nevertheless, the overall pulse duration $\bar{\tau}_2$ does not change during the propagation. Whereas, the overall beam diameter $\bar{\rho}_{x2}$ depends on the propagation distance in the usual way, despite the additional term due to spatial dispersion.

As it is apparent from the expression of p_{pt2}, similarly as in case of propagation of the angularly dispersed pulsed Gaussian beam, the sign of the pulse tilt changes at the particular distance

$$z_{1_{p_{\mathrm{pt2}}=0}} = z_{Rx}\frac{\gamma_{t0}+\gamma_{x0}}{1+\gamma_{x0}^2}. \tag{3.3.8}$$

It witnesses the fact that both the temporal chirp and the phase-front curvature affect the pulse tilt, and that in some cases their contribution to the pulse tilt may be canceled by each other. To illustrate this, let's consider the case when at the input the pulsed Gaussian beam is well-collimated ($\gamma_{x0} = 0$) and has a positive temporal chirp ($\gamma_{t0} > 0$). In such case, after the spatially dispersive optical element the pulsed Gaussian beam acquires the positive pulse tilt ($p_{\mathrm{pt1}} > 0$). However, during propagation in free space the phase-front of the beam becomes divergent and gives rise to the negative pulse tilt. Therefore, after some propagation distance the pulse tilt p_{pt1} is canceled.

Note that other spatio-temporal couplings remain unchanged during the propagation. Nevertheless, the lens introduces the angular dispersion and changes the

angle vs. time as given below

$$p_{\mathrm{ad}3} = -k_0 \frac{x'_{\mathrm{o}}}{f}, \qquad p_{\mathrm{at}3} = -\frac{2x'_{\mathrm{o}}}{\bar{\tau}_1^2}\frac{k_0}{f}\left(\gamma_{t0} + \gamma_{x0} - \frac{z_1 - f}{z_{Rx}}\left(1 + \gamma_{x0}^2\right)\right). \tag{3.3.9}$$

The acquired angular dispersion can be readily explained by means of geometrical optics, since it corresponds to the case when all the rays parallel to the z axis are deflected to the focus of the lens. However, it should be noted that the angular dispersion must obey the paraxial approximation, that is, the condition $\tan\alpha = \dfrac{x'_{\mathrm{o}}}{f} \approx \sin\alpha$ must be fulfilled.

Finally, at the back focal plane of the lens the parameters of the pulsed Gaussian beam become

$$\begin{aligned} \tau_4 &= \tau_0, & \bar{\tau}_4 &= \bar{\tau}_1, \\ \bar{\rho}_{x4} &= \rho_{x0}\frac{|f|}{z_{Rx}}\sqrt{1+\gamma_{x0}^2}, & \rho_{y4} &= \rho_{y0}\frac{|f|}{z_{Ry}}\sqrt{1+\gamma_{y0}^2}, \end{aligned} \tag{3.3.10}$$

and the ones, determining the spatio-temporal couplings, are

$$\begin{aligned} p_{\mathrm{pt}4} &= p_{\mathrm{ad}3}, & p_{\mathrm{sd}4} &= 0, \\ p_{\mathrm{ad}4} &= p_{\mathrm{ad}3}, & p_{\mathrm{at}4} &= p_{\mathrm{at}3}. \end{aligned} \tag{3.3.11}$$

As we can see, the obtained expressions are very simple and has no dependence on propagation distance z_1, except for $p_{\mathrm{at}4}$. In addition, the pulse duration τ_4 is simply equal to the initial pulse duration τ_0, and the pulse is free from spatial dispersion ($p_{\mathrm{sd}4} = 0$), but is tilted due to the angular dispersion, acquired after the lens ($p_{\mathrm{pt}4} = p_{\mathrm{ad}3}$).

3.4 Space-time focusing of temporally chirped pulses

In the previous two sections we have considered the spatio-temporal transformations of pulsed Gaussian beams possessing common STCs, yet without particular purpose having in mind. This section is aimed to give a clue of how to employ the STCs in order to simultaneously compress the temporally chirped pulsed light

beams in space and time. Such compression could be of particular interest for high-peak-power laser systems, where typically a temporal compression of the amplified chirped pulse is accomplished using a pair of gratings or prisms [90, 91]. These traditional pulse compressors suffer from optical damaging of the components due to high pulse intensity when the pulse duration gets shortened [92]. The approach of the chirped-pulse compression presented below, could be a key solution, since spatio-temporal compression of the pulsed beam is achieved during its propagation in free space, and without being in contact with optical elements at the compression stage. Thus, resolving the issue of optical damaging. Yet another potential application of the spatio-temporal compression could be seen in the laser-matter interaction experiments, where enhanced localization of the pulse intensity is required (see for example Ref. [32]).

The basic idea of space-time focusing is simple: we have to assure that all the spectral components of the temporally chirped pulse arrive at the same point in space and at the same time. In order to achieve this in vacuum, different spectral components have to take a different optical path towards the focus. This prerequisite comes from two fundamental conditions: first, the speed, at which the spectral components travel in vacuum, is the same for all the components, and second, at the input the spectral components are delayed with respect to each other, since the pulse is temporally chirped at the input. To take a different optical path in vacuum actually means to propagate at different angle with respect to common propagation axis, usually denoted as z axis. As we can imagine different spectral components, propagating at different angles and arriving at the same point in space, have to come from different space locations. And these are the essential elements for the solution of this problem. In particular, in order to focus in time at the desired distance the spectral components of the pulsed beam must obey the proper angular dispersion, and in order to focus in space at the same distance, the spectral components must obey the proper spatial chirp at the input.

The conceptual scheme is depicted in Fig. 3.9. Actually, there are two of

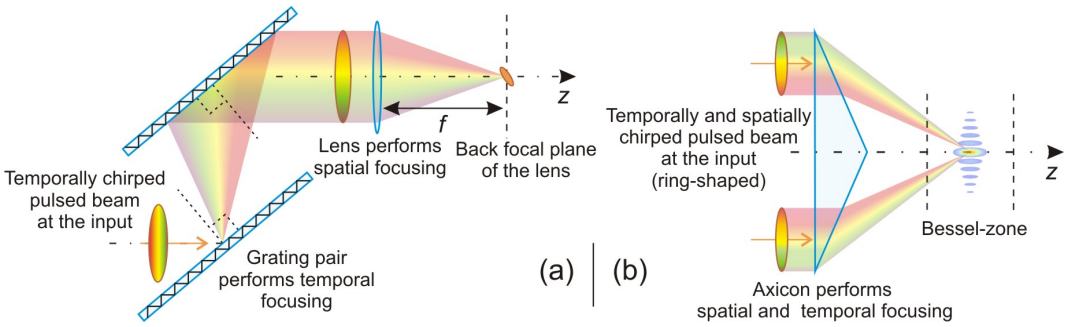

Figure 3.9: The conceptional optical schemes for space-time focusing of temporally chirped pulses: (a) for space-time focusing of temporally chirped pulsed Gaussian-like beams, (b) for space-time focusing of temporally chirped pulsed Bessel-like beams.

them: one for pulsed Gaussian-shaped beams (Fig. 3.9a), and the other for pulsed Bessel–Gaussian beams (Fig. 3.9b). The first scheme might seem very similar to the one considered in [71], and the second to [93], however, note that in those setups the pulse must be transform-limited at the input, in order to obtain a transform-limited pulse at the focus. Therefore, it is actually not a true space-time focusing and this is the essential difference, since we consider the temporally chirped pulses at the input.

Actually, the first scheme has been originally proposed on a slightly different purpose in [94]. It is essential to realize, that in this scheme the initial temporal chirp of the pulse is compensated by the pair of the gratings and that all of its spectral components arrive at the same time in front of the lens. This is a prerequisite of this scheme, since otherwise, the transform-limited duration would not be obtained at the focus (see the previous section). Therefore, the pulse must possess a specific temporal chirp at the input, which can be retrieved from the analysis of the grating pair by means of geometrical optics. The evolution of the pulsed beam after the grating pair is actually described in the previous section, thus for further details the reader is referred to that section.

The second scheme (Fig. 3.9b) has been presented in [C2]. The fundamental difference from the previous scheme, is that at the output we have a pulsed Bessel–Gaussian beam [95]. The main advantage of such a beam over the ordinary Gaussian beam is a prolonged region in space, where the beam diameter is nearly

constant. In case of Bessel–Gaussian beams this particular region in space is called a Bessel-zone. It is important to realize, that the diameter of the pulsed Bessel–Gaussian beam is defined just by intersection angle and the central wavelength of the pulse. Thus, we actually do not need any focusing optics in order to obtain a small beam diameter at the Bessel-zone. However, there is a price, namely, the peak intensity of the pulsed Bessel–Gaussian beam is much lower in comparison to the peak intensity of the pulsed Gaussian beam when the energies, durations (FWHM) and diameters (FWHM) are the same. This is due to the fact that most of the energy of the pulsed Bessel–Gaussian beam is located in its exterior. On the other hand, it may turnout to be advantageous, since it leads to another peculiar feature of the Bessel-Gaussian beams, that is, the ability to restore its shape after the central part of the beam is being blocked by the opaque disk.

The actual layout of this scheme is depicted in Fig. 3.10. As it can bee seen, there are actually two axicons employed. The first axicon just transforms a Gaussian beam into a ring-shaped beam, and the second "focuses" the ring-shaped beam, which after the distance z_2 interferes with itself and forms the Bessel-zone. The length of the Bessel-zone is defined by the diameter of the ring-shaped beam and the intersection angle α. The temporal compression results from the angular dispersion imposed by the refraction at the interface of the axicons. Just as in the previous scheme (Fig. 3.9a), in order to obtain a transform-limited pulse at the center of the Bessel-zone, it must possess a suitable temporal chirp at the input, which, for the particular set of the axicons, can be retrieved by means of geometrical optics. Note that in this scheme the temporal compression occurs simultaneously with the compression in space.

However, in order to achieve a considerable compression in time, a highly dispersive material is needed and the base angle of the axicon should be as large as possible. Therefore, for the second axicon ax_2 we have chosen a SF11 glass. The base angle was equal to $\sigma_2 = 20$ deg, since larger angles is hard to produce due to technological problems. Nevertheless, for the first axicon ax_1 we have chosen

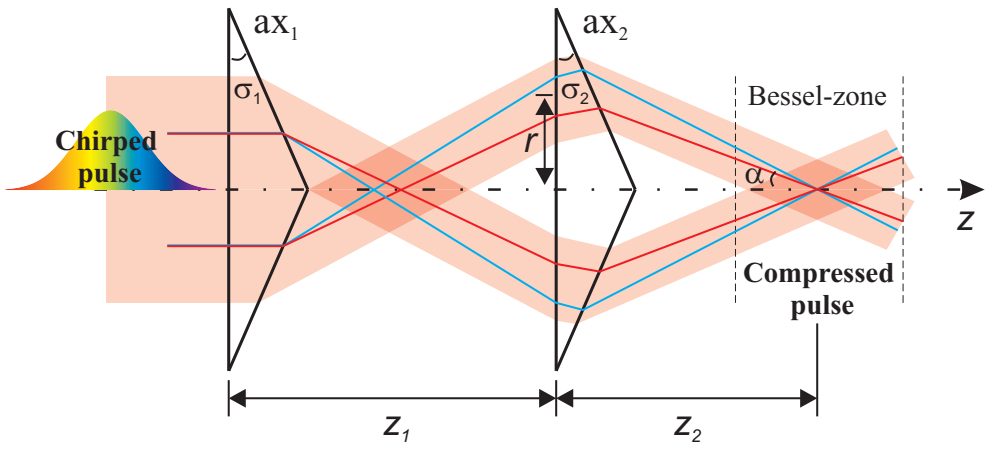

Figure 3.10: Schematic representation of space-time focusing using two axicons. ax_1 and ax_2 denote the axicons with the base angles σ_1 and σ_2, respectively. Red and blue lines indicate the paths of different spectral components of the pulse. α denotes the intersection angle, r denotes the radius of the ring-shaped beam, z_1 - the distance between the axicons, and z_2 - the distance form the second axicon to the center of the Bessel-zone (space-time focus).

BK7 glass, since the purpose of this axicon is just to reshape the Gaussian beam into a ring beam. The base angle of this axicon was equal to $\sigma_1 = 20$ deg as well, since a smaller base angle would lead to a larger intersection angle α, and thus, to the reduced length of the Bessel-zone.

If materials and base angles of the axicons are set, the temporal compression factor depends on the distance z_1 between the axicons, namely, the longer is this distance the longer chirped pulse can be compressed. However, this distance is limited by the diameter of the ax_2, as increasing distance z_1 the radius r of the ring-shaped beam also increases. If considering the axicons of 50 mm in diameter, the estimated duration of the chirped Gaussian pulse at the input is 195 fs for $z_1 = 110$ mm. This duration was obtained by calculating the group delay dispersion of this scheme using the geometrical optics, and assuming the pulse bandwidth, centered at 800 nm and corresponding to 10 fs transform limited Gaussian pulse.

It should be noted, that in this setup we did not take a special care about the spatial chirp at the entrance plane of the second axicon. In the ideal case, the spatial chirp must be of some particular shape in order for all the spectral components of the pulse to arrive at the same point in space. Otherwise, the

residual spatial chirp may result in the reduction of the achievable minimal pulse duration at the center of the Bessel-zone.

The contribution of the residual spatial chirp to the pulse duration at the center of the Bessel-zone was verified numerically. A transform-limited pulsed Gaussian beam of 10 fs duration (FWHM) and 1 mm diameter (FWHM) was transformed into pulsed Bessel–Gaussian beam by applying the angular and spatial dispersions, retrieved from the analysis of this optical scheme using geometrical optics. The duration and diameter of the obtained pulsed Bessel–Gaussian beam were 10.6 fs (FWHM) and 3.5 μm (FWHM), respectively. Thus, the contribution of the spatial chirp to the pulse duration at the Bessel-zone was not significant. Nevertheless, note that for smaller diameters of the initial Gaussian beam or for wider pulse bandwidths the role of the spatial chirp may become detrimental. The peak intensity was 5.4 PW/cm^2, assuming the 1 mJ energy of the pulsed Bessel–Gaussian beam. The distance between the axicons was $z_1 = 110$ mm, whereas the distance from the second axicon to the center of the Bessel zone was $z_2 = 242$ mm. For the central wavelength the radius of the ring-shaped beam at the entrance plane of the second axicon was $r = 19.8$ mm, and the intersection angle was $\alpha = 4.76$ deg.

Finally noted, that such compression in space and time could be achieved not only in free space, but in the desired material as well.

3.5 Conclusions

Due to the presence of the angular dispersion the pulsed Gaussian beam acquires a negative temporal chirp when propagating in free space. Therefore, if the initial pulsed Gaussian beam has a positive temporal chirp, it undergoes a temporal compression. However, a transform-limited duration cannot be achieved due to simultaneous lateral walk-off of the spectral components, namely, due to the acquired spatial chirp.

The spatial chirp accompanied by the phase-front curvature of the beam may give rise to the temporal chirp and pulse-front tilt. Remarkably, under certain

initial conditions the angularly dispersed pulsed Gaussian beam may undergo a temporal compression during propagation in free space even in the case when its initial temporal chirp is negative, and the pulse-front tilt, caused by the angular dispersion, may be counterweighted at the particular propagation distance by the pulse tilt, resulting from the spatial chirp. At this propagation distance the pulsed Gaussian beam is not tilted, even though it has the same angular dispersion.

In the general case, after some intermediate variation, the pulse-front tilt of the angularly or spatially dispersed pulsed Gaussian beam gradually disappears with the increasing propagation distance. However, the overall duration of the angularly or spatially dispersed pulsed Gaussian beam does not change during propagation in free space, despite the fact that its spatio-temporal profile is consistently changing.

When the angularly or spatially dispersed pulsed Gaussian beam is focused by the lens, its spatio-temporal profile at the back focal plane of the lens does not dependent on the propagation distance before the lens. However, the spatio-temporal profile is tilted. In case of angularly dispersed pulsed Gaussian beam, the pulse-front tilt at the back focal plane of the lens depends on the initial parameters of the pulsed Gaussian beam and its sign is determined by the phase-front curvature and temporal chirp at the input. Whereas in case of spatially dispersed pulsed Gaussian beam, the pulse-front tilt at the back focal plane of the lens does not depend on the initial parameters of the pulsed Gaussian beam, and is determined by the acquired angular dispersion only.

In the particular case, when initial pulsed Gaussian beam is well-collimated and its overall duration after the angularly dispersive optical element is much longer than the initial duration, the pulse duration at the back focal plane of the lens does not depend on the initial duration, and the beam diameter does not depend on the initial diameter. It has been demonstrated that in such case, the considered optical scheme could be used to inter-switch the temporal profile of the pulsed beam with its spatial profile.

Chapter 4

Signal pulse reshaping during the parametric amplification

Material related to this chapter was published in [A1, A2]

It is well-known that in optical parametric chirped-pulse amplifier (OPCPA), the spectrum of the signal pulse can be substantially reshaped. The two complementary mechanisms that affect the signal pulse spectrum in OPCPA are: wavelength-dependent phase mismatch and inhomogeneous amplification of the chirped pulse, due to non-uniform profile of the pump pulse. Since the spectral components are temporally delayed in the chirped pulse, different parts of the signal spectrum could be amplified simply by changing the delay between chirped signal and a short pump pulse [96]. Such situation is generally not of practical importance for OPCPA, however, one should have it in mind if difference between the group velocities of signal and pump can not be neglected. In such case, the group-velocity mismatch in combination with the depletion of the pump, might result in ambiguous reshaping of the signal spectrum [97, 98].

In order to reduce the spectral narrowing occurring when a chirped signal pulse is being amplified by a Gaussian pump pulse, in most common situations of OPCPA, the employed signal pulse is considerably shorter than the pump pulse [99]. Note that such spectrum narrowing occurs even in the case of perfect phase matching for all signal wavelengths. Obviously, the spectral narrowing

could be avoided if the duration of the signal pulse was much shorter than the duration of the pump, or if the temporal profile of the pump pulse was flat-top. However, formation of the flat-top pump pulse is demanding, and in the former case, a trade-off between the amplified bandwidth and pump-to-signal conversion efficiency arises [100, 101, 102, 103]. Nevertheless, in the saturation regime, the Gaussian spectrum of the signal may be reshaped into super-Gaussian and may become broadened significantly. Furthermore, it may possess a dip around the central wavelength due to back-conversion [100].

As it was explained above, when phase-matched bandwidth is much broader than the spectrum width of the chirped signal pulse, the amplified bandwidth essentially depends on pump-to-signal duration ratio. However, if phase-matched bandwidth is not that broad, then phase matching also takes a part in reshaping of the signal pulse. In particular, only the spectral components of the signal pulse that are phase matched with the pump, will be preferentially amplified. Consequently, just the part of pump pulse, which is over the phase-matched components of the chirped signal pulse, will be depleted. And here comes an idea, presented in [104], that wavelength-dependent phase mismatch in combination with arbitrarily-shaped temporal profile of the pump pulse could be used to achieve a uniform spectral gain for the chirped signal pulse. In particular, it has been shown that ideal combinations of wavelength-dependent phase mismatch, pump intensity, seed intensity, and their temporal profiles can significantly boost amplifier bandwidth as well as conversion efficiency, allowing in some amplifiers a severalfold increase of the obtainable peak power.

Spectral shaping by means of phase matching might also be employed in order to extend the total bandwidth of the parametric amplifier [105, 106]. The basic idea in this case is to phase match and amplify different parts of the signal spectrum in the subsequent amplification stages, and in such a way to achieve much broader signal spectrum, in comparison to a single-stage case.

As referenced above, there are many works devoted to the analysis and op-

timization of the OPCPA (see also [21, 107, 108]). So far, almost all of them assume a 1D model of plane monochromatic waves and focus their attention to the achievable signal bandwidth or conversion efficiency. Only very recently an extensive 3D study, taking into account the transverse dimensions, has revealed a new aspects of signal pulse reshaping during the amplification in noncollinear OPCPA [20]. It has been shown that, in noncollinear parametric amplifier, when pulse fronts of pump and signal are not matched, the signal pulse becomes tilted and aside from angular dispersion has a spatial chirp. The main results of this study are presented in the following sections.

4.1 Manifestation of spatial chirp

As it was mentioned above, the temporal spectrum of the signal pulse may be reshaped even in the case of extremely broad bandwidth of OPCPA. Yet, in case of noncollinear interaction not only the spectrum of the signal pulse, but the whole spatio-temporal distribution might be reshaped. Typically, the extremely broad amplification bandwidth is provided by the noncollinear optical parametric amplifiers (NOPAs) operated at the so-called "magic" phase-matching angle [13, 14]. However, this noncollinear configuration has a drawback, arising as a consequence of pulse-front mismatch of signal and pump. It has been shown [15, 16], that due to pulse-front mismatching, signal pulse experiences a reshaping, which leads to the reduced conversion efficiency and spatio-temporal distortions of the signal pulse, such as pulse-front tilt, angular dispersion and spatial chirp. These distortions limit the achievable minimum pulse duration and are more pronounced in case of the femtosecond pulse amplification, when the physical length of the pulses, in most of the cases, is much less than the diameter of the beams.

The angular dispersion induced in noncollinear parametric amplifier has been studied in several works [5, 18, 19]. It was shown, that this type of distortion can be eliminated or significantly reduced by pulse-front matching. In those works, the presence of the angular dispersion was considered as a consequence of the

pulse-front tilting. However, as it was pointed out by Akturk et al. [39], the pulse-front tilt and angular dispersion are not equivalent. It has been shown, that the pulse-front tilt can be also caused by the simultaneous presence of the spatial and temporal chirp. Therefore, solely from the pulse-front tilt, one *cannot* conclude that the pulse has angular dispersion.

A typical femtosecond NOPA has been studied in [17], and the measurements taken by imaging spectrometer have revealed, that at the output of NOPA the signal pulse has a slight spatial chirp. This result has spurred the following research on the spatio-temporal distortions arising in noncollinear OPCPAs due to pulse-front mismatch. In what follows, the performed investigation reveals that signal pulse tilting induced by the pump pulse, causes simultaneous appearance of angular dispersion and spatial chirp. However, in case of large temporal chirp of the signal pulse, the contribution of the angular dispersion to the pulse-front tilt becomes negligible. In parallel, we discuss the case when pump and signal fronts are perfectly matched.

This study is organized as follows. In section 4.2 we give an explanation for the origin of spatial chirp and present results of analytical treatment of the noncollinear parametric amplification. The expressions relating the magnitudes of the acquired spatial chirp and angular dispersion to the temporal chirp of the signal pulse are derived. In section 4.3 we present results of (3D+1) numerical experiments for the case of femtosecond noncollinear OPCPA. And in section 4.4 experimental verification of the theoretical findings is presented.

4.2 Spatial chirp and angular dispersion in noncollinear OPCPA

The origin of the signal pulse tilt and spatial chirp in noncollinear parametric amplifier can be explained with the help of schematic diagram presented in Fig. 4.1a. In the figure interacting pulses are depicted by iso-intensity lines: red ellipse for signal pulse and green ellipse for pump pulse. In noncollinear amplifier signal

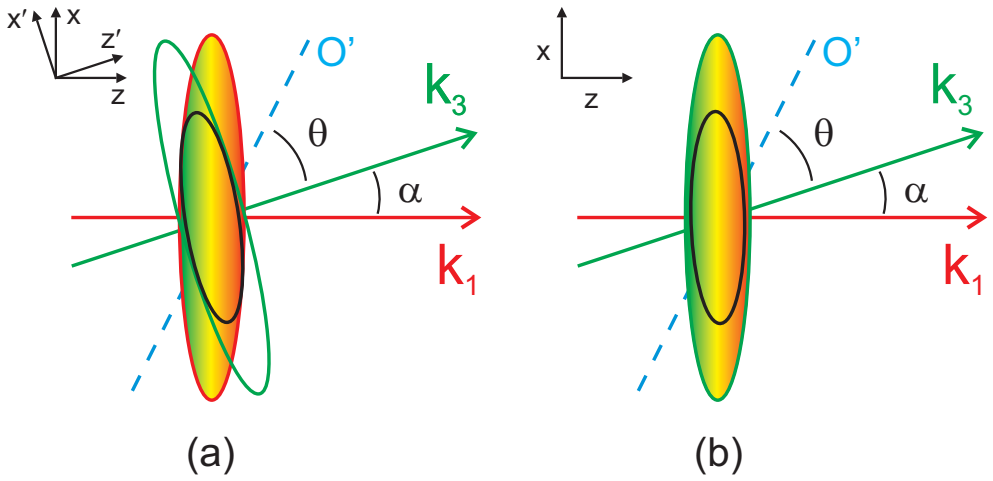

Figure 4.1: Noncollinear interaction scheme when pump and signal fronts are not matched (a) and when pump front is tilted to match the signal front (b). Wave vectors $\mathbf{k}_1$ and $\mathbf{k}_3$ denote propagation direction of signal and pump pulse, respectively; O' denotes the optic axis of nonlinear crystal; θ - phase matching angle, α - noncollinearity angle.

pulse and pump pulse propagates at slightly different directions, which in the figure are indicated by wave vectors $\mathbf{k}_1$ and $\mathbf{k}_3$, respectively. In the case of common noncollinear amplification, the amplitude fronts of signal and pump pulses are not matched and, as a result, the contour of constant gain (black ellipse) is tilted with respect to signal pulse front. Consequently, during parametric amplification the powerful pump pulse makes signal pulse tilted. Furthermore, if input signal pulse is temporally chirped the different spectral components are amplified at different transverse positions (see Fig. 4.1a). Thus, signal pulse acquires spatial chirp, which can be characterized in terms of spatial dispersion or frequency gradient [38]. Obviously, the magnitude of spatial chirp depends on the temporal chirp of the signal.

We note that spatio-temporal distortions can also emerge due to simultaneous temporal and spatial walk-off of pump and signal pulses even if their fronts are perfectly matched in noncollinear amplifier (Fig. 4.1b). However, it requires nonlinear crystal of length comparable or longer than characteristic spatial and temporal walk-off distances of interacting pulses. This case of spatio-temporal distortions buildup is not considered here, since short crystals providing the broadband optical parametric amplification are typically used in practice.

The study is aimed to give an explanation on how the spatial chirp and angular dispersion can emerge just from signal pulse temporal chirp and front mismatch of signal and pump pulses (Fig. 4.1a). For that reason we are using analytical model of undepleted-pump parametric interaction with omitted dispersion and diffraction terms. Such model of the stationary parametric amplification shows that spatial chirp and angular dispersion could be produced "instantly" and are merely the result of the product of signal and pump pulse envelopes. Obviously, this model is valid only when nonlinear crystal is considerably shorter than the characteristic lengths of dispersion and diffraction effects. If such condition is not satisfied the dispersion and diffraction terms should be included (it is done in numeric experiments presented in Sect. 4.3). However, the inclusion of dispersion and diffraction effects will make just some distortions and reductions to the "instantly" produced spatial chirp and angular dispersion.

The characteristics of the spatial chirp and angular dispersion were examined using analytical expressions derived from the approximate solution of coupled differential equations describing three wave parametric interaction in undepleted-pump approximation. Assuming that pump intensity is so high that large amplification factor is achieved in short nonlinear medium, the diffraction as well as dispersion effects can be neglected. Then complex amplitude of the signal pulse, amplified in the field of transform-limited pump and in the case of perfect phase matching, is readily found to be [109]

$$A_1(t, x, z) = A_1(t, x, z = 0) \cosh(A_3(t, x)\sigma z), \tag{4.2.1}$$

where $A_1(t, x, z = 0)$ and $A_3(t, x)$ are the amplitudes of signal and pump pulses at the entrance of amplifier; σ is the nonlinear couping coefficient

$$\sigma = \frac{\omega_1 \omega_2}{2c^2} \frac{\chi_{\text{eff}}}{\sqrt{k_1 k_2}}, \tag{4.2.2}$$

where $\chi_{\text{eff}} = 2d_{\text{eff}}$ is the effective nonlinear susceptibility, ω_1 and ω_2 are the carrier frequencies of signal and idler pulses, respectively, k_1 and k_2 are their correspond-

ing wavenumbers in nonlinear crystal. In the case of large gain ($A_3(t,x)\sigma z \gg 1$) the asymptotic approximation $\cosh(x) \approx \frac{1}{2}\exp(x)$ becomes valid. Thus

$$A_1(t,x,z) \approx \frac{1}{2} A_1(t,x,z=0)\exp(A_3(t,x)\sigma z). \tag{4.2.3}$$

We assume that initial signal pulse is Gaussian and linearly chirped:

$$A_1(t,x,z=0) = A_{10}\exp\left(-\frac{t^2}{\tau_1^2}(1-i\gamma) - \frac{x^2}{\rho_1^2}\right), \tag{4.2.4}$$

where τ_1, ρ_1, γ are the pulse duration, the beam diameter and the temporal chirp parameter of the signal, respectively. Pump pulse is also assumed to be Gaussian:

$$A_3(t',x') = A_{30}\exp\left(-\frac{t'^2}{\tau_3^2} - \frac{x'^2}{\rho_3^2}\right), \tag{4.2.5}$$

where τ_3 is the pump pulse duration and ρ_3 is the pump beam diameter. Due to noncollinear interaction the pump pulse is rotated by internal noncollinearity angle α_{int} in the frame of coordinates (t,x) fixed with the signal pulse, thus its amplitude is given by

$$A_3(t,x) = A_{30}\exp\left[-\frac{\left(tu_3\cos\alpha_{\text{int}} - x\sin\alpha_{\text{int}}\right)^2}{\tau_3^2 u_3^2} - \frac{\left(tu_3\sin\alpha_{\text{int}} + x\cos\alpha_{\text{int}}\right)^2}{\rho_3^2}\right], \tag{4.2.6}$$

where u_3 is the group velocity of the pump pulse. After some reorganizing, Eq. (4.2.6) may be rewritten in a more convenient form:

$$A_3(t,x) = A_{30}\exp\left[-\frac{\left(t-p_0x\right)^2}{\tau^2} - \frac{x^2}{\rho^2}\right], \tag{4.2.7}$$

where τ is the pump pulse duration, ρ is the pump beam diameter and p_0 is the parameter of pump pulse tilt in the frame of the signal pulse coordinates, namely

$$\tau = \tau_3\frac{\rho_3}{\rho}, \tag{4.2.8}$$

$$\rho = \sqrt{\rho_3^2\cos^2\alpha_{\text{int}} + \tau_3^2u_3^2\sin^2\alpha_{\text{int}}}, \tag{4.2.9}$$

$$p_0 = \left(\rho_3^2 - \tau_3^2u_3^2\right)\frac{\cos\alpha_{\text{int}}\sin\alpha_{\text{int}}}{\rho^2u_3}. \tag{4.2.10}$$

In the proximity of the peak of the pump envelope we have $t, x \approx 0$, thus

$$A_3(t,x) = A_{30}\left[1 - \frac{(t-p_0x)^2}{\tau^2} - \frac{x^2}{\rho^2}\right]. \tag{4.2.11}$$

Substituting Eqs. (4.2.4) and (4.2.11) into Eq. (4.2.3), we obtain:

$$A_1(t,x,z) \approx A_0 \exp\left[-\frac{t^2}{\tau_1^2}(1-i\gamma) - \frac{x^2}{\rho_1^2} - \frac{(t-p_0x)^2}{\tau^2}\Gamma z - \frac{x^2}{\rho^2}\Gamma z\right], \tag{4.2.12}$$

where $\Gamma = \sigma A_{30}$ is the small-signal gain coefficient and $A_0 = \frac{1}{2}A_{10}\exp(\Gamma z)$ is the peak amplitude of amplified signal pulse.

The characteristics of induced pulse-front tilt, spatial chirp and angular dispersion can be investigated by analysis of the Eq. (4.2.12). In the following we derive analytical expressions parameterizing the magnitude of the spatio-temporal distortions.

The induced spatial chirp is determined from spatio-spectral intensity distribution $F(\omega, x)$, whereas angular dispersion is determined from spatio-temporal spectrum intensity distribution $G(\omega, k_x)$ [40]. These distributions can be obtained by Fourier transform of the complex amplitude described by Eq. (4.2.12), namely

$$F(\omega,x) = \left|\int_{-\infty}^{\infty} A_1(t,x)\exp(i\omega t)\,\mathrm{d}t\right|^2, \tag{4.2.13}$$

$$G(\omega,k_x) = \left|\iint_{-\infty}^{\infty} A_1(t,x)\exp(i\omega t - ik_x x)\,\mathrm{d}t\mathrm{d}x\right|^2. \tag{4.2.14}$$

By slicing the surface $F(\omega, x)$ at number of frequencies, we obtain a set of functions $F_\omega(x) = F(\omega = \text{const.}, x)$. The beam center position x_0 for each fixed frequency value is defined as a point corresponding to the peak intensity in the slice $F_\omega(x)$. Finally the induced spatial chirp, or more precisely spatial dispersion, is characterized by the slope $\mathrm{d}x_0/\mathrm{d}\omega$ of the retrieved function $x_0(\omega)$ [38].

Similarly, the induced angular dispersion is characterized by the slope $\mathrm{d}k_{x0}/\mathrm{d}\omega$, where $k_{x0}(\omega)$ is a function retrieved by slicing the surface $G(\omega, k_x)$ at fixed frequency values and by finding the spatial frequency value k_{x0} corresponding to the peak intensity in each slice. Note that spatial frequency k_{x0} is a projection

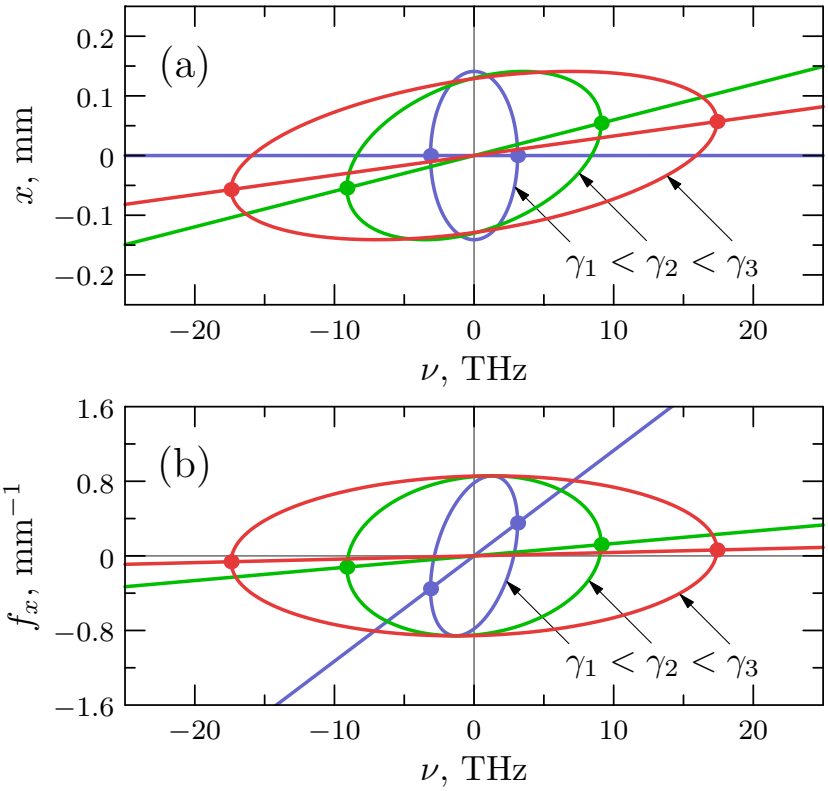

Figure 4.2: Variation of the iso-intensity lines of normalized spectra defined by conditions (a) $F(2\pi\nu, x) = \frac{1}{2}$ and (b) $G(2\pi\nu, 2\pi f_x) = \frac{1}{2}$ when increasing temporal chirp parameter γ of the signal pulse: $\gamma_1 = 0$, $\gamma_2 = 5$, $\gamma_3 = 10$. Filled circles correspond to the most-distant points of iso-intensity lines along the frequency axis. $\tau_3 = 300$ fs (FWHM), $u_3 = 0.2$ μm/fs, $\rho_3 = 1$ mm (FWHM), $\Gamma z = 9$, $\alpha_{\text{int}} = 2.6$ deg, $\tau_1 = 100$ fs (FWHM), $\rho_1 = \rho_3$.

of the wave vector $\mathbf{k}$ onto x axis, namely $k_{x0} = |\mathbf{k}| \sin\beta_0$, where β_0 is the angle between propagation direction of the spectral component and the z axis. Using this relation angular dispersion could be readily expressed in a common form as the propagation angle dependence on frequency $\mathrm{d}\beta_0/\mathrm{d}\omega$ [39].

Note that functions $x_0(\omega)$ and $k_{x0}(\omega)$, corresponding to the Gaussian pulse with linear front tilt and linear temporal chirp, are linear as well and can be derived analytically from geometrical considerations. Any linear function is determined just by two points, thus the desired functions can be obtained by finding two the most-distant points of the iso-intensity line of $F(\omega, x)$ and $G(\omega, k_x)$ distributions along the frequency axis (Fig. 4.2). The straight line crossing these two marginal points determines the position of all the points that would be retrieved from the slicing method described above. Thus we have obtained the analytical expressions relating the slopes of $x_0(\omega)$ and $k_{x0}(\omega)$ functions to temporal and spatial

parameters of the interacting pulses:

$$\frac{\mathrm{d}x_0}{\mathrm{d}\omega} = \frac{\gamma A_{\mathrm{sd}}}{\gamma^2 B + C} \tag{4.2.15}$$

and

$$\frac{\mathrm{d}k_{x0}}{\mathrm{d}\omega} = \frac{A_{\mathrm{ad}}}{\gamma^2 B + C}, \tag{4.2.16}$$

where

$$A_{\mathrm{sd}} = \tfrac{1}{2} p_0 \tau_1^2 \rho_1^2 \tau_3'^2 \rho_3'^2, \tag{4.2.17}$$

$$A_{\mathrm{ad}} = p_0 \tau_1^2 \left(\left(\tau_1^2 + \tau_3'^2 \right) \left(\rho_1^2 + \rho_3'^2 \right) + p_0^2 \rho_1^2 \rho_3'^2 \right), \tag{4.2.18}$$

$$B = \tau_3'^2 \left(\tau_3'^2 \left(\rho_1^2 + \rho_3'^2 \right) + p_0^2 \rho_1^2 \rho_3'^2 \right), \tag{4.2.19}$$

$$C = \left(\tau_1^2 + \tau_3'^2 \right) \left(\left(\tau_1^2 + \tau_3'^2 \right) \left(\rho_1^2 + \rho_3'^2 \right) + p_0^2 \rho_1^2 \rho_3'^2 \right). \tag{4.2.20}$$

In the preceding equations we have denoted $\tau_3' = \tau / \sqrt{\Gamma z}$ and $\rho_3' = \rho / \sqrt{\Gamma z}$.

Also, in the equivalent way, the analytical expression for the parameter characterizing pulse tilt of the amplified signal in (t, x) plane was obtained from the intensity distribution $|A_1(t, x, z)|^2$:

$$p = \frac{\mathrm{d}t_0}{\mathrm{d}x} = \frac{p_0}{1 + \tau_3'^2 / \tau_1^2}, \tag{4.2.21}$$

where $t_0(x)$ is the dependence of pulse delay on transverse position in the beam.

In this study we are addressing the dependence of the induced spatial chirp and angular dispersion on the initial temporal chirp of the signal. Thus in the following analysis only the temporal chirp parameter γ is being varied, while other initial parameters of the pulses are fixed.

The straight lines in Fig. 4.2 depict the induced spatial and angular dispersions for the three different values of the temporal chirp parameter. Spatial dispersion is depicted in Fig. 4.2a as $x_0(\nu) = 2\pi \dfrac{\mathrm{d}x_0}{\mathrm{d}\omega} \nu$, and angular dispersion is depicted in Fig. 4.2b as $f_{x0}(\nu) = \dfrac{\mathrm{d}k_{x0}}{\mathrm{d}\omega} \nu$.

For the fixed signal pulse duration, the greater value of the temporal chirp parameter γ corresponds to the broader bandwidth of the signal pulse (see Fig. 4.2).

Since signal beam diameter and thus the width of the spatial spectrum for the certain interaction geometry are fixed, the increase of chirp parameter γ leads to the reduction of the slopes $\mathrm{d}x_0/\mathrm{d}\omega$ and $\mathrm{d}k_{x0}/\mathrm{d}\omega$, as it can be seen from Fig. 4.2. Namely, in the case of large γ values the magnitude of the induced angular dispersion according to Eq. (4.2.16) vanishes as $1/\gamma^2$. However, the magnitude of the spatial dispersion given by Eq. (4.2.15) reduces just as $1/\gamma$. Thus for the large temporal chirp ($\gamma \gg 1$) the pulse-front tilt of the amplified signal is mainly caused by spatial and temporal chirp. Whereas in case of the transform-limited signal pulse amplification ($\gamma = 0$) the amplified signal pulse has no spatial chirp, but possesses non-zero angular dispersion. Note, that angular dispersion of the amplified signal pulse is caused entirely by the front tilting and is unrelated to the phase matching in nonlinear material. Also note that in the case of interaction when pulse fronts are perfectly matched (Fig. 4.1b) we have $p_0 = 0$, therefore amplified signal pulse is free from spatial and angular dispersions.

As it can be seen from Eq. (4.2.21), signal pulse tilt p depends on the signal-to-pump duration ratio, but is independent of temporal chirp of the signal pulse. The tilt of the signal pulse p is *always* smaller than the tilt of the pump pulse p_0, and decreases when reducing the duration of the signal pulse. Naturally, it is desirable to avoid spatio-temporal distortions, however, if signal pulse duration is much shorter than duration of the pump pulse it would lead to the significant drop in conversion efficiency. Thus in the further analysis signal pulse duration is restricted to $\tau_3/\tau_1 = \sqrt{\Gamma z}$, since this ratio of durations was shown to be the optimum, when considering conversion efficiency and bandwidth of amplified signal pulse [100].

The tilt of the amplified signal pulse essentially depends on the pump pulse tilt p_0. Consequently, sign and magnitude of the signal pulse tilt depends on the ratio of pump pulse duration and pump beam diameter, as it can be seen from Eq. (4.2.10). In case when $\tau_3 u_3 \ll \rho_3$, i.e. in the usual case of femtosecond pulses, the angle of the pulse-front tilt of the pump is close to the noncollinearity angle.

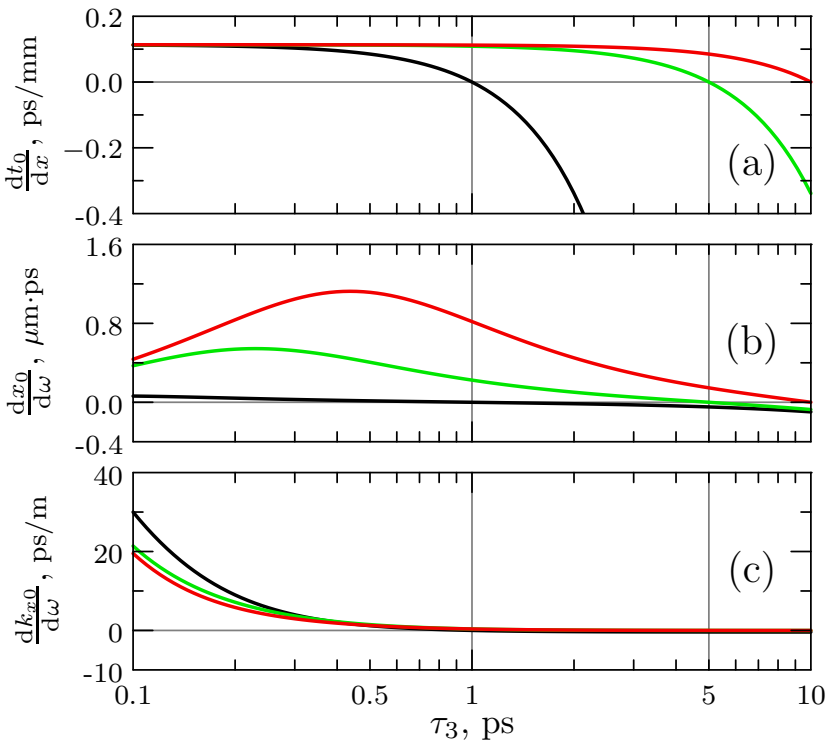

Figure 4.3: Dependences of pulse tilt (a), spatial dispersion (b) and angular dispersion (c) of the amplified signal on the pump pulse duration (FWHM) for the three different pump beam diameters (FWHM): 2 mm (red line), 1 mm (green line), 0.2 mm (black line). $u_3 = 0.2$ μm/fs, $\Gamma z = 9$, $\alpha_{\text{int}} = 2.6$ deg, $\tau_1 = \tau_3/\sqrt{\Gamma z}$, $\rho_1 = \rho_3$, $\tau_{\text{TL}} = 10$ fs (FWHM), $\gamma = \sqrt{\tau_1^2/\tau_{\text{TL}}^2 - 1}$. Note the logarithmic scale of the x-axis.

Whereas, in case when pulse physical length and beam diameter of the pump are equal, i.e. $\tau_3 u_3 = \rho_3$, the tilt of the pump pulse vanishes ($p_0 = 0$) and so does the tilt of the signal pulse. As one can see from Eqs. (4.2.17) and (4.2.18), the spatial dispersion as well as angular dispersion in this case vanish as well. Hence, it is possible to avoid spatio-temporal distortions simply by matching the physical length and beam diameter of the pump. For longer pump pulse durations, i.e. $\tau_3 u_3 > \rho_3$, the tilt of the signal pulse increases in magnitude, but in this case signal pulse is tilted in the opposite direction (see Fig. 4.3a). Note that it is true only while the length of the nonlinear crystal is longer than the physical length of the pump pulse. Otherwise signal pulse front is not effected by the front mismatching of the interacting pulses.

In addition to the dependence of the signal pulse tilt, Fig. 4.3 shows the dependences of spatial and angular dispersions on the pump pulse duration for the three

different pump beam diameters. Note that the dependences of angular dispersion (Fig. 4.3c) are quite far different from the ones of spatial dispersion (Fig. 4.3b). As one can see from Fig. 4.3c, independently from the pump beam diameter, the magnitude of the induced angular dispersion decreases rapidly and becomes negligible for pump pulse durations longer than 1 ps. Whereas the magnitude of spatial dispersion, depending on the pump beam diameter, might be about the same for pump pulse durations in the femtosecond and picosecond scales. Nonetheless the magnitude of spatial dispersion generally increases with the increase of the pump beam diameter. Hence, this figure clearly demonstrates, that the induced spatial and angular dispersions are more pronounced in case of femtosecond pump pulses, when the physical length of the pulses is much less than the diameter of the beams. Note that in this figure the bandwidth of the signal pulse is fixed. Therefore the temporal chirp parameter γ is a function of the signal pulse duration, namely $\gamma = \sqrt{\tau_1^2/\tau_{\mathrm{TL}}^2 - 1}$, where τ_{TL} is transform-limited duration of the signal pulse.

Finally, let us note that diffraction in free space and focusing by the lens of the Gaussian pulses possessing angular as well as spatial dispersion were studied in Sect. 3.2 and Sect. 3.3, respectively.

4.3 Numerical experiments

In order to check the findings we have performed numerical experiments of the three-wave parametric interaction in BBO nonlinear crystal, using the symmetrized split-step method [64, 102]. According to this method the medium was divided into number of slices. Diffraction and material dispersion were accounted for in each slice independently from the nonlinearity of material. The linear propagation of the waves was handled in the Fourier space in accordance with Eq. (2.1.22)

$$A_j(t,x,y,z) = \mathscr{F}^{-1}_{\Omega,k_x,k_y}\left\{\mathscr{F}_{t,x,y}\left\{A_j(t,x,y)\right\}\exp\left(-i\sqrt{k(\omega,k_x)^2 - k_x^2 - k_y^2}z\right)\right\}, \tag{4.3.1}$$

where j=1,2 and 3 indicate signal, idler and pump respectively, and $\mathscr{F}$ denotes the Fourier transformation. Dispersion and diffraction effects are accounted for via exponential term in Eq. (4.3.1), where $k(\omega, k_x) = \frac{\omega}{c} n(\omega, k_x)$ is the magnitude of the wave vector and $n(\omega, k_x)$ is the refractive index. The spatial walk-off of the extraordinary wave due to birefringence was taken into account via $n(\omega, k_x)$ dependence on k_x, that is, on propagation direction (Eq. (2.1.24)).

The nonlinear step, accounting for the three-wave parametric interaction, was performed using fourth-order Runge–Kutta method for integration of the coupled three-wave equations (2.2.8) in the near field representation (t, x, y)

$$\begin{aligned} \frac{\partial A_1}{\partial z} &= -i \frac{w_1^2}{2k_1 c^2} \chi_{\text{eff}}^{(2)} A_3 A_2^*, \\ \frac{\partial A_2}{\partial z} &= -i \frac{w_2^2}{2k_2 c^2} \chi_{\text{eff}}^{(2)} A_3 A_1^*, \\ \frac{\partial A_3}{\partial z} &= -i \frac{w_3^2}{2k_3 c^2} \chi_{\text{eff}}^{(2)} A_1 A_2. \end{aligned} \tag{4.3.2}$$

Note that for the nonlinear step, a slowly varying envelope approximation was assumed (Eq. (2.2.5)).

In numerical experiments it was also accounted for self-focusing and cross-focusing as well as self-phase and cross-phase modulation, due to third order nonlinearity of the BBO material. The intensity dependent spatio-temporal phase modulation was accounted in each step under slowly varying envelope approximation in accordance with Eq. (2.2.8)

$$A_j(t, x, y, z) = A_j(t, x, y) \exp \left[-i \frac{\omega_j}{c} n_2 \left(I_j(t, x, y) + 2 \sum_{k=1, k \neq j}^{k=3} I_k(t, x, y) \right) z \right], \tag{4.3.3}$$

where $I_j(t, x, y)$ is the intensity of the wave and ω_j is its central frequency. The nonlinear refractive index was taken to be $n_2 = 5.5 \times 10^{-16}$ cm^2/W [110]. However, the modifications of the characteristics of amplified signal pulse due to Kerr effect were negligible.

Numerical experiments were performed for the case of type-I (oo-e) interaction

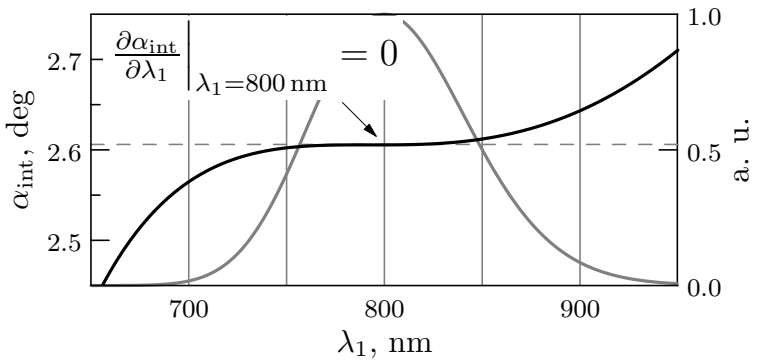

Figure 4.4: Calculated phase-matching curve (black line) at the magic phase-matching angle of $\theta = 24.67$ deg in type-I BBO crystal pumped by $\lambda_3 = 512$ nm. Signal pulse spectrum corresponding to 10 fs transform-limited Gaussian pulse is depicted by gray solid line.

in 1.5 mm long BBO crystal at the phase matching angle $\theta = 24.67$ deg and internal noncollinearity angle $\alpha_{\rm int} = 2.6$ deg. In what follows, these angles were found for the broadband phase matching of 512 nm pump wavelength and 800 nm signal wavelength.

In case of perfect phase matching, wave vectors of interacting waves form a triangle, from which noncollinearity angle can be obtained [14]

$$\cos(\alpha_{\rm int}(\lambda)) = \frac{k_1^2 + k_3^2 - k_2^2}{2k_1k_3}. \tag{4.3.4}$$

Broadband phase matching in the vicinity of 800 nm wavelength is ensured by setting the condition:

$$\frac{\partial\alpha_{\rm int}}{\partial\lambda_1}\Big|_{\lambda_1=800\,\rm nm} = 0. \tag{4.3.5}$$

Thereby solving this equation for θ, the "magic" phase-matching angle was found. As it follows from Eq. (4.3.5), the noncollinearity angle $\alpha_{\rm int}(\lambda)$ keeps nearly constant value for broad spectral range (see Fig. 4.4), thus the broadband signal pulse free from the induced angular dispersion can be amplified [26].

In numerical experiments, the durations of pump and signal pulses were set to 300 fs and 200 fs (FWHM), respectively. The bandwidth of the chirped signal pulse corresponded to 10 fs transform-limited pulse duration. Thus it resulted in temporal chirp parameter of $\gamma = 20$. Beam diameters of signal and pump were equal to 1 mm (FWHM), whereas peak intensities were 40 GW/cm^2 for the pump

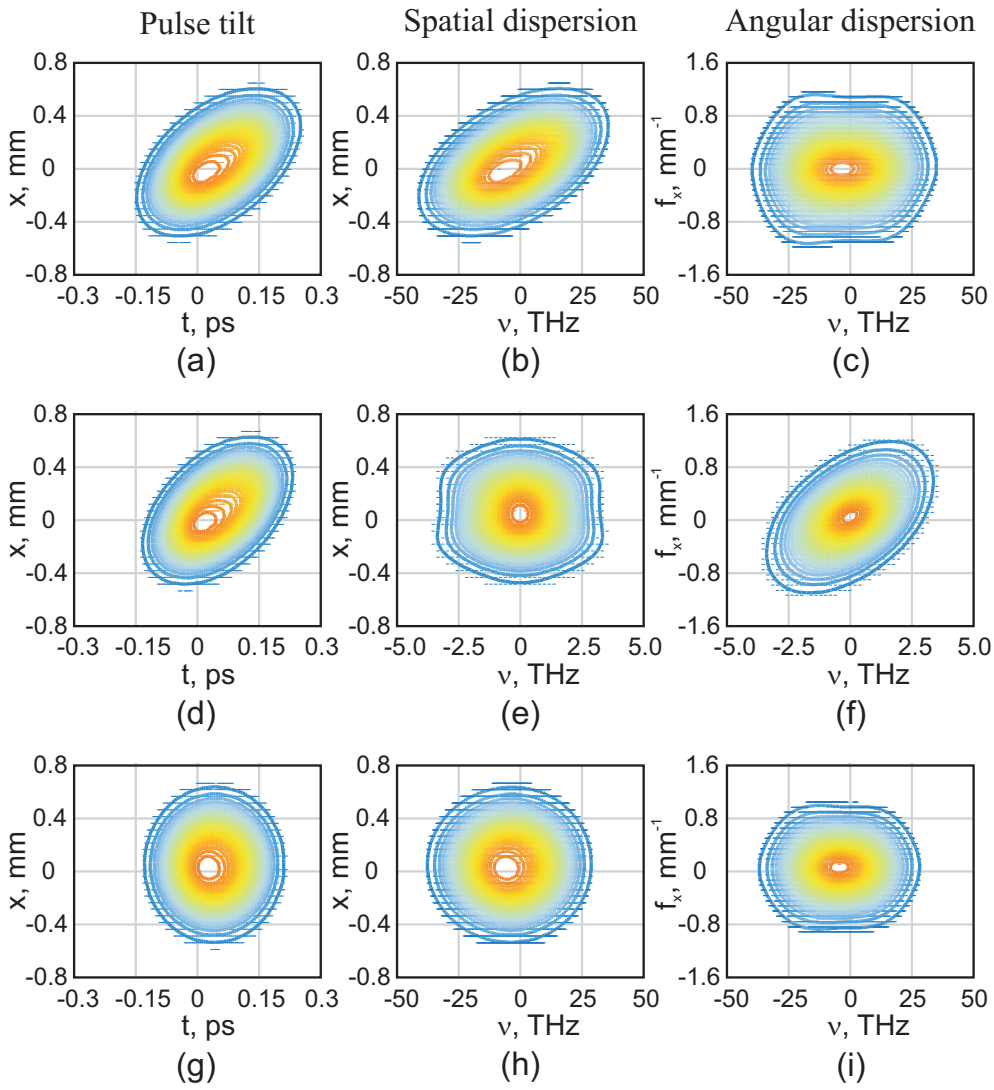

Figure 4.5: Normalized intensity profiles of amplified signal pulse in three different domains (see text) for the three different input conditions: (a-c) when signal pulse is temporally chirped ($\gamma = 20$); (d-f) when signal pulse is transform limited ($\gamma = 0$); (g-i) when fronts of signal and pump pulses are matched ($\gamma = 20$). Note that the scale interval of frequency axis is reduced ten times in (e) and (f) due to narrow bandwidth of transform limited signal.

and 0.03 GW/cm^2 for the signal. Pulse and beam profiles were Gaussian. The coefficients of Sellmeier equations given by Kato [111] were used and the effective second order nonlinear susceptibility was taken to be $\chi^{(2)}_{\text{eff}} = 4$ pm/V [102].

Results of numerical experiments are summarized in Fig. 4.5. Three rows of graphs correspond to the three different input conditions: results in case of temporally chirped ($\gamma = 20$) signal pulse amplification when fronts of the pulses are not matched are presented in the first row (a-c graphs), for the same initial conditions, but in case of transform limited ($\gamma = 0$) signal pulse amplification,

results are presented in the second row (d-f graphs) and in the third row (g-i graphs) results for the case of pulse-front matching are presented. Three columns in the figure correspond to three different domains of normalized intensity distributions of the amplified signal pulse: the first column (a, d, g graphs) depicts near field intensity distributions $|A(t,x)|^2$, the second column (b, e, h graphs) depicts the spatio-spectral intensity distributions $F(2\pi\nu, x)$ and the third column (c, f, i graphs) depicts the far field intensity distributions $G(2\pi\nu, 2\pi f_x)$. One can see from the graphs presented in the first row that, after amplification of temporally chirped signal pulse, it becomes tilted (Fig. 4.5a) and has spatial chirp (Fig. 4.5b), but its angular dispersion is negligibly small (Fig. 4.5c). Whereas from the graphs presented in the second row one can see that after amplification of the transform limited signal pulse it has no spatial chirp (Fig. 4.5e), but acquires angular dispersion (Fig. 4.5f). Note that in this case signal pulse tilt (Fig. 4.5d) is nearly the same as in the case of temporally chirped signal pulse amplification.

Lastly, in the case of pulse-front matching, i.e. in case of interaction geometry depicted in Fig. 4.1b, as expected, amplified signal pulse has no spatio-temporal distortions (see Fig. 4.5g, 4.5h, 4.5i). However, the results of numerical experiments show that pulse-front matching leads to narrower bandwidth of the amplified signal pulse. In the case of pulse-front matching signal bandwidth at FWHM was 1067 cm^{-1}, whereas in the case when fronts were not matched the bandwidth was 1242 cm^{-1}. Pump-to-signal energy conversion efficiencies were calculated to be 12.6 % and 11.2 %, respectively. Better spatio-temporal overlap of signal and pump pulses leads to higher conversion efficiency in the case of matched fronts, however, the broader bandwidth is achieved when fronts are not matched due to longer effective duration of the pump pulse. Hence, when signal and pump pulse fronts are mismatched the bandwidth of the amplified signal pulse depends not only on signal-to-pump duration ratio and temporal profile of the pump pulse [100, 102], but also, on pump beam diameter and spatial profile as well. This is a result of space-time coupling introduced by the rotated pump pulse, as it

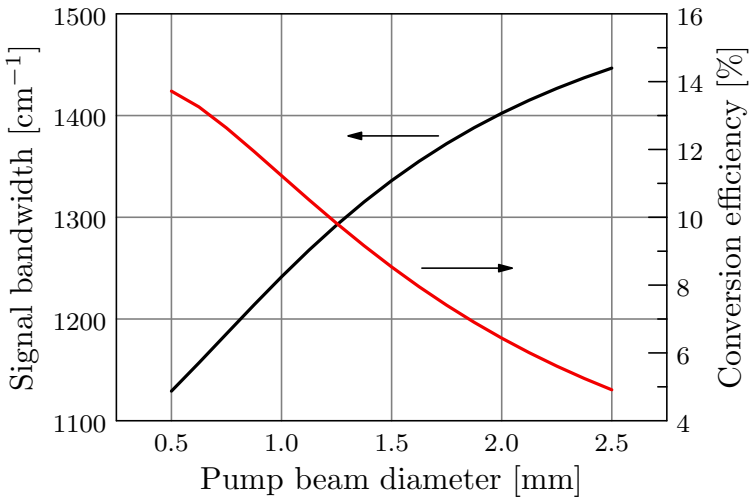

Figure 4.6: Dependences of FWHM bandwidth of amplified signal pulse (black line) and pump-to-signal energy conversion efficiency (red line) on pump beam diameter (FWHM) in case when fronts are not matched.

can be seen from Eqs. (4.2.8)–(4.2.10). The dependences of the signal bandwidth and pump-to-signal energy conversion efficiency on the pump beam diameter are depicted in Fig. 4.6. As one can see, the broader bandwidth can be achieved with the increase of the pump beam diameter, however at the cost of conversion efficiency.

4.4 Experimental verification

The experiment was carried out in two-stage NOPA [A2], driven by femtosecond Yb:KGW laser system ("PHAROS", Lightcon Ltd.), which after second harmonic generation was delivering 200 μJ and 300 fs pulses centered at 512 nm. White light continuum, generated in a bulk sapphire and then precompressed in a prism pair compressor, was used as a broadband seed in this setup. The amplification was performed in type-I BBO crystal at the phase-matching angle $\theta = 24.6$ deg and internal noncollinearity angle α_{int} close to 2.6 deg. In the first amplification stage seed and pump beams were focused into 1.5 mm long BBO crystal, where signal pulses were amplified to 1 μJ energy. The spatio-temporal distortions of the signal pulse were negligible in this stage due to small beam size, which was nearly 70 μm at FWHM. Further signal beam was expanded to 1.2 mm diameter

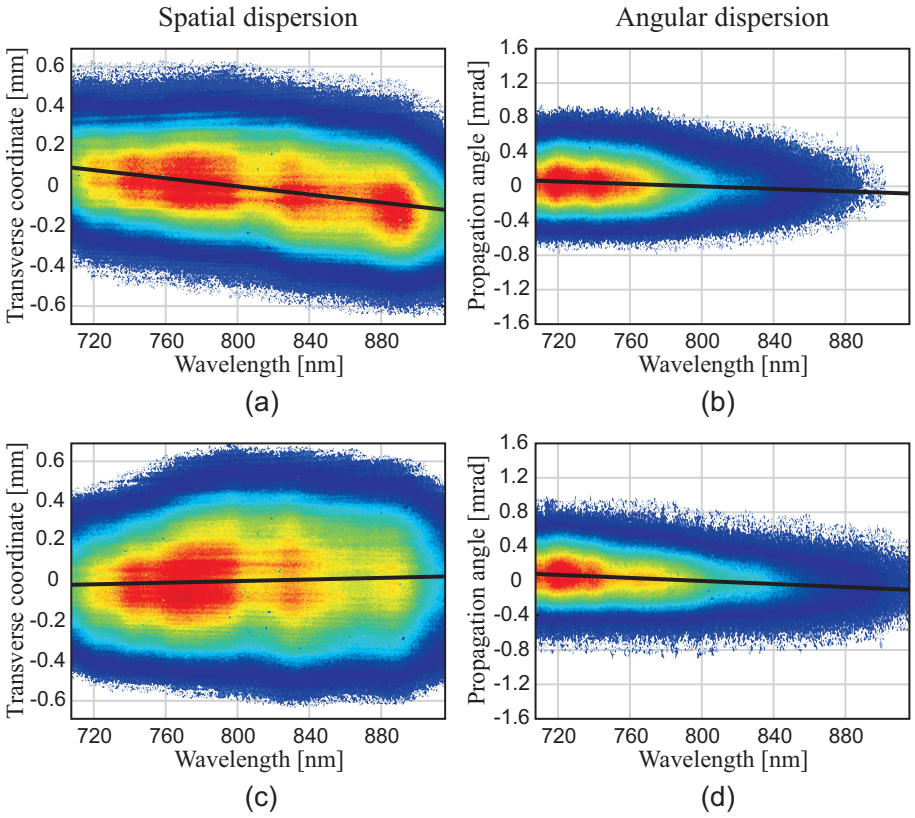

Figure 4.7: Spatio-spectral intensity distributions $F(\lambda, x)$ (a, c graphs) and far field intensity distributions $G(\lambda, \beta)$ (b, d graphs) of amplified signal pulse in case of not matched fronts (first row) and in case of matched fronts (second row).

and collimated to the second 2.5 mm long BBO crystal, where it was amplified from 0.8 μJ to 14 μJ energy. The estimated signal pulse duration was 200 fs, while its bandwidth corresponded to the transform limited pulse duration of 10 fs and to the chirp parameter value of 20. Peak intensity of the pump pulse in the second stage was 35 GW/cm^2.

The spatio-temporal distortions of the amplified signal pulse were investigated in both matched-front and non-matched-front cases of noncollinear parametric amplification. For the measurements of angular and spatial distributions of the signal spectrum an imaging spectrometer similar to one described in [66] has been used, except that achromatic lenses were replaced by spherical mirrors in the current setup. For measurements of the angular dispersion the signal beam was focused into the entrance slit of the spectrometer by spherical mirror of 1 m focal length placed at a focal distance from the slit, whereas for spatial chirp measure-

ments, the mirror was moved to the position required for the exact imagining of the BBO output plane onto the entrance slit.

Initially, spatial chirp and angular dispersion were measured for the signal pulse before amplification, indicating that spatio-temporal distortions are undetectable within our experimental accuracy. However, the experimental results for the amplified signal pulse show that in the case of not matched pulse fronts the amplified signal pulse acquired spatial dispersion of $dx_0/d\lambda = 1\,\mu$m/nm (Fig. 4.7a), whereas angular dispersion was found to be negligible (Fig. 4.7b). The residual angular dispersion alone would correspond to the pulse-front tilt of approximately 0.03-0.04 deg which is insignificant compared to the noncollinearity angle in this interaction. This leads to the conclusion that pulse-front tilt is related to the simultaneous presence of spatial and temporal chirp. After the pump pulse front was tilted employing BK7 prism of 67 deg apex angle in order to match the fronts of signal and pump pulses neither spatial chirp (Fig. 4.7c) nor angular dispersion (Fig. 4.7d) were observed after amplification.

4.5 Conclusions

We have investigated spatio-temporal distortions acquired by signal pulse in noncollinear OPCPA due to pulse-front mismatch. The analytical expressions derived from the solution of the coupled wave equations of three-wave interaction allows for easy analysis of pulse-front tilt, spatial and angular dispersion. It was shown that the acquired pulse tilt by the signal is always smaller than the tilt of the pump pulse, and that both vanish when the physical length of the pump pulse is equal to its diameter. The results of analytical treatment complemented by numerical experiments in the (3D+1) space has shown that in case of amplification of strongly chirped signal pulse in NOPA, it acquires spatial chirp as well as pulse-front tilt, however the angular dispersion is negligible. On the contrary, when transform limited signal pulse is amplified, at the output it is also tilted, but possess angular dispersion only. Theoretical findings were verified by experiment.

Chapter 5

Compressor-less OPXPA with subsequent space-time focusing

Material related to this chapter was published in [A3]

Optical parametric chirped-pulse amplification (OPCPA) [3] has became a widely recognized technique [7, 9, 10, 112, 113, 114, 115] and recently was investigated for generation of few-cycle light pulses with petawatt peak powers [108, 116] and beyond [92]. In particular, the broad amplification bandwidth of the optical parametric amplifier is provided by the noncollinear interaction geometry. When combined with an angularly dispersed signal beams, it could yield still broader parametric bandwidths [21, 22, 23]. Additionally, the use of angular dispersion could open the route for parametric amplification of chirped X-pulses, featuring temporal compression during propagation in free space [24, 25]. For the case of high-peak-power pulses this feature would be of particular importance, since in contrast to ordinary OPCPA technique, the pulse compressor is no longer needed. Yet the realization of such compressor-less idea has been left to be proven as obtaining a particular X-pulse for seeding is obscure.

The main requirement for the X-pulse to be seeded is actually the same as for Gaussian-shaped pulses, namely, the angular dispersion of the pulse must be perfectly matched with the phase-matching curve. One realistic possibility for obtaining such X-pulses was experimentally demonstrated in [27, 28]. It has been

proven that X-pulses, or pulsed conical waves (PCWs) in general, with the angular dispersion, which corresponds to the phase-matching curve, can be obtained by parametric amplification of the tightly focused signal. Remarkably, due to tight focusing the initial Gaussian-shaped beam is self-adopted by the parametric amplifier and is transformed into conical one, defined by the phase-matching condition (a more detailed explanation is given in the next section). Therefore, there is no need to apply any angular dispersion to the seeded pulse. However, in those works, parametric amplification was performed in the near field of the tightly focused signal, thus resulting in gain saturation without appreciable energy transfer from the pump. In this contribution, we present a method that allows to avoid amplification of the near field possessing the intense central spike. In our method, the far field of the tightly focused signal is amplified. Therefore, a sudden manifestation of the saturation regime is avoided. This is a simple, yet essential improvement regarding the previous works.

This study is aimed to deliver a new approach in generation and amplification of few-cycle high-peak-power light pulses by means of optical parametric amplification (OPA). The proposed method combines the major features of OPA and chirped-pulse amplification (CPA), namely, the ultra-broad parametric bandwidth, which is achieved by achromatic phase matching, and amplification of stretched seed pulse, which is achieved by performing the far field amplification of the PCW. Moreover, these features are brought in a simple setup, in which a pulse compressor is dismissed.

5.1 Gaussian wave-packet reshaping into conical via parametric amplification of the far field

There are many works that consider the ways of achieving a broadband phase matching. However, none of them points out that one of the easiest way to achieve the broadband phase matching is by tightly focusing the signal beam. Recently it was demonstrated, that broad angular spectrum of the tightly focused signal

beam can be exploited in generation and amplification of pulsed Bessel beams [27] and conical wave-packets in general [28]. In the following it is demonstrated, that such amplification is particularly suitable for pulsed conical wave parametric amplification (PCWPA) with subsequent spatio-temporal compression during propagation in free space.

In case of parametric amplification of tightly focused signal, the angular dispersion, corresponding to the phase matching curve, is imprinted in the signal pulse. Usually, the imposed angular dispersion is considered as a drawback that must be corrected for [26]. However, in the scheme presented below it is a workhorse empowering temporal compression of the amplified signal pulse during propagation in free space. This feature is of particular importance and is a major advantage over ordinary OPCPA technique, since there is no need for pulse compressor.

In the following, we numerically demonstrated that Gaussian wave-packet can be reshaped into pulsed conical wave just by means of lens and nonlinear crystal. We pointed out that performing the far field amplification of the PCW is the key for generation of localized PCWs with ultrahigh intensities. It allows to form ultra-intense and propagation invariant wave-packets capable to propagate over many Rayleigh range in the desired material.

The scheme under consideration is depicted in Fig. 5.1. Actually it is cylindrical symmetric, except that the optic axis of the nonlinear crystal is not. In what follows, the main clues of the proposed method are explained using the results of the numerical experiment, from which intensity profiles of the signal pulse are depicted in the distinctive space and time domains.

The basic idea is to achieve broadband phase matching simply by sending signal pulse with wide angular spectrum into the nonlinear crystal [117]. Therefore, we put lens in front of the nonlinear crystal. In such case the optical parametric amplifier becomes achromatically phase matched, i.e. phase mismatch is equal to zero for all signal wavelengths along the phase-matching curve. Thus, the width of the amplified temporal spectrum is virtually not limited by the nonlinear

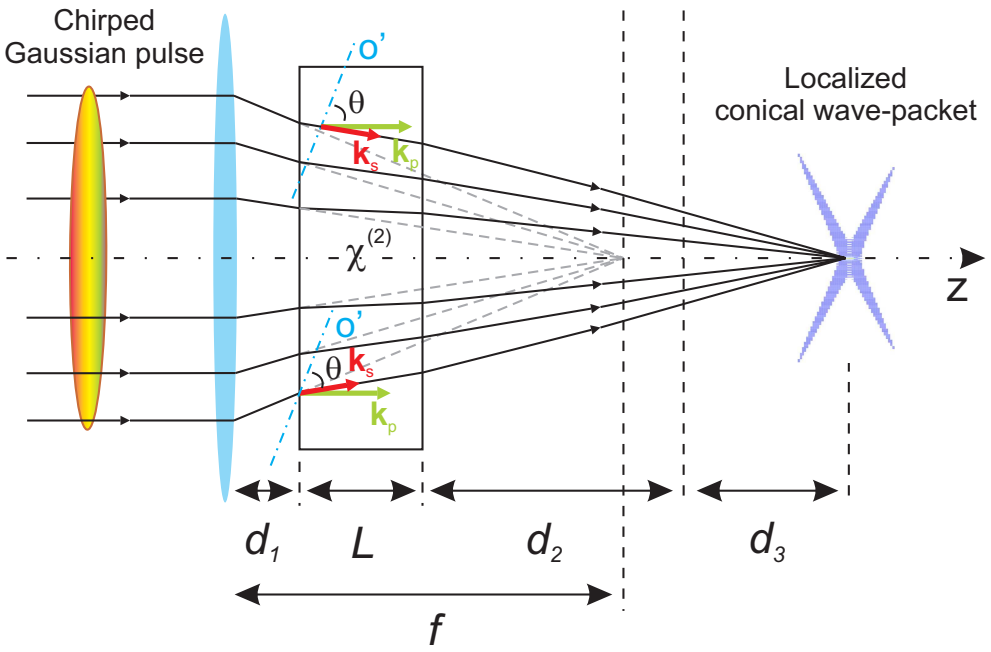

Figure 5.1: Schematic representation of interacting waves. $\mathbf{k}_s$ and $\mathbf{k}_p$ denote wave vectors of signal and pump waves, respectively; O' denotes the optic axis of nonlinear crystal; θ - phase-matching angle; f - focal length of the lens; L - the length of the nonlinear crystal; d_1 - the distance between the lens and the entrance plane of the nonlinear crystal; d_2 - the distance between the exit plane of the nonlinear crystal and the actual position of the focal plane of the lens; d_3 the distance between the focal plane and the center of the Bessel-zone.

crystal, unless absorption takes place or phase matching for certain wavelengths is simply not possible. Yet only those angular components that lay in the vicinity of the phase-matching curve are amplified by the pump pulse. Consequently, the amplified angular spectrum becomes ring-shaped (Fig. 5.2a, vivid). The diameter of the ring is determined by the phase-matching condition, whereas the width of the ring at each signal wavelength depends on the acceptance angle of the nonlinear crystal for that wavelength [118]. In such a way the angular spectrum of the broadband PCW is formed during the parametric amplification.

Note that it is not obligatory for the lens to be close to the nonlinear crystal. Actually, the results of the experiment would not change at all, if, for the fixed position of the nonlinear crystal relative to the back focal plane of the lens, the distance between the lens and the nonlinear crystal was increased. However, an appropriate scaling of the focal length and diameter of the signal beam in front of the lens must be ensured, since the width of the angular spectrum of signal beam in front of the nonlinear crystal must be preserved.

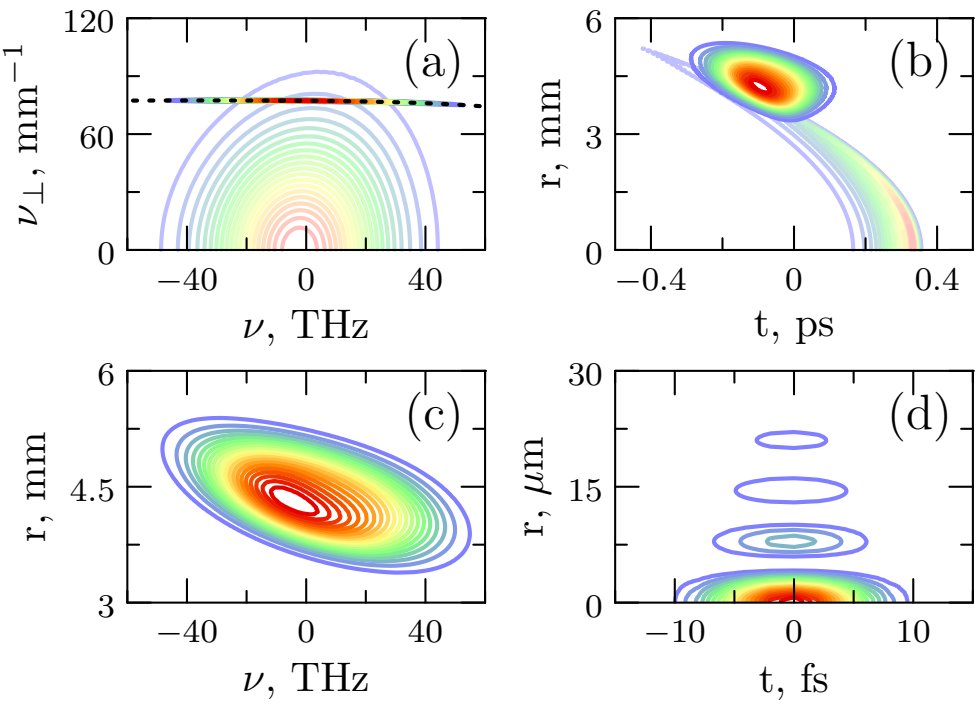

Figure 5.2: (a) Spatio-temporal spectrum of the signal pulse before (dimmed) and after (vivid) amplification in nonlinear crystal; phase-matching curve is depicted by black dotted line; $\nu_\perp$ denotes the spatial frequency $\nu_\perp = k_\perp/2\pi$, and ν denotes the temporal one $\nu = \Omega/2\pi$. (b) Spatio-temporal profile of the signal pulse before (dimmed) and after (vivid) amplification in nonlinear crystal. (c) Spatio-spectral intensity distribution of the amplified signal pulse. (d) Spatio-temporal profile of the amplified signal pulse at the center of the Bessel-zone. Depicted signal profiles correspond to DKDP$^{(1)}$ case (see text for more details). All graphs are normalized.

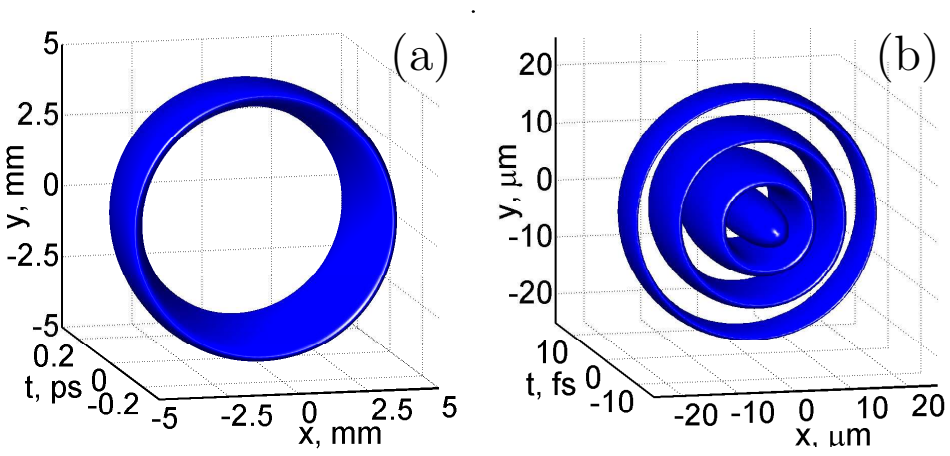

Figure 5.3: Iso-intensity profile of the formed PCW at the exit plane of the nonlinear crystal (a) and at the center of the Bessel-zone (b). Iso-intensity profiles are depicted at 0.5 and 0.05 levels of the peak intensity, respectively. Note that the scales in (a) and (b) are different.

After the lens, signal pulse possess broad angular spectrum and, in addition, acquires a parabolic spatio-temporal profile (Fig. 5.2b, dimmed). Such profile is caused by distinct group velocity delay at different transverse position of the lens.

However, the amplification is selective and just a particular part of the signal pulse, where angular components are phase matched with the pump, is amplified. Under such amplification conditions signal pulse becomes ring-shaped (Fig. 5.2b, vivid). Furthermore, signal pulse acquires the spatial chirp (Fig. 5.2c) [38], since different wavelengths are amplified at slightly different positions across the signal beam. Thereby, due to selective amplification and focusing the far field of PCW is formed with all the wave vectors directed to the focus.

During propagation in free space toward the focus, the far field evolves, and finally, results in the near field of the localized PCW. The actual shape of the spatio-temporal profile of the localized PCW is defined by its angular dispersion [119, 120]. In our case the angular dispersion is not a free parameter and is defined by the phase-matching condition. In this particular case, the spatio-temporal profile (Fig. 5.2d) closely corresponded to a so-called pulsed Bessel–Gaussian beam [95]. The propagation of such pulse is characterized by Bessel-zone, where the peak intensity reaches extreme values and the beam diameter is nearly constant. Actually, pulsed Bessel–Gaussian beams have attracted a considerable interest due to their superior features over pulsed Gaussian beams in high-order harmonic generation [121, 122].

The iso-intensity profiles of the formed PCW at the exit plane of the nonlinear crystal and at the center of the Bessel-zone are depicted in Fig. 5.3. These profiles were retrieved from the corresponding intensity profiles of Fig. 5.2b and Fig. 5.2d.

It is important to note, that nonlinear crystal performs as a spatial spectrum filter in this scheme, selecting only those angular components of the signal pulse that are phase matched with the pump. Therefore, signal pulse with the arbitrary profile can be reshaped into PCW. It is also noteworthy, that the ultra-broad gain bandwidth in this scheme is not restricted to the specific phase-matching angles as it is common in OPCPA setups. Moreover, by changing the phase-matching angle or, generally, nonlinear crystals as well as wavelengths of interacting waves it is possible to form PCWs with miscellaneous types of angular dispersion and

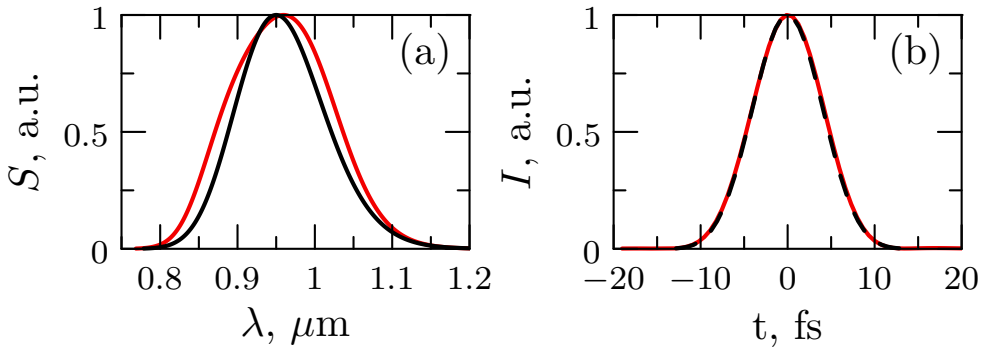

Figure 5.4: (a) Spectral power of the amplified signal pulse (red line); black line depicts initial spectrum of the Gaussian signal pulse. (b) On-axis temporal profile of the amplified signal pulse at the center of the Bessel-zone (red line); black dashed line depicts its Fourier transform-limited profile. All graphs are normalized.

linear propagation features [28, 123]. Therefore, PCWPA could stand as versatile tool for formation and amplification of PCWs with the specific angular dispersion adjusted for each application.

Also note that amplified temporal spectrum resembles the initial Gaussian spectrum (Fig. 5.4a, red line). In addition, it has no significant modulation nor sharp side peaks, that may emerge in the OPCPA setups employing a fixed non-collinearity angle for all signal wavelengths [102, 108]. As a result the on-axis temporal profile of the localized PCW is also nearly Gaussian and is free from significant pre- and post-pulses (Fig. 5.4b, red line). Such uniform amplification of the whole signal spectrum was achieved by achromatic phase matching and a flat-top pump pulse.

The spatio-temporal profile of the amplified signal pulse (Fig. 5.2b, vivid), i.e. the far field of the PCW, is mainly determined by the interplay between the acquired angular dispersion and spatial chirp. It actually suggests that the far field of the PCW can be obtained in advance, i.e. without the explicit simulation of the parametric interaction. It can be done by calculating back-propagation, from the focus to the nonlinear crystal, of transform-limited PCW with the specified angular dispersion in free space. This might be very useful when estimating the required duration and diameter of the pump, and also, the actual dimensions of PCW in the far-field. Note that having large spatio-temporal dimensions of

the far field enables to take the key advantage of the CPA technique. Specifically, boosting the energy of the far-field that has a rather low intensity, makes it possible to attain ultrahigh intensity at the focus. In addition, that allows to avoid gain saturation without appreciable energy transfer when the near field with intense central spike is being amplified.

Let us note that the focal length of the lens has no effect on the angle at which the ring-shaped signal beam intersects. This angle is equal to the external noncollinearity angle and is essentially determined by the phase-matching condition. Whereas the focal length of lens determines just the width of the angular spectrum at the entrance of the nonlinear crystal, and the energy of the angular components that are phase-matched with the pump.

By replacing the spherical lens with the cylindrical one in Fig. 5.1, this scheme could be also be applied for parametric amplification of one-dimensional pulsed Bessel–Gaussian beams [124]. Furthermore, if just a half of the signal beam was overlapped by the pump, then an ordinary pulsed Gaussian beam, possessing angular dispersion, could be obtained. However, there should be additional lens in the optical scheme in order to focus this beam. Recall, that focusing of the angularly dispersed pulsed Gaussian beam results in the spatial chirp at the focus, and consequently, a transform-limited duration cannot be achieved (Sect. 3.2).

5.2 Pre-chirping of the signal pulse

Before the exemplifying numerical analysis the pre-chirping of the signal pulse must be considered. Initially, when there is only lens presented in the scheme, signal pulse must be transform-limited in front of the lens in order to have transform-limited duration at the focus. However, when nonlinear crystal is placed after the lens, the spectral phase of the signal pulse must be adjusted before the lens in order to compensate the introduced material dispersion. Material dispersion of the lens is not taken into account, i.e. it is assumed to be a parabolic mirror. Nonetheless, signal pulse is pre-chirped just to compensate the material disper-

sion, and the real CPA effect is essentially determined by the largeness of the spatio-temporal profile of the PCW in the far field. Not all the far fields will work equally well, but those with larger dimensions will enable to gain more energy into PCW. Comprehensive discussion on this issue can be found in Sect. 5.5.

In the ideal case, when parametric amplification does not introduce any aberrations, the localized PCW should be obtained at the focal plane of the lens. However, the signal and idler beams become mutually trapped during the propagation in the nonlinear crystal [125]. Therefore, at the exit plane of the nonlinear crystal, the far field of the PCW appears to be slightly shifted from the z-axis when compared to the ideal case. Consequently, PCW has to propagate some extra distance d_3 in free space from the focal plane of the lens to the actual focus, where it becomes localized (Fig. 5.1). In DKDP$^{(1)}$ case the distance d_3 from the focal plane of the lens to the center of the Bessel-zone was 14.6 mm, and in other two cases it was 22.4 mm (for more details see next section). Due to dispersive propagation of the PCW in free space, this distance must be accounted for in order to obtain the transform-limited duration of the localized PCW.

The dispersion experienced by the localized PCW in an arbitrary media can be evaluated from a simple relation [126]

$$k_{\mathrm{z}}(\omega) = k(\omega)\cos\left(\alpha(\omega)\right), \tag{5.2.1}$$

where $k(\omega) = \dfrac{\omega}{c}n(\omega)$, $n(\omega)$ is the refractive index of the media and $\alpha(\omega)$ defines the angular dispersion of the PCW. Since PCWs are formed through the parametric amplification, the angular dispersion is directly related to the phase-matching condition. In case of perfect phase matching of plane waves, the internal noncollinearity angle between signal and pump can be obtained from [14]

$$\cos(\alpha_{\mathrm{int}}(\omega)) = \frac{k_1^2 + k_3^2 - k_2^2}{2k_1k_3}, \tag{5.2.2}$$

where subscripts 1,2, and 3 indicate the magnitudes of the wave vectors of signal, idler, and pump, respectively. By taking into account the refraction at the exit

interface of the nonlinear crystal we obtain

$$\alpha(\omega) = \arcsin\left(\frac{k_1}{k(\omega)}\sin\left(\alpha_{\mathrm{int}}(\omega)\right)\right). \tag{5.2.3}$$

Finally, the group velocity (GV), group velocity dispersion (GVD) and so forth can be obtained from (5.2.1) in the usual way:

$$u^{-1} = \left.\frac{dk_{\mathrm{z}}}{d\omega}\right|_{\omega_0}, g = \left.\frac{d^2k_{\mathrm{z}}}{d\omega^2}\right|_{\omega_0}, h = \left.\frac{d^3k_{\mathrm{z}}}{d\omega^3}\right|_{\omega_0}, \ldots \tag{5.2.4}$$

Thus, knowing the propagation distance and dispersion orders, the dispersive propagation of the PCW can be taken into account when pre-chirping signal pulse. In case of DKDP[(1)], the values of the dispersion orders for localized PCW, propagating in free space, were:

$$u^{-1} = 3.343\ \mathrm{fs}/\mu\mathrm{m},\ g = -0.003\ \mathrm{fs}^2/\mu\mathrm{m},\ h = 0.044\ \mathrm{fs}^3/\mu\mathrm{m}. \tag{5.2.5}$$

For comparison the corresponding values of the material dispersion of the DKDP crystal were:

$$u^{-1}_{\mathrm{DKDP}} = 5.045\ \mathrm{fs}/\mu\mathrm{m},\ g_{\mathrm{DKDP}} = 0.019\ \mathrm{fs}^2/\mu\mathrm{m},\ h_{\mathrm{DKDP}} = 0.051\ \mathrm{fs}^3/\mu\mathrm{m}. \tag{5.2.6}$$

Lastly, it should be noted that by placing the nonlinear crystal after the lens, the focal length of the lens is prolonged due to the refraction at the entrance and exit interfaces of the nonlinear crystal. The distance from the exit plane of the nonlinear crystal to the actual position of the focal plane of the lens can be obtained from a simple considerations of geometrical optics. Knowing the internal α_{int} and external α noncollinearity angles, this distance can be calculated for the particular wavelength by the following formula

$$d_2 = f - d_1 - L\tan(\alpha_{\mathrm{int}})\cot(\alpha), \tag{5.2.7}$$

where f is the focal length of the lens, d_1 is the distance from the lens to the entrance plane of the nonlinear crystal, and L is the length of the nonlinear crystal.

In addition it is important to note, that refraction at the interfaces of the non-

linear crystal also introduces a non-negligible aberrations to the pulsed Gaussian signal beam. These aberrations are caused by the wide angular spectrum of the signal beam. Due to these aberrations, the initial Gaussian pulse is no longer transform-limited at the focus, yet the FWHM duration and the diameter are very close to the transform-limited ones. However, the peak intensity at the focus is reduced by 10-15 % in comparison to the case when nonlinear crystal is removed from the scheme. Nevertheless, the width of the angular spectrum of the formed PCW is much narrower than that of the initial Gaussian beam (see Fig. 5.2a). Therefore, the influence of the refraction-related aberrations on the peak intensity of the localized PCW is negligible.

5.3 Numerical experiments

In this section we present a detailed numerical study of the method presented above (Fig. 4.1). The numerical experiments were performed for the case of Type I (oo-e) interaction in DKDP crystal using the split-step method. Similarly as in Sect. 4.3, the linear step was handled in the Fourier domain in accordance with Eq. (2.1.22), thus taking into account full material dispersion and beam non-paraxiality:

$$A_j(t,r,z) = \mathscr{F}^{-1}_{\Omega,k_\perp}\left\{\mathscr{F}_{t,r}\left\{A_j(t,r)\right\}\exp\left(-i\sqrt{k(\omega)^2-k_\perp^2}\,z\right)\right\}, \qquad (5.3.1)$$

where $r=\sqrt{x^2+y^2}$, $k_\perp=\sqrt{k_x^2+k_y^2}$, j=1,2, and 3 indicate signal, idler, and pump, respectively, $k(\omega)=\dfrac{\omega}{c}n(\omega)$ is the magnitude of the wave vector, $n(\omega)$ the refractive index, and $\mathscr{F}$ denotes the Fourier transformation. Actually, the transformation in the spatial domain was performed using quasi-discrete Hankel transform [127, 128]. For the nonlinear step, the coupled three-wave equations (4.3.2) were solved in the near field representation (t,r,z) using fourth-order Runge–Kutta method.

In numerical experiment it was also accounted for self-focusing and cross-

focusing as well as self-phase and cross-phase modulation, due to third order nonlinearity of the DKDP material. The intensity dependent spatio-temporal phase modulation was accounted in each step using Eq. (4.3.3). The nonlinear refractive index was taken to be $n_2 = 5 \times 10^{-16}$ cm^2/W for the pump, and $n_2 = 3 \times 10^{-16}$ cm^2/W for the signal and idler [108]. However, the modification of the presented results due to Kerr effect was found insignificant.

The coefficients of Sellmeier equations for 96 % deuterated DKDP were taken from [129], and the effective second order nonlinear susceptibility was taken to be $\chi^{(2)}_{\text{eff}} = 0.4$ pm/V. The center wavelengths of pump and signal were 532 nm and 950 nm, respectively. The phase-matching angle was taken to be $\theta = 40$ deg, which resulted in external noncollinearity angle of 4.2 deg at 950 nm. This phase-matching angle and the wavelengths of pump and signal assured sufficiently small GVD for the localized PCW (Eq. (5.2.5)), thus a long Bessel-zone could be obtained. Absorption in the DKDP crystal as well as Fresnel reflection losses at the interfaces were not taken into account.

The bandwidth of the signal pulse corresponded to 10 fs (FWHM) transform-limited Gaussian pulse, but signal pulse was pre-chirped before the lens in order to obtain transform-limited duration of the localized PCW. Consequently, the temporal profile of the signal pulse was not Gaussian due to presence of third and higher dispersion orders in the spectral phase. The focal length of the lens was 60 mm and the diameter of the collimated Gaussian signal beam in front of the lens was 5 mm (FWHM). Accordingly, when there was no parametric amplification, the beam diameter at the focal plane of the lens was 5 μm (FWHM).

As it is common in OPCPA there is a trade-off between the amplified signal bandwidth and pump-to-signal conversion efficiency. However, in this paper we focus on disclosing the features related to formation of PCWs. Therefore, for the proof-of-principle numerical experiment, we took pump pulse with nearly rectangular spatio-temporal profile and fully overlapping with the whole signal pulse. The duration of the pump pulse was 2.4 ps, and the beam diameter was 15.5 mm.

Obviously, more reasonable dimensions of the pump pulse could be adopted in order to obtain greater pump-to-signal conversion efficiency. The shape of the amplified signal pulse suggests that for greater conversion efficiencies the ring-shaped pump beam should be employed. Such pump beam could be obtained using either a pair of the axicons [130] or a lens-axicon doublet [131, 132] or a W-shaped axicon mirror [133]. In the former cases, the diameter of the produced ring could be adjusted by changing the distance between the axicons.

When considering the optimum duration and diameter of the pump, the temporal as well as spatial walk-off effects between signal and pump, and also temporal as well as spatial chirps in the far field of the PCW should be taken into account. We also note that birefringent walk-off effect of extraordinary polarized pump will introduce some asymmetry in the far field of the PCW. It should be more pronounced if the diameter of the pump beam is optimized. However, we assume that this effect is not significant in the current setup.

In the following we demonstrate that saturation of parametric amplification can be achieved with relatively low intensities of the signal pulse and without tangible loss of signal bandwidth during the amplification. Of course, for the weaker signal the longer the nonlinear crystal is required in order to achieve the saturation. However, it is not a problem, since the parametric bandwidth, namely, phase-matched bandwidth, is practically unlimited in this scheme. Therefore energy gain factors in access of 10^7 have been reached without any loss of signal bandwidth. The large gain factor is vital, at least in the first amplification stage, in order to suppress remainders of the original Gaussian pulse.

We have found that in case of longer nonlinear crystal, localized PCWs with the longer Bessel-zone can be formed. In the current setup the length of the nonlinear crystal is limited only by the process of back-conversion starting when saturation of parametric amplification is reached. Therefore, by reducing signal or pump intensity one can increase the length of the nonlinear crystal and thus achieve a longer Bessel-zone. As it is explained in the following, this is related to

the acceptance angle of the nonlinear crystal. Therefore, nonlinear crystals that have a small acceptance angle are preferable in formation of the PCWs with the prolonged Bessel-zone.

In order to demonstrate these findings and the performance of the PCWPA in general, numerical experiments were performed for three different cases with different peak intensities of signal and pump pulses. In every case the pump-to-signal conversion efficiency was kept the same by adjusting the length of the nonlinear crystal. The three different cases are labeled as DKDP$^{(1)}$, DKDP$^{(2)}$, and DKDP$^{(3)}$ and referring to the following variation of initial conditions: (a) DKDP$^{(1)}$: $E_\mathrm{s} = 30$ nJ, $I_\mathrm{p} = 50$ GW/cm^2, $L = 23$ mm; (b) DKDP$^{(2)}$: $E_\mathrm{s} = 30$ pJ, $I_\mathrm{p} = 50$ GW/cm^2, $L = 31.8$ mm; (c) DKDP$^{(3)}$: $E_\mathrm{s} = 30$ nJ, $I_\mathrm{p} = 25$ GW/cm^2, $L = 31.6$ mm, where E_s denotes the energy of the signal pulse, I_p denotes the peak intensity of the pump pulses, and L is the length of the DKDP crystal.

For the DKDP$^{(1)}$ case the characteristic spatio-temporal profiles of the signal pulse are depicted in Fig. 5.2. For the other two cases these profiles were visually very similar. As can bee seen from the amplified temporal spectrum (Fig. 5.4a, red line), there was no loss of signal bandwidth. Moreover, for the given initial conditions, it became 15-25 % wider due to saturation of parametric amplification. Energy gain factors of the signal pulse were 5×10^4, 5×10^7 and 2.5×10^4 in case of DKDP$^{(1)}$, DKDP$^{(2)}$ and DKDP$^{(3)}$, respectively.

For the fixed pump intensity the output energy of the PCW is limited by the saturation of parametric amplification, and in those three cases it was 1.54 mJ, 1.52 mJ and 0.77 mJ, respectively. However, note that higher output energies could be achieved by re-scaling of the setup.

The evolution of the peak intensity of the localized PCW during propagation in the Bessel-zone is depicted in Fig. 5.5a. The lengths of the Bessel-zone, measured as FWHM, were 11.5 mm, 13 mm, and 15 mm in DKDP$^{(1)}$, DKDP$^{(2)}$, and DKDP$^{(3)}$ cases, respectively, and the peak values of the peak intensity at the Bessel-zone were accordingly 7.6 PW/cm^2, 6.2 PW/cm^2 and 2.7 PW/cm^2. Recall

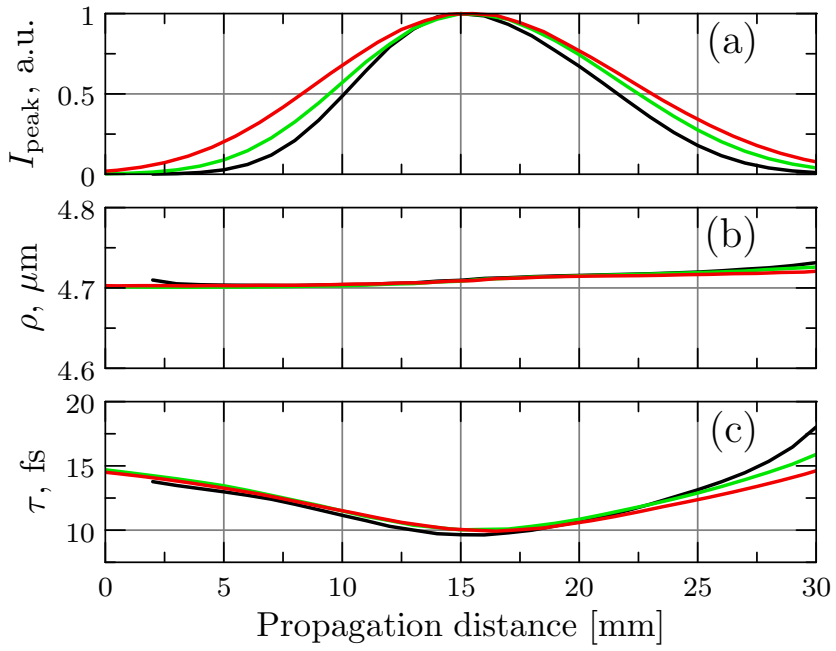

Figure 5.5: (a) Normalized peak intensity, (b) beam diameter (FWHM) and (c) pulse duration (FWHM) of the localized PCW as a function of propagation distance at the Bessel-zone. In all the three graphs black line corresponds to DKDP$^{(1)}$ case, green line to DKDP$^{(2)}$ case and red line to DKDP$^{(3)}$ case. The zero corresponds to the 44 mm, 45 mm and 44.5 mm distance from the exit plane of the nonlinear crystal, respectively.

that in case of Bessel–Gaussian beam the length of the Bessel-zone is longer for narrower angular spectrum of the beam, which in our case is determined by the acceptance angle of the nonlinear crystal. On the other hand, the peak intensity of the diffraction limited Gaussian beam is higher for wider angular spectrum of the beam. That explains the tendency of the obtained values of the peak intensities and the Bessel-zone lengths, since the acceptance angle is smaller for longer nonlinear crystals or for lower pump intensities. Note that it is possible to enlarge the acceptance angle to some extend, using pump beam with a broad angular spectrum [134].

Fig. 5.5b shows the corresponding evolution of the beam diameter of the localized PCW. As expected, beam diameter keeps nearly constant value of 4.7 μm (FWHM) in entire Bessel-zone, which in DKDP$^{(1)}$ case is 2 orders longer than Rayleigh length (53 μm) of Gaussian beam of the same waist. Since the diameter of Bessel-beam is defined by intersection angle, even smaller beam diameters and higher peak intensities could be obtained at the Bessel-zone by increase of the

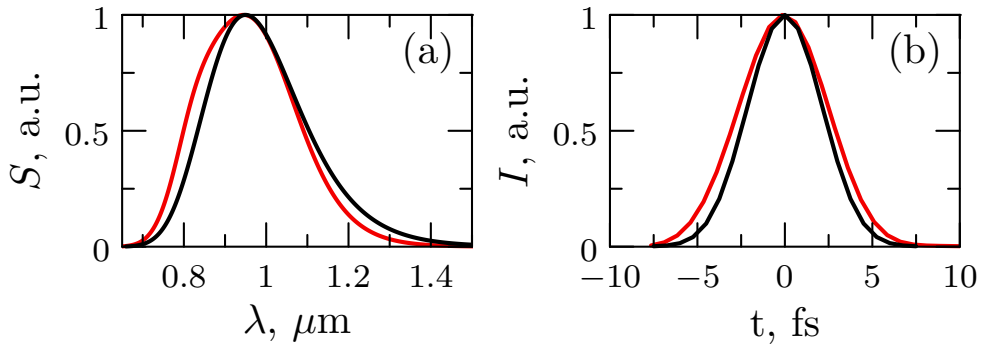

Figure 5.6: (a) Spectral power of the amplified signal pulse (red line); black line depicts initial spectrum of the Gaussian signal pulse. (b) On-axis temporal profile of the amplified signal pulse at the center of the Bessel-zone (red line); black dashed line depicts its Fourier transform-limited profile. All graphs are normalized.

noncollinearity angle.

As can bee seen from Fig. 5.5c, the localized PCW has nearly transform-limited duration ($\approx$ 9.5 fs) around the center of the Bessel-zone. However, due to dispersive propagation in free space the duration of this localized PCW varies. The point in the Bessel-zone, at which the minimal duration is obtained, can be adjusted by concerted pre-chirping of the signal pulse before the lens. In addition, by controlling the position of the point in the Bessel-zone, at which the minimal duration is obtained, it is possible to modify the evolution of the peak intensity of the localized PCW during propagation in the Bessel-zone. This might be beneficial in some experiments, where asymmetric evolution of the peak intensity with respect to the center of the Bessel-zone is required.

In addition, numerical experiments were performed for the signal pulse of bandwidth corresponding to 5 fs transform-limited Gaussian pulse. The obtained results revealed that there were no loss of signal bandwidth (Fig. 5.6a). However, noncollinear interaction introduces non-negligible spatial walk-off between signal and idler beams, resulting in chromatic aberration that prevents transform-limited duration at the Bessel-zone. With the initial parameters as in DKDP$^{(1)}$, the minimal duration of the localized PCW was 6 fs, and the temporal profile was still nearly Gaussian (Fig. 5.6b, read line) with the peak intensity of 14.4 PW/cm^2.

Note that DKDP crystal was chosen only for demonstrational purposes, and

the method presented in this study is suitable for other nonlinear crystals as well as for other wavelengths of interacting waves.

In the next section we demonstrate, that the same scheme and ideas could be adopted for parametric amplification of PCWs by means of four-wave-mixing (FWM) in isotropic materials. Thus, offering the possibility for obtaining ultrashort PCWs in the ultraviolet.

5.4 PCWPA by means of four-wave-mixing in isotropic materials

Since FWM has been demonstrated as an attractive way for generation of ultrashort pulses in the ultraviolet [135, 136, 137, 138, 139], we carried out a series of numerical experiments for PCWPA in a medium with Kerr nonlinearity. We have investigated the parametric amplification via FWM in fused silica (FS), using unidirectional pulse propagation equation (Eq. (2.1.21)). The Kerr nonlinearity was accounted for in the Fourier domain, thus taking into account self-phase modulation, self-focusing, self-steepening, cross-phase modulation, cross-focusing, and of course, parametric amplification via FWM. Yet the other relevant effects such as third harmonic generation, multi-photon absorption and modulation instability were omitted for simplicity.

The center wavelengths of signal and pump were 395 nm and 527 nm, respectively. Such wavelengths guarantied sufficiently small GVD during propagation in free space of the localized PCW. The values of the dispersion orders, calculated according to Eq. (5.2.4), were:

$$u^{-1} = 3.275 \text{ fs}/\mu\text{m},\ g = 0.00055 \text{ fs}^2/\mu\text{m},\ h = 0.085 \text{ fs}^3/\mu\text{m}. \tag{5.4.1}$$

However, just a small scale setup could be handled in a reasonable calculation time due to requirements of small spatial and temporal discretization. Thus, the focal length of the lens was 15 mm and the diameter of the collimated Gaussian signal beam in front of the lens was 1.25 mm (FWHM). Accordingly, when there

was no parametric amplification, the beam diameter at the focal plane of the lens was 2 μm (FWHM). The length of the fused silica was 14.5 mm and the distance in free space from the exit plane of fused silica to the center of the Bessel-zone was 21.2 mm. The external noncollinearity angle was 4.4 deg at 395 nm. The non-linear refractive index at 527 nm was taken to be $n_2 = 2.2 \times 10^{-16}$ cm^2/W [140]. The temporal profile of the pump was Gaussian with the peak intensity of 300 GW/cm^2 and 2 ps duration (FWHM). The spatial profile of the pump was super-Gaussian of 15-th order and it was ring-shaped (Fig. 5.7b, dimmed and dotted). The diameter of the ring-shaped pump was 2.5 mm (FWHM) and the radius of the ring was 1.6 mm. The bandwidth of the signal pulse corresponded to 10 fs (FWHM) transform-limited Gaussian pulse, but signal pulse was pre-chirped before the lens in order to obtain transform-limited duration of the localized PCW.

Fig. 5.7 depicts intensity profiles of the signal pulse in distinctive space and time domains. Similarly as in $\chi^{(2)}$ case, the angular spectrum and the far field of the amplified signal pulse were ring-shaped (Fig. 5.7a,b vivid). However, the resulted spatio-temporal profile of the localized PCW was X-shaped (Fig. 5.7d), as determined by its angular dispersion (Fig. 5.7a, vivid), which in turn was defined by the phase-matching condition in FS.

The iso-intensity profiles of the formed PCW at the exit plane of FS and at the center of the Bessel-zone are depicted in Fig. 5.8. These profiles were obtained from corresponding intensity profiles of Fig. 5.7b and Fig. 5.7d.

The energy gain factor of 1.41×10^5 was obtained with the input signal energy of 2 nJ. However, the pump-to-signal conversion efficiency was just 0.18 %. In contrast to $\chi^{(2)}$ case, a deep depletion of the pump pulse could not be achieved due to self- and cross-phase modulation encountered by the interacting waves. Thus, the length of the FS was primarily limited by the phase modulation and not by the saturation of parametric amplification.

In the current setup the initial bandwidth of the signal pulse could not be preserved during the amplification (Fig. 5.9a, red line). The spectral narrowing

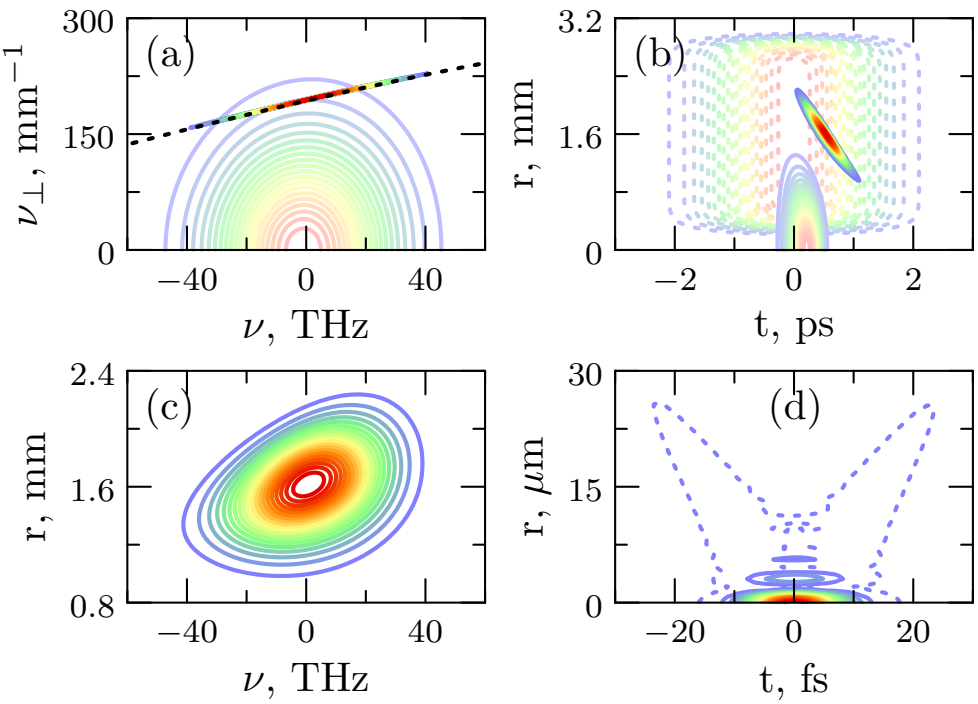

Figure 5.7: (a) Spatio-temporal spectrum of the signal pulse before (dimmed) and after (vivid) amplification in FS; phase-matching curve is depicted by black dotted line; $\nu_\perp$ denotes the spatial frequency $\nu_\perp = k_\perp/2\pi$, and ν denotes the temporal one $\nu = \Omega/2\pi$. (b) Spatio-temporal profile of the signal pulse before (dimmed) and after (vivid) amplification in FS; the spatio-temporal profile of the pump pulse is depicted by dimmed and dotted line. (c) Spatio-spectral intensity distribution of the amplified signal pulse. (d) Spatio-temporal profile of the amplified signal pulse at the center of the Bessel-zone; the dotted blue contour corresponds to iso-intensity line at 0.005 level of the peak intensity. All graphs are normalized.

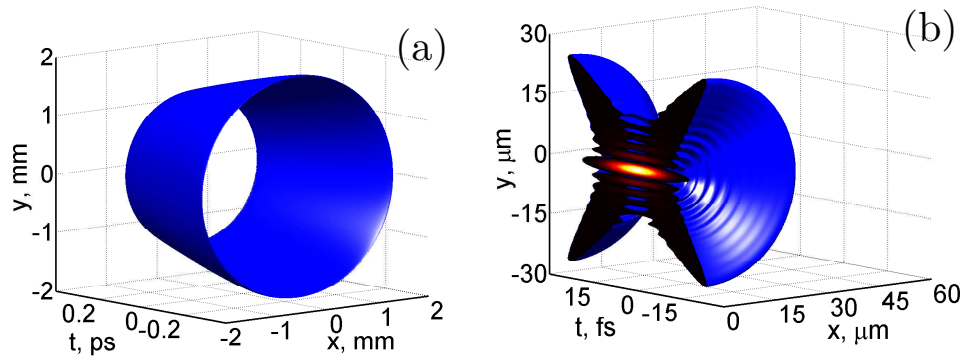

Figure 5.8: Iso-intensity profile of the formed PCW at the exit plane of the FS (a) and at the center of the Bessel-zone (b). Iso-intensity profiles are depicted at 0.5 and 0.005 levels of the peak intensity, respectively. The iso-intensity profile in (b) is cut-in-half for better visual experience. Note that the scales in (a) and (b) are different.

was caused by the Gaussian temporal profile of the pump pulse (Fig. 5.7b, dimmed and dotted) and the presence of spatial (Fig. 5.7c) and temporal chirps in the far field of the PCW. Yet the on-axis temporal profile at the center of the Bessel-zone was close to its transform-limited profile (Fig. 5.9b, red line).

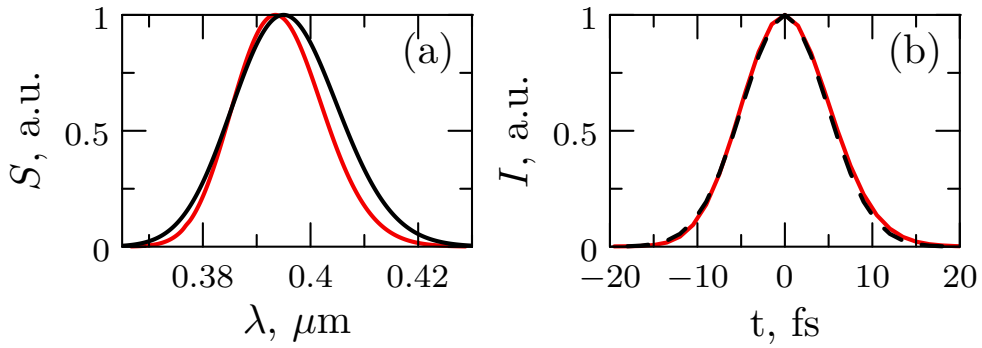

Figure 5.9: (a) Spectral power of the amplified signal pulse (red line); black line depicts initial spectrum of the Gaussian signal pulse. (b) On-axis temporal profile of the amplified signal pulse at the center of the Bessel-zone (red line); black line depicts its Fourier transform-limited profile. All graphs are normalized.

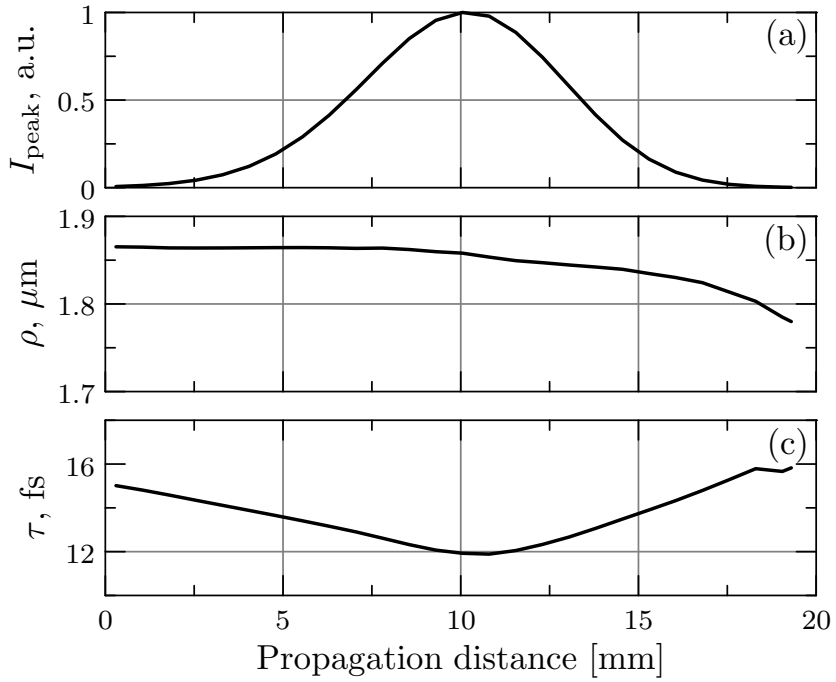

Figure 5.10: (a) Normalized peak intensity, (b) beam diameter (FWHM) and (c) pulse duration (FWHM) of the localized PCW as a function of propagation distance at the Bessel-zone. The zero corresponds to the 11.2 mm distance from the exit plane of FS.

The length of the obtained Bessel-zone was 6.7 mm (Fig. 5.10a) and the peak value of the peak intensity of the localized PCW was 4.7 PW/cm^2. The beam diameter of 1.85 μm (FWHM) was nearly constant in entire Bessel-zone (Fig. 5.10b) and the duration of 12 fs (FWHM) was near-transform-limited (11.5 fs) around the center of the Bessel-zone (Fig. 5.10c). Thereby it is demonstrated that PCWPA is a feasible tool for formation of ultrashort PCWs in the ultraviolet by means of FWM.

In the next section the underlying idea of the PCWPA method is explained in a greater detail by disclosing some features of the linear propagation of PCWs.

5.5 Linear propagation of pulsed conical waves

Using PCWPA method presented in Sect. 5.1 it is possible to transform Gaussian-shaped pulse into the far field of arbitrary PCW, determined by the phase-matching condition in the nonlinear material. The actual shape and linear propagation features of the PCW essentially depend on the acquired angular dispersion. However, not all the angular dispersions that can be imposed by the parametric amplification will work equally well. Therefore, in this section some properties of the formed PCW are discussed in a greater detail. There are two essential things that we have to consider: first, the dispersive propagation in the Bessel-zone, and second, the dependence of the far-field spatio-temporal profile on the angular dispersion.

Due to presence of the angular dispersion, the duration of the PCW varies during propagation in free space (Fig. 5.5c). In general, light pulses possessing angular dispersion will experience the dispersion, which is different from the dispersion of the media [141, 142, 143, 144, 123]. Once the function of the angular dispersion $\alpha(\omega)$ is known, the experienced dispersion along the chosen direction z' can be evaluated from a simple relation [126]

$$k_{z'}(\omega) = k(\omega)\cos\left(\alpha(\omega)\right), \tag{5.5.1}$$

where α is the angle of the angular component relative to the chosen direction z′ (Fig. 5.11), and $k(\omega) = \dfrac{\omega}{c}n(\omega)$, here $n(\omega)$ is the refractive index of the media. The group velocity (GV), group velocity dispersion (GVD) and so forth can be obtained from Eq. (5.5.1) in the usual way:

$$u^{-1} = \left.\frac{dk_{z'}}{d\omega}\right|_{\omega_0}, g = \left.\frac{d^2k_{z'}}{d\omega^2}\right|_{\omega_0}, h = \left.\frac{d^3k_{z'}}{d\omega^3}\right|_{\omega_0}, \ldots \tag{5.5.2}$$

Due to the presence of GVD or higher dispersion orders, the pulse duration

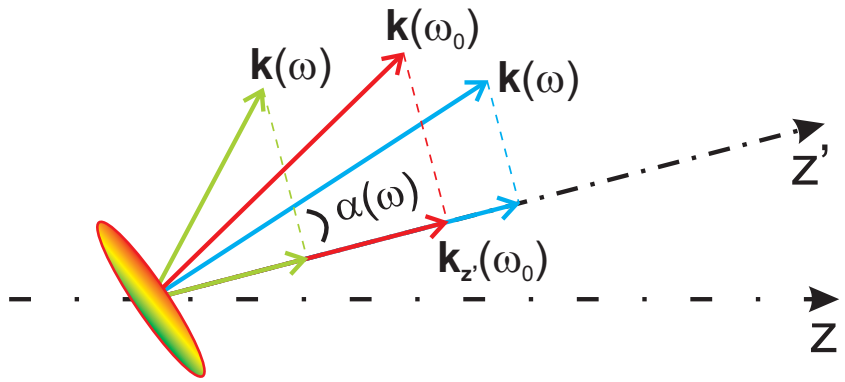

Figure 5.11: Schematic representation of the pulse possessing angular dispersion. α is the angle between the wave vector of particular frequency and the chosen direction of reference z', whereas z axis implies the actual propagation direction of the pulse.

and shape varies during the propagation. In case when third and higher dispersion orders are negligible, the FWHM duration of the initially transform-limited Gaussian pulse can be calculated using the following formula

$$\tau = \tau_{\mathrm{TL}} \sqrt{1 + \left(4\ln(2)\frac{g}{\tau_{\mathrm{TL}}^2} d\right)^2}, \tag{5.5.3}$$

where τ_{TL} is the transform-limited duration (FWHM) and d is the propagation distance. However note, that this equation is valid only in the case when the pulse has non-negligible spatial chirp.

Before the specific analysis of the PCWs, we present some general features of linear propagation in free space of pulses that posses angular dispersion. Assuming that $n(\omega) = 1$, from Eq. (5.5.2) we can obtain an explicit expressions:

$$u^{-1} = \frac{1}{c}\left[\cos\alpha_0 - \alpha_1\omega_0 \sin\alpha_0\right], \tag{5.5.4}$$

$$g = -\frac{1}{c}\left[\alpha_1^2\omega_0\cos\alpha_0 + (2\alpha_1 + \alpha_2\omega_0)\sin\alpha_0\right], \tag{5.5.5}$$

$$h = -\frac{1}{c}\left[3\left(\alpha_1^2 + \alpha_1\alpha_2\omega_0\right)\cos\alpha_0 + \left(-\alpha_1^3\omega_0 + 3\alpha_2 + \alpha_3\omega_0\right)\sin\alpha_0\right], \tag{5.5.6}$$

where $\alpha_0 = \alpha(\omega_0)$, $\alpha_1 = \left.\frac{d\alpha}{d\omega}\right|_{\omega_0}$, $\alpha_2 = \left.\frac{d^2\alpha}{d\omega^2}\right|_{\omega_0}$, $\alpha_3 = \left.\frac{d^3\alpha}{d\omega^3}\right|_{\omega_0}$.

As can bee seen from Eq. (5.5.4), the GV of the pulse, possessing angular dispersion, may have values from positive to negative infinity [145]. Interestingly, but this feature is not widely recognized. Yet it should be noted, that it depends on the chosen direction z′, i.e. on the direction of reference. When propagation

direction of the angular component with the central frequency ω_0 is taken as a reference, then $\alpha_0 = 0$ and the GV becomes equal to the speed of light in vacuum, and is independent from the angular dispersion. Note that in this analysis, the central frequency ω_0 is a free parameter and is defined just by the frequency, which is chosen when evaluating the derivatives in Eq. (5.5.2). In most of the practical cases, the chosen frequency coincides with the central frequency of the pulse being considered. In such case, the propagation direction of the central angular component usually coincides with the direction of the energy flow.

As can be seen from Eq. (5.5.5), depending upon the function of the angular dispersion, the GVD may have arbitrary values as well. However, in the particular case when we choose the propagation direction of the central angular component as a reference, then $\alpha_0 = 0$ and the sign of the GVD is *always* negative. Therefore, during propagation in free space light pulses possessing angular dispersion will always experience the anomalous dispersion in the propagation direction of the central angular component. This is an important feature that empowers to build pulse compressors, based on gratings and prisms [90, 91]. Do not be confused with the positive GVD value of the PCW given in the previous section (Eq. (5.4.1)), since in that case $\alpha_0 \neq 0$, as is explained below.

In the following we are interested in the dispersive propagation of PCWs along the z axis (Fig. 5.1), therefore $\alpha_0 \neq 0$. Neglecting the fact, that the direction of the energy flow is different, we chose z axis as a direction of reference, since it is the actual direction of propagation of the localized PCW at the Bessel-zone.

In order to analyze the dispersion experienced by the localized PCW in free space we need to obtain the function of the angular dispersion $\alpha(\omega)$. Recall, that pump pulse is capable to amplify only those angular components that lay in the vicinity of the phase-matching curve (Fig. 5.2a, vivid). Therefore the angular dispersion $\alpha(\omega)$ of the PCW, obtained by means of PCWPA, is directly related to the phase-matching condition. For the case of perfect phase matching, the internal noncollinearity angle $\alpha_{\text{int}}(\omega)$ can be obtained from Eq. (5.2.2). Yet we have to

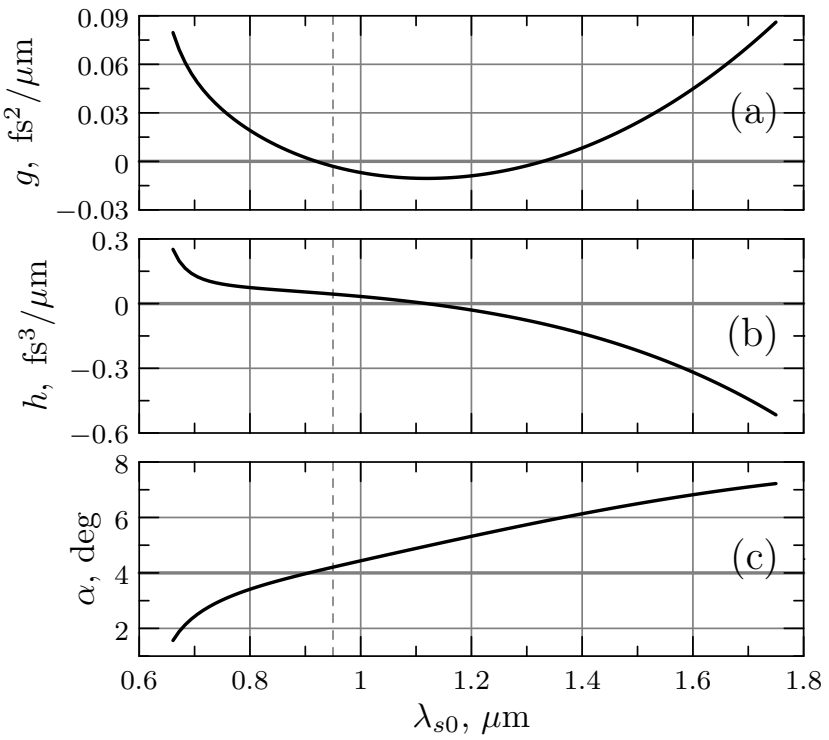

Figure 5.12: GVD (a) and third dispersion order (b) for the localized PCW during propagation in free space as a function of the central signal wavelength. The external noncollinearity angle α is depicted in (c). The graphs were obtained for the DKDP crystal pumped by 532 nm at the phase-matching angle 40 deg. The vertical dashed gray line marks the central wavelength of the signal, investigated in Sect. 5.1. It should be noted, that g and h dependence on the phase-matching angle was insignificant.

take into account the refraction at the exit interface of the nonlinear crystal, and finally we obtain

$$\alpha(\omega) = \arcsin\left[n_1(\omega)\sin\left(\alpha_{\text{int}}(\omega)\right)\right], \tag{5.5.7}$$

where $n_1(\omega)$ is the refraction index for the signal wave in the nonlinear material.

By substituting Eq. (5.5.7) into Eq. (5.5.2) we could obtain expression for each dispersion order. However, the obtained expressions would be rather lengthy, and therefore are not presented here. The free parameters in those expression are: the central frequencies of signal and pump, the phase-matching angle and the material dispersion of the nonlinear crystal. By changing these parameters a wide variety of values of the dispersion orders can be obtained. There are no restrictions for the value and sign of any dispersion order in general, thus it is possible to find adequate dispersion orders that match the particular goals.

For the particular case presented in section 5.1, the dependences of second

and third dispersion orders are depicted in Fig. 5.12. In that case, the goal was to obtain as small GVD as possible, and a small third dispersion order as well, in order to have a long Bessel-zone. We have looked up some other nonlinear crystals, yet DKDP crystal seemed to match the best our preferred parameters: pump wavelength around 530 nm, external noncollinearity angle around 4 deg, central signal wavelength in the visible or near-infrared.

On the other hand, the goal could be absolutely opposite, in case it is aimed to have a tight temporal focus of the localized PCW. Naturally, this would result in a shorter Bessel-zone, but also it may lead to the substantial increase of the PCW duration in the far field. Therefore, it could be preferable over quasi-steady duration of the localized PCW at the Bessel-zone, due to advantages from the CPA point of view (energy boosting). In addition, a tight temporal focus seems to be advantageous in many applications of light-matter interaction, including high-order harmonic generation, as was referenced in the introduction of Sect. 3.3.

However, the duration of the PCW in the far field is hardly predicted knowing just a GVD, since Eq. (5.5.3) is not applicable due to the presence of the spatial chirp (Fig. 5.2c). Recall that the spatial chirp may yield shorter as well as longer pulse duration (Eq. (3.3.3)), depending on the temporal chirp of the pulse, which actually is a function of GVD and the propagation distance. In addition, due to the presence of the spatial chirp, the beam diameter will also contribute to the duration of the far field. Nevertheless, there are some works in which pulse broadening accompanied by the spatial chirp is treated analytically, however, with the assumption of linear angular dispersion and narrow bandwidth of the pulse [70, 69]. Thus, analytical approach is applicable just for particular cases and, in general, is not suitable for the case under consideration, since we are interested in ultra-broadband pulses and the angular dispersion is defined by the phase-matching curve, which may take arbitrary shapes. Therefore, the best way to estimate the spatio-temporal profile of the PCW in the far field is by numerical simulation of linear propagation of the localized PCW.

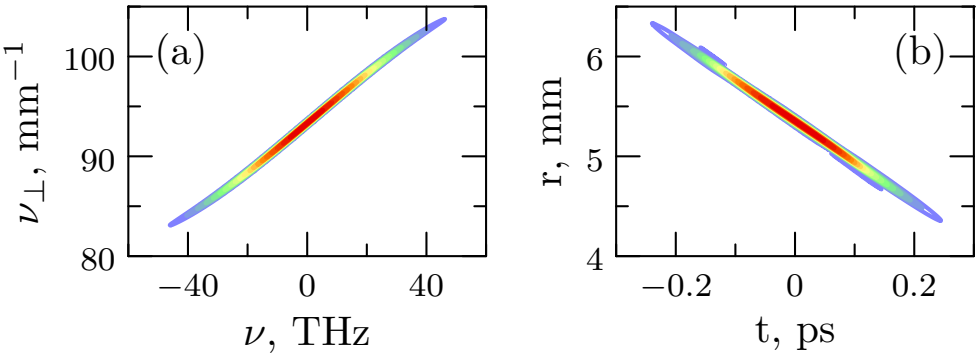

Figure 5.13: Spatio-temporal spectrum of the PCW (a) and corresponding spatio-temporal profile of the far field (b). $\nu_\perp$ denotes the spatial frequency $\nu_\perp = k_\perp/2\pi$, and ν denotes the temporal one $\nu = \Omega/2\pi$. All graphs are normalized. The far field of the PCW was obtained by back-propagating the transform-limited and localized PCW in free space for 60 mm. The bandwidth of the PCW corresponded to 10 fs transform-limited Gaussian-pulse duration (FWHM). The angular dispersion was applied artificially, assuming the parametric amplification of the signal pulse with 800 nm central wavelength in BBO nonlinear crystal, pumped by 515 nm at the phase-matching angle 24.545 deg, which corresponds to the "magic" phase-matching angle. The FWHM duration of the PCW in the far field is 14.6 fs.

The angular dispersion originating in the PCWPA due to noncollinear interaction geometry could be separated into three general groups: first, when $\alpha(\omega)$ is nearly constant, i.e. when $\alpha(\omega) \approx \alpha_0$, thus there is no angular dispersion actually; second, when $k_\perp(\omega) = k(\omega)\sin(\alpha(\omega)) = \text{const.}$, i.e. the angular dispersion corresponds to the definition of the pulsed Bessel beam [146]; third, when the function of the angular dispersion is arbitrary and cannot be described by the definitions of the first two groups.

The first group is well exploited in ultra-broadband noncollinear parametric amplifiers (NOPAs) based on BBO nonlinear crystals [1, 125]. It could be of particular interest for PCWPA as well, since $\alpha(\omega) = \text{const.}$ would yield zero GVD and zero higher dispersion orders (see Eqs. (5.5.5)–(5.5.6)) for the localized PCW during propagation in free space. However, due to such angular dispersion, nearly transform limited pulse duration is preserved in the far field of PCW as well (Fig. 5.13). Therefore, parametric amplification of ultrashort light pulses by means of PCWPA would not be practical in this case.

Angular dispersion of the second group ($k_\perp(\omega) = \text{const.}$), unlike any other type of angular dispersion, has visually no effect on the spatio-temporal profile

of the Gaussian pulse. The localized PCW with such angular dispersion is called pulsed Bessel–Gaussian beam (PBGB) and corresponds to a special case of PCWs. Note that localized PCW with nearly $k_\perp(\omega) = \text{const.}$ was formed in the PCWPA presented previously (Fig. 5.2d). Nevertheless, it is possible to find nonlinear crystals and wavelengths of pump and signal, that would match this condition more strictly for the broadband signal pulse. Commonly, the broadest parametric bandwidths with $k_\perp(\omega) \approx \text{const.}$ are obtained in case of noncollinear degenerate parametric interaction, for instance: DKDP crystal, $\theta = 39.5$ deg, $\lambda_\text{p} = 515$ nm, $\lambda_\text{s} = 1030$ nm.

Since in case of PBGB the angular dispersion is defined just by one number, the dispersion orders for the PBGB propagating in free space can be estimated in advance without specifying neither nonlinear crystal nor pump wavelength. The function of the angular dispersion is obtained simply from the following formula

$$\alpha(\omega) = \arcsin\left(\frac{k_\perp}{\omega}c\right). \tag{5.5.8}$$

After substituting Eq. (5.5.8) into Eq. (5.5.2), the first three dispersion orders were evaluated for two specific central frequencies and depicted as a functions of $k_\perp$ in Fig. 5.14. For indication, the angle of the central angular component with respect to the z axis is provided in Fig. 5.14d. Recall, that in case of PCWPA, this angle is related to the external noncollinearity angle between signal and pump. Therefore, in the practical setups, α_0 should not be greater than 10 deg, in order to avoid problems related to the spatial walk-off between the interacting beams during the parametric amplification.

From Fig. 5.14a we can observe the general feature of the PBGB, namely, the group velocity of the PBGB in free space is always smaller than the speed of light in vacuum c. Furthermore, as it can be seen from Figs. 5.14b and 5.14c, the PBGB with the shorter central wavelength would experience the smaller GVD during propagation in free space. Therefore, in case when quasi-steady duration is desired during propagation at the Bessel-zone, the PBGB with the shorter

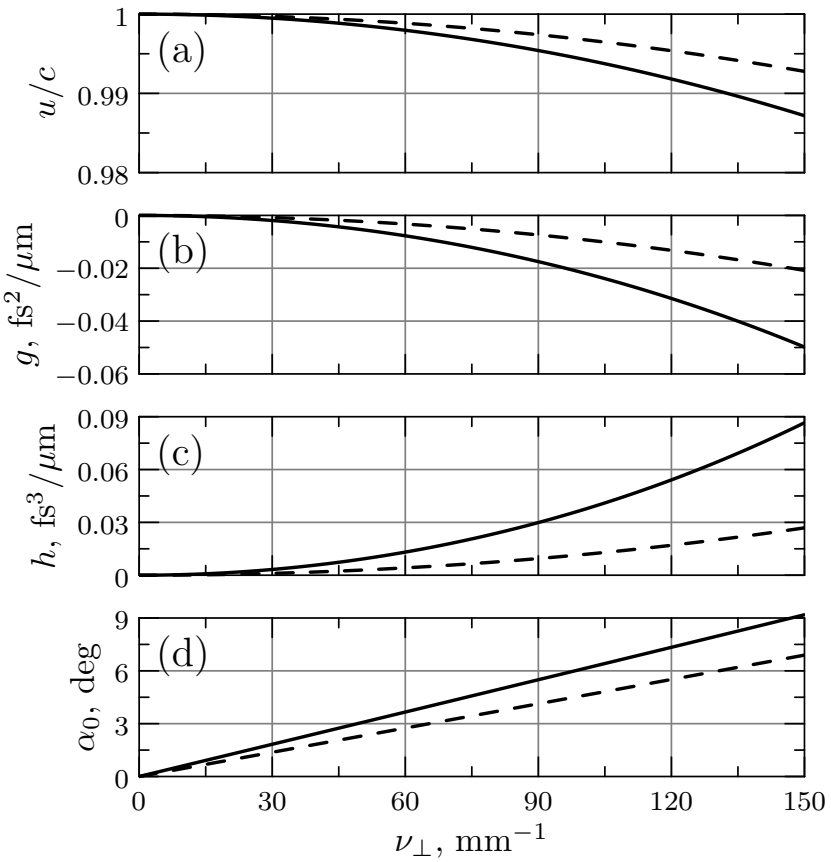

Figure 5.14: (a) GV relative to the speed of light in vacuum, (b) GVD and (c) third dispersion order for the pulsed Bessel-Gaussian beam during propagation in free space as a function of the spatial frequency $\nu_\perp = k_\perp/2\pi$. In addition, the dependence of the angle between the central angular component and the z axis is depicted in (d). In each graph, the solid line depicts the dependencies of the pulsed Bessel-Gaussian beam with the central wavelength of 1064 nm, whereas the dashed line - of 800 nm.

central wavelength would be more advantageous. However, numerical experiments of PBGB propagation in free space indicate that the longer central wavelength yields longer duration of the spatio-temporal profile in the far field, thus it would be superior from the CPA point of view (energy boosting).

Lastly, the third group of angular dispersion defined above, posses miscellaneous types of angular dispersion that may yield extraordinary shapes of the spatio-temporal profile in the far field of PCW (Fig. 5.15). Still it is very attractive for PCWPA, since it gives the maximum flexibility on possible signal wavelengths and on obtainable dispersion orders for the localized PCW during propagation in free space or any other medium.

In conclusion, the angular dispersion and the shape of the spatio-temporal

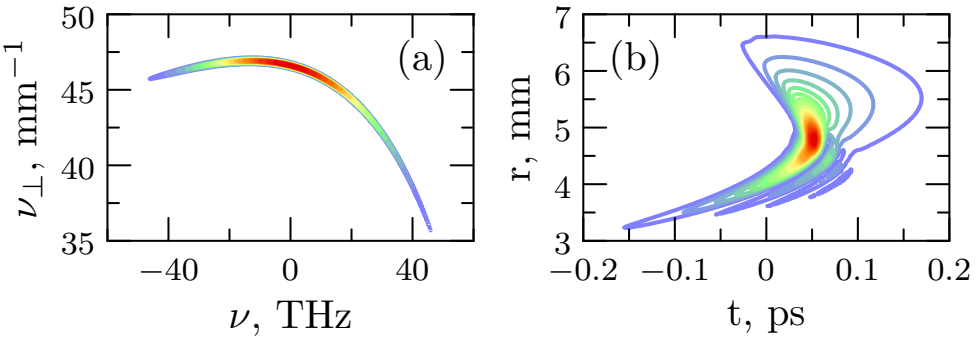

Figure 5.15: Spatio-temporal spectrum of the PCW (a) and corresponding spatio-temporal profile of the far field (b). $\nu_\perp$ denotes the spatial frequency $\nu_\perp = k_\perp/2\pi$, and ν denotes the temporal one $\nu = \Omega/2\pi$. All graphs are normalized. The far field of the PCW was obtained by back-propagating the transform-limited and localized PCW in free space for 150 mm. The bandwidth of the PCW corresponded to 10 fs transform-limited Gaussian-pulse duration (FWHM). The angular dispersion was applied artificially, assuming the parametric amplification of the signal pulse with 750 nm central wavelength in DKDP nonlinear crystal, pumped by 515 nm at the phase-matching angle 38 deg.

profile of the PCW, as well as experienced dispersion during propagation at the Bessel-zone, are essentially determined by the phase-matching condition in the nonlinear material. Therefore, despite the fact that in the previous sections the PCWs were obtained by transformation from the Gaussian-shaped pulses, the spatio-temporal profile and the linear propagation characteristics of the localized PCW can be predicted solely from the phase-matching condition. By varying the phase-matching curves a great variety of angular dispersions can be obtained, thus empowering to adopt the PCWPA for diverse applications.

5.6 Conclusions

In conclusion, we have presented a novel and versatile method for formation and parametric amplification of localized ultra-intense few-cycle PCWs. The method allows to reshape Gaussian wave-packet into PCW and simultaneously achieve a large gain factor by performing parametric amplification in the far field. The achromatic phase matching, exploited in this method, empowers the parametric amplification of bandwidths corresponding to few-cycle light pulses with Gaussian temporal spectrum. Moreover, it enables to select angular dispersion for the PCW corresponding to a particular phase-matching curve, among many possible in the

nonlinear crystal. Thus, a wide family of localized PCWs with peculiar propagation features can be generated. In fact, fine tuning of the angular dispersion is possible, either by adjusting the phase-matching angle or temperature of the nonlinear crystal.

The distance to the point of temporal focus is controlled by pre-chirping of the signal pulse. However, the length of the obtained Bessel-zone is determined by the acceptance angle and the external noncollinearity angle. Thus, cannot be controlled freely. The beam diameter of the localized PCW is also not a free parameter, and is defined by the signal wavelength and the noncollinearity angle.

The presented method renders the main features of the OPCPA technique and, in addition, suggest a substantial simplification as it does not require a pulse compressor. Therefore, it might be considered as a key solution in OPCPA setups, for which the pulse compressor is a bottleneck. Moreover, subsequent amplification stages could be arranged by exploiting the 4-f imagining with the nonlinear crystal placed after the second lens like in Fig. 5.2. Each additional stage could be designed for larger beam diameters, thus enabling for greater pump energies.

Furthermore, this method can be applied for parametric amplification of PCWs by means of four-wave-mixing in materials with Kerr nonlinearity. It has been demonstrated that relatively large energy gain factor, of the order of 10^5, could be achieved with the modest pump intensity of 300 GW/cm^2 and without spontaneous break-up and filamentation of the pump beam in fused silica.

Chapter 6

Conclusions

1. The overall duration of the angularly or spatially dispersed pulsed Gaussian beam does not change during propagation in free space, despite the fact that its spatio-temporal profile is consistently changing. The pulse-front tilt of the angularly or spatially dispersed pulsed Gaussian beam gradually disappears with increasing propagation distance.

2. When the angularly or spatially dispersed pulsed Gaussian beam is focused by the lens, its spatio-temporal profile at the back focal plane of the lens does not dependent on the propagation distance before the lens. However, the spatio-temporal profile is tilted. In case of angularly dispersed pulsed Gaussian beam, the pulse-front tilt depends on the initial parameters of the pulsed beam. Whereas in case of spatially dispersed pulsed Gaussian beam, the pulse-front tilt at the back focal plane of the lens does not depend on the initial parameters of the pulsed beam, and is determined by the acquired angular dispersion only.

3. The spatio-temporal distortions acquired by the signal pulse in noncollinear OPCPA originate due to pulse-front mismatch. The acquired signal pulse tilt is always smaller than the tilt of the pump pulse, and vanishes when the physical length of the pump becomes equal to its diameter.

4. When a strongly chirped signal pulse is being amplified in noncollinear parametric amplifier, it acquires both the spatial chirp and pulse-front tilt, however the angular dispersion is negligible. Conversely, when transform-limited

signal pulse is amplified, it also becomes tilted, but possesses angular dispersion only.

5. The presented PCWPA method is a novel and versatile technique for formation and parametric amplification of localized ultra-intense few-cycle PCWs. It exploits achromatic phase matching and allows to generated a wide family of localized PCWs with peculiar propagation features.

6. The proposed method allows to achieve large energy gain factors, and renders the main features of the OPCPA technique, but does not require a pulse compressor stage. Thus, it might be considered as a key solution in OPCPA setups where the pulse compressor is a bottleneck.

7. This method is suitable for parametric amplification of PCWs by means of four-wave-mixing in materials with Kerr nonlinearity. A relatively large energy gain factor can be achieved with the pump intensity below filamentation threshold.

Bibliography

[1] G. M. Gale, M. Cavallari, T. J. Driscoll, and F. Hache, "Sub-20-fs tunable pulses in the visible from an 82-MHz optical parametric oscillator," Opt. Lett. **20**, 1562–1564 (1995).

[2] D. Strickland and G. Mourou, "Compression of amplified chirped optical pulses," Opt. Commun. **56**, 219–221 (1985).

[3] A. Dubietis, G. Jonušauskas, and A. Piskarskas, "Powerful femtosecond pulse generation by chirped and stretched pulse parametric amplification in BBO crystal," Opt. Commun. **88**, 437–440 (1992).

[4] G. Cerullo, M. Nisoli, S. Stagira, and S. D. Silvestri, "Sub-8-fs pulses from an ultrabroadband optical parametric amplifier in the visible," Opt. Lett. **23**, 1283–1285 (1998).

[5] T. Kobayashi and A. Shirakawa, "Tunable visible and near-infrared pulse generator in a 5 fs regime," Appl. Phys. B **70**, S239–S246 (2000).

[6] A. Baltuška, T. Fuji, and T. Kobayashi, "Visible pulse compression to 4 fs by optical parametric amplification and programmable dispersion control," Opt. Lett. **27**, 306–308 (2002).

[7] S. Witte, R. T. Zinkstok, A. L. Wolf, W. Hogervorst, W. Ubachs, and K. S. E. Eikema, "A source of 2 terawatt, 2.7 cycle laser pulses based on noncollinear optical parametric chirped pulse amplification," Opt. Express **14**, 8168–8177 (2006).

[8] H. Kiriyama, M. Mori, Y. Nakai, Y. Yamamoto, M. Tanoue, A. Akutsu, T. Shimomura, S. Kondo, S. Kanazawa, H. Daido, T. Kimura, and N. Miyanaga, "High-energy, high-contrast, multiterawatt laser pulses by optical parametric chirped-pulse amplification," Opt. Lett. **32**, 2315–2317 (2007).

[9] D. Herrmann, L. Veisz, R. Tautz, F. Tavella, K. Schmid, V. Pervak, and F. Krausz, "Generation of sub-three-cycle, 16 TW light pulses by using noncollinear optical parametric chirped-pulse amplification," Opt. Lett. **34**, 2459–2461 (2009).

[10] P. Wnuk, Y. Stepanenko, and C. Radzewicz, "Multi-terawatt chirped pulse optical parametric amplifier with a time-shear power amplification stage," Opt. Express **17**, 15264–15273 (2009).

[11] S. Adachi, H. Ishii, T. Kanai, N. Ishii, A. Kosuge, and S. Watanabe, "1.5 mJ, 6.4 fs parametric chirped-pulse amplification system at 1 kHz," Opt. Lett. **32**, 2487–2489 (2007).

[12] J. Rothhardt, S. Hädrich, E. Seise, M. Krebs, F. Tavella, A. Willner, S. Düsterer, H. Schlarb, J. Feldhaus, J. Limpert, J. Rossbach, and A. Tünnermann, "High average and peak power few-cycle laser pulses delivered by fiber pumped OPCPA system," Opt. Express **18**, 12719–12726 (2010).

[13] D. N. Schimpf, J. Rothhardt, J. Limpert, A. Tünnermann, and D. C. Hanna, "Theoretical analysis of the gain bandwidth for noncollinear parametric amplification of ultrafast pulses," J. Opt. Soc. Am. B **24**, 2837–2846 (2007).

[14] A. Piskarskas, A. Stabinis, and V. Pyragaitė, "Ultrabroad bandwidth of optical parametric amplifiers," IEEE J. Quantum Electron. **46**, 1031–1038 (2010).

[15] A. Shirakawa and T. Kobayashi, "Noncollinearly phase-matched femtosecond optical parametric amplification with a 2000 cm^{-1} bandwidth," Appl. Phys. Lett. **72**, 147–149 (1998).

[16] P. Tzankov, J. Zheng, M. Mero, D. Polli, C. Manzoni, and G. Cerullo, "300 μJ noncollinear optical parametric amplifier in the visible at 1 kHz repetition rate," Opt. Lett. **31**, 3629–3631 (2006).

[17] R. Antipenkov, A. Varanavičius, A. Zaukevičius, and A. P. Piskarskas, "Femtosecond Yb:KGW MOPA driven broadband NOPA as a frontend for TW few-cycle pulse systems," Opt. Express **19**, 3519–3524 (2011).

[18] A. Shirakawa, I. Sakane, and T. Kobayashi, "Pulse-front-matched optical parametric amplification for sub-10-fs pulse generation tunable in the visible and near infrared," Opt. Lett. **23**, 1292–1294 (1998).

[19] O. Isaienko and E. Borguet, "Pulse-front matching of ultrabroadband near-infrared noncollinear optical parametric amplified pulses," J. Opt. Soc. Am. B **26**, 965–972 (2009).

[20] A. Zaukevičius, V. Jukna, R. Antipenkov, V. Martinėnaitė, A. Varanavičius, A. P. Piskarskas, and G. Valiulis, "Manifestation of spatial chirp in femtosecond noncollinear optical parametric chirped-pulse amplifier," J. Opt. Soc. Am. B **28**, 2902–2908 (2011).

[21] G. Arisholm, J. Biegert, P. Schlup, C. Hauri, and U. Keller, "Ultra-broadband chirped-pulse optical parametric amplifier with angularly dispersed beams," Opt. Express **12**, 518–530 (2004).

[22] K. Yamane, T. Tanigawa, T. Sekikawa, and M. Yamashita, "Angularly-dispersed optical parametric amplification of optical pulses with one-octave bandwidth toward monocycle regime," Opt. Express **16**, 18345–18353 (2008).

[23] L. Cardoso, H. Pires, and G. Figueira, "Increased bandwidth optical parametric amplification of supercontinuum pulses with angular dispersion," Opt. Lett. **34**, 1369–1371 (2009).

[24] G. Valiulis, A. Dubietis, and A. Piskarskas, "Optical parametric amplification of chirped X pulses," Phys. Rev. A **77**, 043824 (2008).

[25] A. Dubietis, V. Smilgevičius, A. Stabinis, G. Valiulis, and A. Piskarskas, "Optical parametric amplification of X-shaped localised wave-packets," Quantum Electron. **39**, 599 (2009).

[26] J. Bromage, C. Dorrer, and J. D. Zuegel, "Angular-dispersion-induced spatiotemporal aberrations in noncollinear optical parametric amplifiers," Opt. Lett. **35**, 2251–2253 (2010).

[27] M. Clerici, O. Jedrkiewicz, E. Rubino, D. Faccio, L. Tartara, V. Degiorgio, and P. D. Trapani, "Generation and amplification of pulsed Bessel beams by seeding an optical parametric amplifier," Opt. Lett. **33**, 2296–2298 (2008).

[28] O. Jedrkiewicz, M. Clerici, E. Rubino, and P. Di Trapani, "Generation and control of phase-locked conical wave packets in type-I seeded optical parametric amplification," Phys. Rev. A **80**, 033813 (2009).

[29] A. Zaukevičius and G. Valiulis, "Gaussian wave-packet reshaping into conical via parametric amplification of the far field," Opt. Commun. **288**, 101–106 (2013).

[30] H. Vincenti and F. Quéré, "Attosecond Lighthouses: How To Use Spatiotemporally Coupled Light Fields To Generate Isolated Attosecond Pulses," Phys. Rev. Lett. **108**, 113904 (2012).

[31] L.-C. Cheng, C.-Y. Chang, C.-Y. Lin, K.-C. Cho, W.-C. Yen, N.-S. Chang, C. Xu, C. Y. Dong, and S.-J. Chen, "Spatiotemporal focusing-based widefield multiphoton microscopy for fast optical sectioning," Opt. Express **20**, 8939–8948 (2012).

[32] B. Zeng, W. Chu, H. Gao, W. Liu, G. Li, H. Zhang, J. Yao, J. Ni, S. L. Chin, Y. Cheng, and Z. Xu, "Enhancement of peak intensity in a filament core with spatiotemporally focused femtosecond laser pulses," Phys. Rev. A **84**, 063819 (2011).

[33] D. N. Vitek, E. Block, Y. Bellouard, D. E. Adams, S. Backus, D. Kleinfeld, C. G. Durfee, and J. A. Squier, "Spatio-temporally focused femtosecond laser pulses for nonreciprocal writing in optically transparent materials," Opt. Express **18**, 24673–24678 (2010).

[34] F. He, H. Xu, Y. Cheng, J. Ni, H. Xiong, Z. Xu, K. Sugioka, and K. Midorikawa, "Fabrication of microfluidic channels with a circular cross section using spatiotemporally focused femtosecond laser pulses," Opt. Lett. **35**, 1106–1108 (2010).

[35] M. E. Durst, A. A. Straub, and C. Xu, "Enhanced axial confinement of sum-frequency generation in a temporal focusing setup," Opt. Lett. **34**, 1786–1788 (2009).

[36] M. Durst, G. Zhu, and C. Xu, "Simultaneous spatial and temporal focusing in nonlinear microscopy," Opt. Commun. **281**, 1796–1805 (2008).

[37] D. Oron, E. Tal, and Y. Silberberg, "Scanningless depth-resolved microscopy," Opt. Express **13**, 1468–1476 (2005).

[38] X. Gu, S. Akturk, and R. Trebino, "Spatial chirp in ultrafast optics," Opt. Commun. **242**, 599–604 (2004).

[39] S. Akturk, X. Gu, E. Zeek, and R. Trebino, "Pulse-front tilt caused by spatial and temporal chirp," Opt. Express **12**, 4399–4410 (2004).

[40] S. Akturk, X. Gu, P. Gabolde, and R. Trebino, "The general theory of first-order spatio-temporal distortions of Gaussian pulses and beams," Opt. Express **13**, 8642–8661 (2005).

[41] P. Gabolde, D. Lee, S. Akturk, and R. Trebino, "Describing first-order spatio-temporal distortions in ultrashort pulses using normalized parameters," Opt. Express **15**, 242–251 (2007).

[42] M. Kolesik, J. V. Moloney, and M. Mlejnek, "Unidirectional Optical Pulse Propagation Equation," Phys. Rev. Lett. **89**, 283902 (2002).

[43] M. Kolesik and J. V. Moloney, "Nonlinear optical pulse propagation simulation: From Maxwell's to unidirectional equations," Phys. Rev. E **70**, 036604 (2004).

[44] A. Couairon, E. Brambilla, T. Corti, D. Majus, O. d. J. Ramírez-Góngora, and M. Kolesik, "Practitioner´s guide to laser pulse propagation models and simulation," Eur. Phys. J. Special Topics **199**, 5–76 (2011).

[45] M. Geissler, G. Tempea, A. Scrinzi, M. Schnürer, F. Krausz, and T. Brabec, "Light Propagation in Field-Ionizing Media: Extreme Nonlinear Optics," Phys. Rev. Lett. **83**, 2930–2933 (1999).

[46] A. V. Husakou and J. Herrmann, "Supercontinuum Generation of Higher-Order Solitons by Fission in Photonic Crystal Fibers," Phys. Rev. Lett. **87**, 203901 (2001).

[47] A. V. Husakou and J. Herrmann, "Supercontinuum generation, four-wave mixing, and fission of higher-order solitons in photonic-crystal fibers," J. Opt. Soc. Am. B **19**, 2171–2182 (2002).

[48] M. B. Gaarde and A. Couairon, "Intensity Spikes in Laser Filamentation: Diagnostics and Application," Phys. Rev. Lett. **103**, 043901 (2009).

[49] T. Brabec and F. Krausz, "Nonlinear Optical Pulse Propagation in the Single-Cycle Regime," Phys. Rev. Lett. **78**, 3282–3285 (1997).

[50] P. Kinsler and G. H. C. New, "Few-cycle pulse propagation," Phys. Rev. A **67**, 023813 (2003).

[51] A. Couairon and A. Mysyrowicz, "Femtosecond filamentation in transparent media," Phys. Rep. **441**, 47–189 (2007).

[52] P. Kinsler, "Optical pulse propagation with minimal approximations," Phys. Rev. A **81**, 013819 (2010).

[53] P. Kinsler, S. B. P. Radnor, and G. H. C. New, "Theory of directional pulse propagation," Phys. Rev. A **72**, 063807 (2005).

[54] E. Rothwell and M. Cloud, *Electromagnetics*, Electrical Engineering Textbook Series (CRC Press, 2008).

[55] A. D. Boardman, K. Marinov, D. I. Pushkarov, and A. Shivarova, "Influence of nonlinearly induced diffraction on spatial solitary waves," Opt. Quantum Electron. **32**, 49–62 (2000).

[56] M. Conforti, F. Baronio, and C. D. Angelis, "Modeling of ultrabroadband and single-cycle phenomena in anisotropic quadratic crystals," J. Opt. Soc. Am. B **28**, 1231–1237 (2011).

[57] M. Kolesik, P. Jakobsen, and J. V. Moloney, "Quantifying the limits of unidirectional ultrashort optical pulse propagation," Phys. Rev. A **86**, 035801 (2012).

[58] J. J. A. Fleck and M. D. Feit, "Beam propagation in uniaxial anisotropic media," J. Opt. Soc. Am. **73**, 920–926 (1983).

[59] J. J. Stamnes and V. Dhayalan, "Double refraction of a Gaussian beam into a uniaxial crystal," J. Opt. Soc. Am. A **29**, 486–497 (2012).

[60] M. Conforti, F. Baronio, and C. De Angelis, "Ultrabroadband Optical Phenomena in Quadratic Nonlinear Media," IEEE Photonics J. **2**, 600–610 (2010).

[61] R. R. Alfano and S. L. Shapiro, "Emission in the region 4000 to 7000 Åvia four-photon coupling in glass," Phys. Rev. Lett. **24**, 584–587 (1970).

[62] A. L. Gaeta, "Catastrophic collapse of ultrashort pulses," Phys. Rev. Lett. **84**, 3582–3585 (2000).

[63] P. Whalen, J. V. Moloney, A. C. Newell, K. Newell, and M. Kolesik, "Optical shock and blow-up of ultrashort pulses in transparent media," Phys. Rev. A **86**, 033806 (2012).

[64] G. Arisholm, "General numerical methods for simulating second-order nonlinear interactions in birefringent media," J. Opt. Soc. Am. B **14**, 2543–2549 (1997).

[65] K. Osvay, A. Kovacs, Z. Heiner, G. Kurdi, J. Klebniczki, and M. Csatari, "Angular dispersion and temporal change of femtosecond pulses from misaligned pulse compressors," IEEE J. Sel. Top. Quantum Electron. **10**, 213–220 (2004).

[66] K. Osvay, A. Kovcs, G. Kurdi, Z. Heiner, M. Divall, J. Klebniczki, and I. Ferincz, "Measurement of non-compensated angular dispersion and the subsequent temporal lengthening of femtosecond pulses in a CPA laser," Opt. Commun. **248**, 201–209 (2005).

[67] G. Pretzler, A. Kasper, and K. Witte, "Angular chirp and tilted light pulses in CPA lasers," Appl. Phys. B **70**, 1–9 (2000).

[68] S. Akturk, X. Gu, P. Bowlan, and R. Trebino, "Spatio-temporal couplings in ultrashort laser pulses," J. Opt. **12**, 093001 (2010).

[69] S. Zeng, D. Li, X. Lv, J. Liu, and Q. Luo, "Pulse broadening of the femtosecond pulses in a Gaussian beam passing an angular disperser," Opt. Lett. **32**, 1180–1182 (2007).

[70] O. E. Martinez, "Grating and prism compressors in the case of finite beam size," J. Opt. Soc. Am. B **3**, 929–934 (1986).

[71] G. Zhu, J. van Howe, M. Durst, W. Zipfel, and C. Xu, "Simultaneous spatial and temporal focusing of femtosecond pulses," Opt. Express **13**, 2153–2159 (2005).

[72] C. G. Durfee, M. Greco, E. Block, D. Vitek, and J. A. Squier, "Intuitive analysis of space-time focusing with double-ABCD calculation," Opt. Express **20**, 14244–14259 (2012).

[73] Z. Horvth, K. Osvay, and Z. Bor, "Dispersed femtosecond pulses in the vicinity of focus," Opt. Commun. **111**, 478–482 (1994).

[74] I. P. Christov, "Amplification of femtosecond pulses in a spatially dispersive scheme," Opt. Lett. **17**, 742–744 (1992).

[75] N. I. Michailov, "Passively mode-locked dye laser with spatial dispersion in the gain medium," J. Opt. Soc. Am. B **9**, 1369–1373 (1992).

[76] J. Faure, J. Itatani, S. Biswal, G. Chriaux, L. R. Bruner, G. C. Templeton, and G. Mourou, "A spatially dispersive regenerative amplifier for ultrabroadband pulses," Opt. Commun. **159**, 68–73 (1999).

[77] N. B. Chichkov, U. Bünting, D. Wandt, U. Morgner, J. Neumann, and D. Kracht, "Spatially dispersive regenerative amplification of ultrashort laser pulses," Opt. Express **17**, 24075–24083 (2009).

[78] L. Giniūnas, J. Pocius, and R. Danielius, "Energy extraction improvement in picosecond amplifiers by pulse tilting," Opt. Lett. **31**, 643–645 (2006).

[79] S. Akhmanov and S. Nikitin, *Physical Optics* (Clarendon Press, 1997).

[80] Z. Bor, B. Racz, G. Szabo, M. Hilbert, and H. A. Hazim, "Femtosecond pulse front tilt caused by angular dispersion," Opt. Eng. **32**, 2501–2504 (1993).

[81] J. Hebling, "Derivation of the pulse front tilt caused by angular dispersion," Opt. Quantum Electron. **28**, 1759–1763 (1996).

[82] R. Butkus, R. Danielius, A. Dubietis, A. Piskarskas, and A. Stabinis, "Progress in chirped pulse optical parametric amplifiers," Appl. Phys. B **79**, 693–700 (2004).

[83] D. N. Vitek, D. E. Adams, A. Johnson, P. S. Tsai, S. Backus, C. G. Durfee, D. Kleinfeld, and J. A. Squier, "Temporally focused femtosecond laser pulses for low numerical aperture micromachining through optically transparent materials," Opt. Express **18**, 18086–18094 (2010).

[84] Y.-C. Li, L.-C. Cheng, C.-Y. Chang, C.-H. Lien, P. J. Campagnola, and S.-J. Chen, "Fast multiphoton microfabrication of freeform polymer microstructures by spatiotemporal focusing and patterned excitation," Opt. Express **20**, 19030–19038 (2012).

[85] P. G. Kazansky, W. Yang, E. Bricchi, J. Bovatsek, A. Arai, Y. Shimotsuma, K. Miura, and K. Hirao, ""Quill" writing with ultrashort light pulses in transparent materials," Appl. Phys. Lett. **90**, 151120 (2007).

[86] M. M. Wefers and K. A. Nelson, "Analysis of programmable ultrashort waveform generation using liquid-crystal spatial light modulators," J. Opt. Soc. Am. B **12**, 1343–1362 (1995).

[87] A. Efimov and D. H. Reitze, "Programmable dispersion compensation and pulse shaping in a 26-fs chirped-pulse amplifier," Opt. Lett. **23**, 1612–1614 (1998).

[88] Y. Oishi, A. Suda, F. Kannari, and K. Midorikawa, "Intense femtosecond pulse shaping using a fused-silica spatial light modulator," Opt. Commun. **270**, 305–309 (2007).

[89] S. You, W. Shao, W. Cai, H. Cao, and M. Kavehrad, "Analysis of ultra-short pulse shaping with programmable amplitude and phase masks," Chin. Opt. Lett. **9**, 033201 (2011).

[90] E. Treacy, "Optical pulse compression with diffraction gratings," IEEE J. Quantum Electron. **5**, 454–458 (1969).

[91] R. L. Fork, O. E. Martinez, and J. P. Gordon, "Negative dispersion using pairs of prisms," Opt. Lett. **9**, 150–152 (1984).

[92] G. Mourou, N. Fisch, V. Malkin, Z. Toroker, E. Khazanov, A. Sergeev, T. Tajima, and B. L. Garrec, "Exawatt-Zettawatt pulse generation and applications," Opt. Commun. **285**, 720–724 (2012).

[93] M. Clerici, D. Faccio, E. Rubino, A. Lotti, A. Couairon, and P. D. Trapani, "Space–time focusing of Bessel-like pulses," Opt. Lett. **35**, 3267–3269 (2010).

[94] F. He, H. Xu, Y. Cheng, J. Ni, H. Xiong, Z. Xu, K. Sugioka, and K. Midorikawa, "Fabrication of microfluidic channels with a circular cross section using spatiotemporally focused femtosecond laser pulses," Opt. Lett. **35**, 1106–1108 (2010).

[95] M. A. Porras, R. Borghi, and M. Santarsiero, "Suppression of dispersive broadening of light pulses with Bessel–Gauss beams," Opt. Commun. **206**, 235–241 (2002).

[96] C. Manzoni, D. Polli, and G. Cerullo, "Two-color pump-probe system broadly tunable over the visible and the near infrared with sub-30 fs temporal resolution," Rev. Sci. Instrum. **77**, 023103 (2006).

[97] G. Arisholm, G. Rustad, and K. Stenersen, "Importance of pump-beam group velocity for backconversion in optical parametric oscillators," J. Opt. Soc. Am. B **18**, 1882–1890 (2001).

[98] G. Arisholm, "General analysis of group velocity effects in collinear optical parametric amplifiers and generators," Opt. Express **15**, 6513–6527 (2007).

[99] I. N. Ross, P. Matousek, G. H. C. New, and K. Osvay, "Analysis and optimization of optical parametric chirped pulse amplification," J. Opt. Soc. Am. B **19**, 2945–2956 (2002).

[100] V. Pyragaitė, A. Stabinis, R. Butkus, R. Antipenkov, and A. Varanavičius, "Parametric amplification of chirped optical pulses under pump depletion," Opt. Commun. **283**, 1144–1151 (2010).

[101] J. Zheng and H. Zacharias, "Non-collinear optical parametric chirped-pulse amplifier for few-cycle pulses," Appl. Phys. B **97**, 765–779 (2009).

[102] S. Witte, R. Zinkstok, W. Hogervorst, and K. Eikema, "Numerical simulations for performance optimization of a few-cycle terawatt NOPCPA system," Appl. Phys. B **87**, 677–684 (2007).

[103] J. Moses, C. Manzoni, S.-W. Huang, G. Cerullo, and F. X. Kaertner, "Temporal optimization of ultrabroadband high-energy OPCPA," Opt. Express **17**, 5540–5555 (2009).

[104] J. Moses and S.-W. Huang, "Conformal profile theory for performance scaling of ultrabroadband optical parametric chirped pulse amplification," J. Opt. Soc. Am. B **28**, 812–831 (2011).

[105] T. S. Sosnowski, P. B. Stephens, and T. B. Norris, "Production of 30-fs pulses tunable throughout the visible spectral region by a new technique in optical parametric amplification," Opt. Lett. **21**, 140–142 (1996).

[106] A. Harth, M. Schultze, T. Lang, T. Binhammer, S. Rausch, and U. Morgner, "Two-color pumped OPCPA system emitting spectra spanning 1.5 octaves from VIS to NIR," Opt. Express **20**, 3076–3081 (2012).

[107] Y. Stepanenko, "On the efficiency of a multiterawatt optical parametric amplifier: numerical model and optimization," J. Opt. Soc. Am. B **28**, 2337–2346 (2011).

[108] A. Thai, C. Skrobol, P. K. Bates, G. Arisholm, Z. Major, F. Krausz, S. Karsch, and J. Biegert, "Simulations of petawatt-class few-cycle optical-parametric chirped-pulse amplification, including nonlinear refractive index effects," Opt. Lett. **35**, 3471–3473 (2010).

[109] R. Boyd, *Nonlinear optics* (Academic Press, 2008).

[110] R. DeSalvo, A. Said, D. Hagan, E. Van Stryland, and M. Sheik-Bahae, "Infrared to ultraviolet measurements of two-photon absorption and n_2 in wide bandgap solids," IEEE J. Quantum Electron. **32**, 1324–1333 (1996).

[111] K. Kato, "Second-harmonic generation to 2048 Å in β-BaB_2O_4," IEEE J. Quantum Electron. **22**, 1013–1014 (1986).

[112] V. Lozhkarev, G. Freidman, V. Ginzburg, E. Katin, E. Khazanov, A. Kirsanov, G. Luchinin, A. Mal'shakov, M. Martyanov, O. Palashov, A. Poteomkin, A. Sergeev, A. Shaykin, and I. Yakovlev, "Compact 0.56 Petawatt laser system based on optical parametric chirped pulse amplification in KD*P crystals," Laser Phys. Lett. **4**, 421–427 (2007).

[113] S. Adachi, N. Ishii, T. Kanai, A. Kosuge, J. Itatani, Y. Kobayashi, D. Yoshitomi, K. Torizuka, and S. Watanabe, "5-fs, multi-mJ, CEP-locked parametric chirped-pulse amplifier pumped by a 450-nm source at 1 kHz," Opt. Express **16**, 14341–14352 (2008).

[114] M. Schultze, T. Binhammer, G. Palmer, M. Emons, T. Lang, and U. Morgner, "Multi-μJ, CEP-stabilized, two-cycle pulses from an OPCPA system with up to 500 kHz repetition rate," Opt. Express **18**, 27291–27297 (2010).

[115] J. Rothhardt, S. Demmler, S. Hädrich, J. Limpert, and A. Tünnermann, "Octave-spanning OPCPA system delivering CEP-stable few-cycle pulses and 22 W of average power at 1 MHz repetition rate," Opt. Express **20**, 10870–10878 (2012).

[116] C. Skrobol, I. Ahmad, S. Klingebiel, C. Wandt, S. A. Trushin, Z. Major, F. Krausz, and S. Karsch, "Broadband amplification by picosecond OPCPA in DKDP pumped at 515 nm," Opt. Express **20**, 4619–4629 (2012).

[117] O. Isaienko and E. Borguet, "Generation of ultra-broadband pulses in the near-IR by noncollinear optical parametric amplification in potassium titanyl phosphate," Opt. Express **16**, 3949–3954 (2008).

[118] A. Stabinis and J. Krupic, "Spatialtemporal frequency band of optical parametric amplifier," Opt. Commun. **271**, 564–568 (2007).

[119] M. A. Porras and P. Di Trapani, "Localized and stationary light wave modes in dispersive media," Phys. Rev. E **69**, 066606 (2004).

[120] S. Malaguti and S. Trillo, "Envelope localized waves of the conical type in linear normally dispersive media," Phys. Rev. A **79**, 063803 (2009).

[121] T. Auguste, O. Gobert, and B. Carré, "Numerical study on high-order harmonic generation by a Bessel–Gauss laser beam," Phys. Rev. A **78**, 033411 (2008).

[122] A. Lotti, D. Faccio, A. Couairon, M. B. Gaarde, and P. Di Trapani, "Carrier-envelope shearing and isolated attosecond pulse generation," Phys. Rev. A **83**, 053804 (2011).

[123] M. A. Porras, G. Valiulis, and P. Di Trapani, "Unified description of Bessel X waves with cone dispersion and tilted pulses," Phys. Rev. E **68**, 016613 (2003).

[124] G. Rousseau, D. Gay, and M. Piché, "One-dimensional description of cylindrically symmetric laser beams: application to Bessel-type nondiffracting beams," J. Opt. Soc. Am. A **22**, 1274–1287 (2005).

[125] G. Cerullo and S. D. Silvestri, "Ultrafast optical parametric amplifiers," Rev. Sci. Instrum. **74**, 1–18 (2003).

[126] M. A. Porras and I. Gonzalo, "Control of temporal characteristics of Bessel-X pulses in dispersive media," Opt. Commun. **217**, 257–264 (2003).

[127] L. Yu, M. Huang, M. Chen, W. Chen, W. Huang, and Z. Zhu, "Quasi-discrete Hankel transform," Opt. Lett. **23**, 409–411 (1998).

[128] M. Guizar-Sicairos and J. C. Gutiérrez-Vega, "Computation of quasi-discrete Hankel transforms of integer order for propagating optical wave fields," J. Opt. Soc. Am. A **21**, 53–58 (2004).

[129] V. V. Lozhkarev, G. I. Freidman, V. N. Ginzburg, E. A. Khazanov, O. V. Palashov, A. M. Sergeev, and I. V. Yakovlev, "Study of Broadband Optical Parametric Chirped Pulse Amplification in a DKDP Crystal Pumped by the Second Harmonic of a Nd:YLF Laser," Laser Phys. **15**, 1319–1333 (2005).

[130] Y. Z. Yoon and P. Cicuta, "Optical trapping of colloidal particles and cells by focused evanescent fields using conical lenses," Opt. Express **18**, 7076–7084 (2010).

[131] P.-A. Bélanger and M. Rioux, "Ring pattern of a lens-axicon doublet illuminated by a Gaussian beam," Appl. Opt. **17**, 1080–1088 (1978).

[132] C. Parigger, Y. Tang, D. H. Plemmons, and J. W. L. Lewis, "Spherical aberration effects in lens-axicon doublets: theoretical study," Appl. Opt. **36**, 8214–8221 (1997).

[133] M. Lei and A. Zumbusch, "Total-internal-reflection fluorescence microscopy with W-shaped axicon mirrors," Opt. Lett. **35**, 4057–4059 (2010).

[134] P. J. M. Johnson, V. I. Prokhorenko, and R. J. D. Miller, "Enhanced bandwidth noncollinear optical parametric amplification with a narrowband anamorphic pump," Opt. Lett. **36**, 2170–2172 (2011).

[135] J. Darginavičius, G. Tamošauskas, A. Piskarskas, and A. Dubietis, "Generation of 30-fs ultraviolet pulses by four-wave optical parametric chirped pulse amplification," Opt. Express **18**, 16096–16101 (2010).

[136] C. G. D. III, S. Backus, H. C. Kapteyn, and M. M. Murnane, "Intense 8-fs pulse generation in the deep ultraviolet," Opt. Lett. **24**, 697–699 (1999).

[137] I. Babushkin and J. Herrmann, "High energy sub-10 fs pulse generation in vacuum ultraviolet using chirped four wave mixing in hollow waveguides," Opt. Express **16**, 17774–17779 (2008).

[138] Y. Kida, J. Liu, and T. Kobayashi, "Single 10-fs deep-ultraviolet pulses generated by broadband four-wave mixing and high-order dispersion compensation," Appl. Phys. B **105**, 675–679 (2011).

[139] T. Fuji, T. Horio, and T. Suzuki, "Generation of 12 fs deep-ultraviolet pulses by four-wave mixing through filamentation in neon gas," Opt. Lett. **32**, 2481–2483 (2007).

[140] J. Darginavičius, G. Tamošauskas, G. Valiulis, and A. Dubietis, "Broadband four-wave optical parametric amplification in bulk isotropic media in the ultraviolet," Opt. Commun. **282**, 2995–2999 (2009).

[141] O. E. Martinez, "Pulse distortions in tilted pulse schemes for ultrashort pulses," Opt. Commun. **59**, 229–232 (1986).

[142] H. Sõnajalg and P. Saari, "Suppression of temporal spread of ultrashort pulses in dispersive media by Bessel beam generators," Opt. Lett. **21**, 1162–1164 (1996).

[143] S. Szatmári, P. Simon, and M. Feuerhake, "Group-velocity-dispersion-compensated propagation of short pulses in dispersive media," Opt. Lett. **21**, 1156–1158 (1996).

[144] S. Orlov, A. Piskarskas, and A. Stabinis, "Localized optical subcycle pulses in dispersive media," Opt. Lett. **27**, 2167–2169 (2002).

[145] C. J. Zapata-Rodríguez and M. A. Porras, "X-wave bullets with negative group velocity in vacuum," Opt. Lett. **31**, 3532–3534 (2006).

[146] Z. Liu and D. Fan, "Propagation of pulsed zeroth-order bessel beams," J. Mod. Opt. **45**, 17–21 (1998).